Efficient Quantum Gauge Simulations with the Triamond Lattice

Ali Hosseinzadehkavaki

A Dissertation Submitted to
the Faculty of Graduate Studies
in Partial Fulfillment of the Requirements
for the Degree of
Doctor of Philosophy

GRADUATE PROGRAM IN PHYSICS AND ASTRONOMY
YORK UNIVERSITY
TORONTO, ONTARIO

December 2025

Abstract

Quantum computers have the potential to revolutionize lattice gauge theory computations. While classical methods suffer from the sign problem, quantum computers enable real-time evolution dynamics, making them an exciting avenue for exploration. However, implementing lattice gauge theories on quantum hardware remains an ongoing challenge. In this work, we focus on a truncated version of SU(2) gauge theory, a well-known non-Abelian step toward quantum chromodynamics. Three-dimensional simulation in this context has barely been explored in the noisy quantum computing era, making it a crucial step toward advancing quantum simulations of gauge theories. The triamond lattice provides some key advantages for attaining the goal of working in three spatial dimensions.

Acknowledgments

I would like to express my deepest gratitude to my supervisor, **Prof. Randy Lewis**, for his exceptional guidance, mentorship, and support throughout my doctoral studies. His insight and patience shaped both this thesis and my development as a researcher, and I am sincerely grateful for the opportunity to work under his supervision.

I also wish to thank the members of my supervisory committee, **Prof. Tom Kirchner** and **Prof. Sean Tulin**, for their helpful feedback and continued encouragement. I am particularly grateful to Tom for his careful attention to detail and thoughtful comments throughout this work. I would also like to acknowledge **Prof. Patrick Draper**, the external examiner, for his time and constructive suggestions during the defense.

I have benefited from collaborations and discussions with colleagues and friends. I especially want to thank **Matthew Tsang** for his collaboration and valuable insights. I am also appreciative of the supportive academic environment at **York University**, which provided the resources and community essential to this research.

Parts of this work were carried out using quantum computers provided by **IBM**, and I gratefully acknowledge access to these devices, which supported some of the simulations presented here.

Finally, I wish to express my heartfelt appreciation to my family for their unwavering support throughout this journey. **I dedicate this thesis to my mother**, whose strength, love, and encouragement have been constant sources of motivation. Her belief in me made this achievement possible.

Contents

List of Tables

List of Figures

Chapter 1

Introduction

Quantum field theory, which merges quantum mechanics with special relativity, is a fundamental framework in high-energy physics, nuclear physics, and condensed matter physics. A crucial subclass of these theories, known as gauge theories, emerges when local symmetries are enforced. The Standard Model of Particle Physics consists of three such gauge theories governing the strong, weak, and electromagnetic interactions. Among them, quantum chromodynamics (QCD) describes the strong force between quarks and gluons. However, due to the failure of perturbation theory at large coupling constants, numerical approaches like lattice gauge theory have become indispensable for studying non-perturbative aspects of QCD [1, 2].

Lattice gauge theory has been a cornerstone in the precise numerical study of QCD, providing direct calculations of hadron properties such as masses, decay constants, and form factors. The standard formulation involves a four-dimensional Euclidean spacetime lattice, which allows for imaginary-time calculations but does not provide direct access to real-time evolution. Although this has led to significant progress in static properties, a full understanding of dynamical phenomena, such as hadron collisions, transport properties, and vacuum decay, remains elusive due to the sign problem in Monte Carlo simulations [3].

One particularly compelling example of such dynamics is **false vacuum decay**, a fundamental quantum process typically described using a double-well potential. In this picture, a system initially in a metastable false vacuum can tunnel into the true vacuum through an energy barrier. Although the decay rate can be estimated using semiclassical approximations and imaginary time evolution, this method does not provide insight into the physical mechanism of decay. A real-time simulation would enable direct observation of vacuum decay, potentially revealing bubble nucleation and the dynamics of the transition. Several approaches have been proposed for tackling this problem, but challenges remain in applying lattice gauge theory to real-time quantum field simulations [4, 5].

Quantum computing offers a promising alternative, as it enables real-time simulations beyond static properties. Unlike traditional Monte Carlo methods, which struggle with sign problems in scenarios involving real-time evolution, finite-density systems, or topological interactions, quantum simulations employ a **Hamiltonian approach** that naturally maps the exponentially large Hilbert space onto a quantum computer. This approach retains continuous time evolution while discretizing only the spatial components onto a three-dimensional lattice. Although enforcing non-Abelian Gauss's law on quantum hardware remains an active area of research, significant progress has been made in successfully implementing non-Abelian gauge theories on small quantum systems [6, 7, 8].

Despite these advances, extending lattice gauge theory into **three spatial dimensions** remains a major challenge. In a cubic lattice formulation, each site is connected to six gauge links, requiring additional qubits at each site to properly encode the non-Abelian quantum numbers and satisfy Gauss's law constraints. The **triamond lattice** presents a compelling alternative, offering a highly symmetric, isotropic structure in three-dimensional space while requiring only **three gauge links per site**. Unlike cubic lattices, where additional qubits are necessary to track intermediate angular momentum sums, the triamond lattice's structure allows gauge fields to be fully defined by the gauge link qubits alone. This significantly reduces resource overhead while preserving the essential physics of the theory [9, 10].

In the absence of matter fields, gauge invariance ensures that the non-Abelian charge flow forms closed loops on the lattice. These structures manifest as localized particles known as glueballs, which can be described as a superposition of localized gauge flux paths. On periodic lattices, there also exist torelons, large loops of color flux that wind around the lattice without contracting to a point. While these objects become heavy in the infinite-volume limit, they play an essential role in small-scale simulations, where they influence the gauge-field dynamics [11, 12].

In this work, we take a first step toward using lattice gauge theory for the real-time simulation of false vacuum decay on quantum hardware. We employ a pure gauge theory without matter fields and focus on a truncated SU(2) gauge theory, a key stepping stone toward full QCD simulations. Given the constraints of current noisy quantum devices, we implement a self-mitigation technique to improve computational accuracy, with details to be explained later. Finally, we extend our framework to a **three-dimensional triamond lattice**, deriving the SU(2) Hamiltonian and demonstrating its use on a noiseless simulator before implementing our method on IBM quantum hardware [9, 10].

By leveraging recent advances in quantum computing, this study aims to bridge the gap between traditional lattice gauge theory and real-time quantum simulations, laying the groundwork for future investigations into non-Abelian gauge dynamics, vacuum decay, and

beyond [16].

Chapter 2

Background

2.1 Quantum Chromodynamics (QCD) and the Path Integral Formalism

Quantum Chromodynamics (QCD) is the non-Abelian gauge theory that describes the strong nuclear force, one of the four fundamental forces, thereby completing the Standard Model of particle physics [17]. It governs the interactions of quarks and gluons, the fundamental constituents of hadrons such as protons and neutrons. The theory is defined by two fundamental properties: asymptotic freedom and confinement. The pivotal discovery of asymptotic freedom by Gross, Wilczek, and Politzer in 1973 [18, 19] demonstrated that the strong force weakens at short distances or high energies, enabling perturbative calculations. This breakthrough, combined with the earlier quark model and experimental evidence for hadron substructure, firmly established QCD in the early 1970s. While asymptotic freedom allows for a perturbative treatment at high energies, confinement dictates that quarks and gluons are permanently bound within color-singlet hadrons at low energies [22], defining the nature of visible matter in the universe.

The dynamics of QCD are dictated by the Lagrangian density:

$$\mathcal{L}_{\text{QCD}} = \bar{\psi}_f^a (i\gamma^\mu D_\mu - m_f)_{ab} \psi_f^b - \frac{1}{4} G^A_{\mu\nu} G_A^{\mu\nu}, \tag{2.1}$$

where ψ_f^a is the Dirac spinor for a quark of flavor f with color index $a = 1, 2, 3$, $D_\mu = \partial_\mu - i g_s G_\mu$ is the covariant derivative ensuring local $SU(3)$ gauge invariance, $G_\mu = T_A G_\mu^A$ is the gluon field, and $G^A_{\mu\nu} = \partial_\mu G^A_\nu - \partial_\nu G^A_\mu + g_s f^{ABC} G^B_\mu G^C_\nu$ is the non-Abelian field strength tensor [23].

The **path integral formalism**, developed by Feynman, provides the quantum framework

for QCD [20]. The central object is the generating functional:

$$Z_{\mathrm{QCD}}[J,\eta,\bar{\eta}] = \int \mathcal{D}\bar{\psi}\mathcal{D}\psi\mathcal{D}G\, e^{iS_{\mathrm{QCD}}[\bar{\psi},\psi,G]+i\int d^4x\,(J^A_\mu G^{A\mu}+\bar{\eta}\psi+\bar{\psi}\eta)}, \tag{2.2}$$

where $S_{\mathrm{QCD}} = \int d^4x\, \mathcal{L}_{\mathrm{QCD}}$ is the action, and J, η, $\bar{\eta}$ are source fields for the gluons, quarks, and antiquarks respectively.

The path integral formalism enables the computation of correlation functions, which are essential for extracting physical observables [23]. The n-point correlation functions are obtained by taking functional derivatives with respect to the source fields:

$$\langle 0|T[\mathcal{O}_1(x_1)\cdots\mathcal{O}_n(x_n)]|0\rangle = \frac{1}{Z[0]}\left(-i\frac{\delta}{\delta J_1(x_1)}\right)\cdots\left(-i\frac{\delta}{\delta J_n(x_n)}\right) Z[J]\Big|_{J=0}, \tag{2.3}$$

where T denotes time ordering and $\mathcal{O}_i$ are composite operators constructed from the fundamental fields.

These correlation functions contain the physical information of the theory. For example:

- **Propagators** (2-point functions) encode information about particle masses and decay widths
- **Vertex functions** (3-point functions) describe interactions between particles
- **Scattering amplitudes** can be extracted from 4-point functions.

In particular, hadron masses can be extracted from the asymptotic behavior of 2-point correlation functions [1, 11]:

$$\langle 0|T[J_H(x)J_H^\dagger(0)]|0\rangle \xrightarrow{|x^0|\to\infty} e^{-m_H|x^0|}, \tag{2.4}$$

where J_H is an interpolating operator with the quantum numbers of the hadron H, and m_H is its mass.

The fermionic fields $(\bar{\psi},\psi)$ are Grassmann-valued variables, which are integrated out formally using the properties of Gaussian integrals for fermions:

$$Z_{\mathrm{QCD}} = \int \mathcal{D}G\ \det(M[G])\, e^{iS_G[G]}, \tag{2.5}$$

where $M[G] = \gamma^\mu D_\mu + m$ is the Dirac operator. The fermionic determinant $\det(M[G])$ encapsulates the effects of virtual quark loops and plays a crucial role in the dynamics of the theory.

This path integral formulation provides a powerful framework for both perturbative and non-perturbative studies of QCD, serving as the foundation for lattice QCD computations that extract physical observables from first principles [1, 27].

2.2 Lattice Gauge Theory and Lattice QCD

While the path integral formalism provides the theoretical foundation for QCD, direct computation of correlation functions in Minkowski space-time is challenging due to the oscillatory nature of the e^{iS} factor. Lattice gauge theory, pioneered by Kenneth Wilson in 1974 [22] and building on earlier work by Wegner and others, addresses this challenge through two key innovations: discretizing space-time and performing a **Wick rotation** to Euclidean space. Wilson's seminal work introduced link variables and the plaquette action, providing the first non-perturbative formulation of gauge theories that maintained exact gauge invariance on the lattice and offered a rigorous framework for understanding confinement [21].

The Wick rotation involves substituting $t \to -i\tau$, which transforms the Minkowski space-time metric to a Euclidean one and converts the oscillatory factor e^{iS} into a real, exponentially decaying weight e^{-S_E}. This transformation is crucial as it allows the path integral to be interpreted as a statistical mechanical system :

$$Z_{\text{QCD}}^{\text{Euclidean}} = \int \mathcal{D}\bar{\psi}\mathcal{D}\psi\mathcal{D}G\, e^{-S_E[\bar{\psi},\psi,G]}. \tag{2.6}$$

The Euclidean formulation makes the path integral amenable to numerical computation through importance sampling methods, as the factor e^{-S_E} can be interpreted as a probability measure [1, 2].

In lattice QCD, the fundamental degrees of freedom are quark fields $\psi(x)$ defined on lattice sites x and gauge fields represented by link variables $U_\mu(x) \in SU(3)$ connecting neighboring sites as depicted in Fig. 2.1.

Figure 2.1: Gauge link variables on the lattice. Forward link $U_\mu(n)$ and backward link $U_{-\mu}(n) \equiv U_\mu^\dagger(n-\hat{\mu})$ connecting adjacent lattice sites.

The link variables are related to the continuum gauge fields by:

$$U_\mu(x) = e^{iag_sG_\mu(x)}, \tag{2.7}$$

where $G_\mu(x)$ is the continuum gluon field. This formulation preserves exact gauge invariance on the lattice, which is crucial for the theory's consistency.

The simplest and most widely used lattice action is the Wilson gauge action, constructed from the smallest closed loops on the lattice - the plaquettes.

A plaquette $U_{\mu\nu}(x)$, shown in Fig. 2.2, is defined as the product of four link variables around an elementary square:

$$U_{\mu\nu}(x) = U_\mu(x)U_\nu(x+\hat{\mu})U_\mu^\dagger(x+\hat{\nu})U_\nu^\dagger(x), \tag{2.8}$$

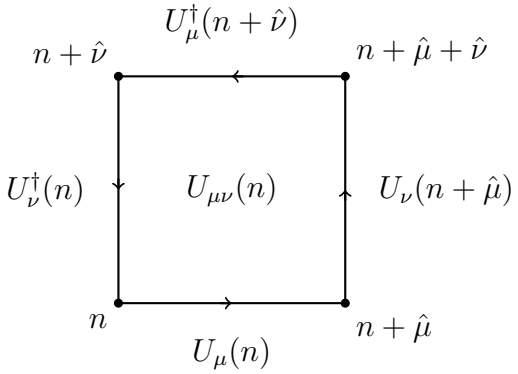

Figure 2.2: Wilson plaquette, which is the product of four gauge links around an elementary square on the lattice. The plaquette forms the basic building block for the lattice gauge action.

The Wilson gauge action is then:

$$S_G^{\text{Wilson}}[U] = \beta \sum_x \sum_{\mu<\nu} \text{Re}\,\text{Tr}\left[1 - U_{\mu\nu}(x)\right], \quad \text{where} \quad \beta = \frac{6}{g_s^2}. \tag{2.9}$$

In the continuum limit $a \to 0$, this action reproduces the familiar Yang-Mills action, ensuring the correct classical continuum theory [22].

Incorporating fermions on the lattice presents unique challenges. The naive discretization of the Dirac operator leads to the fermion doubling problem, where instead of one fermion species, the formulation produces 16 degenerate fermion flavors in four dimensions. Several solutions to this problem have been developed, each with different trade-offs [1, 2]. Wilson fermions add a momentum-dependent mass term that gives large masses to the doublers but explicitly breaks chiral symmetry. Staggered fermions reduce the number of doublers by spin diagonalization, preserving a remnant chiral symmetry. Domain wall fermions use an extra dimension to recover chiral symmetry, while overlap fermions construct an exact chiral symmetry on the lattice using the overlap Dirac operator.

The expectation value of an observable in lattice QCD is given by:

$$\langle \mathcal{O} \rangle = \frac{1}{Z} \int \prod_{\text{links}} dU_{\text{link}}\, \mathcal{O}[U, \psi, \bar{\psi}]\, \det(M[U])\, e^{-S_G[U]}, \tag{2.10}$$

with the partition function:

$$Z = \int \prod_{\text{links}} dU_{\text{link}}\, \det(M[U])\, e^{-S_G[U]}. \tag{2.11}$$

This formulation provides a mathematically well-defined framework that enables first-principles computations of hadron masses, decay constants, form factors, and other non-perturbative phenomena, making lattice QCD an essential tool for understanding the strong interaction and testing QCD predictions against experimental results [27].

2.3 Monte Carlo Sampling and the Sign Problem

The high-dimensional path integral on the lattice, with its enormous number of degrees of freedom, cannot be evaluated using conventional numerical integration methods. The **Monte Carlo method** provides the only practical approach for computing these integrals, relying on statistical sampling rather than deterministic quadrature.

2.3.1 Importance Sampling in Lattice Field Theory

The fundamental idea behind Monte Carlo integration in lattice field theory is **importance sampling**. When the Boltzmann factor $P[U] \propto \det(M[U])e^{-S_G[U]}$ is real and positive, it can be interpreted as a probability density for gauge field configurations. The expectation value of an observable is then approximated by:

$$\langle \mathcal{O} \rangle = \frac{\int \mathcal{D}U\, \mathcal{O}[U] P[U]}{\int \mathcal{D}U\, P[U]} \approx \frac{1}{N} \sum_{i=1}^{N} \mathcal{O}[U_i], \tag{2.12}$$

where $\{U_1, U_2, ..., U_N\}$ is an ensemble of gauge field configurations distributed according to $P[U]$.

The generation of these configurations typically employs Markov Chain Monte Carlo methods, where each new configuration is generated from the previous one through a stochastic process that satisfies detailed balance:

$$P[U]T[U \to U'] = P[U']T[U' \to U], \tag{2.13}$$

where $T[U \to U']$ is the transition probability from configuration U to U' [1].

2.3.2 The Metropolis Algorithm and Hybrid Monte Carlo

The simplest Monte Carlo algorithm for lattice gauge theory is the **Metropolis algorithm**[32], which proceeds as follows:

1. Start from an initial configuration U
2. Propose a local change $U \to U'$ by modifying a single link variable
3. Calculate the change in action $\Delta S = S[U'] - S[U]$
4. Accept the change with probability $P_{\text{accept}} = \min(1, e^{-\Delta S})$
5. Repeat for many sweeps through the lattice

However, for large lattices with dynamical fermions, the Metropolis algorithm becomes inefficient due to low acceptance rates. The **Hybrid Monte Carlo (HMC)** algorithm addresses this by using molecular dynamics evolution in a fictitious time to propose global changes [30].

The HMC algorithm introduces conjugate momenta π for each gauge link and evolves the system according to Hamilton's equations:

$$\frac{dU}{d\tau} = \frac{\partial H}{\partial \pi}, \quad \frac{d\pi}{d\tau} = -\frac{\partial H}{\partial U}, \tag{2.14}$$

where the Hamiltonian is given by:

$$H[U, \pi] = \frac{1}{2} \sum_{\text{links}} \pi^2 + S_G[U] - \ln \det(M[U]). \tag{2.15}$$

The fermion determinant is typically handled using pseudofermions, introducing additional fields ϕ such that:

$$\det(M[U]) = \int \mathcal{D}\phi^\dagger \mathcal{D}\phi \, e^{-\phi^\dagger M^{-1}[U] \phi}. \tag{2.16}$$

2.3.3 Autocorrelations and Critical Slowing Down

A crucial consideration in Monte Carlo simulations is the presence of **autocorrelations** between successive configurations. The autocorrelation function for an observable $\mathcal{O}$ is defined as:

$$\Gamma_{\mathcal{O}}(t) = \frac{\langle \mathcal{O}_i \mathcal{O}_{i+t} \rangle - \langle \mathcal{O} \rangle^2}{\langle \mathcal{O}^2 \rangle - \langle \mathcal{O} \rangle^2}, \tag{2.17}$$

where t is the separation in Monte Carlo time. The integrated autocorrelation time τ_{int} quantifies how many steps are needed to generate statistically independent configurations.

Near the continuum limit ($a \to 0$), simulations suffer from **critical slowing down**, where the autocorrelation time diverges as:

$$\tau_{\text{int}} \propto a^{-z}, \tag{2.18}$$

with $z \approx 2$ for local update algorithms. This makes continuum extrapolations computationally very expensive [1].

2.3.4 The Sign Problem: A Fundamental Limitation

The Monte Carlo approach relies crucially on interpreting $P[U]$ as a probability measure, which requires it to be real and positive. However, in many physically important scenarios, this condition is violated, leading to the infamous **sign problem** [3, 31].

Mathematically, when $P[U] = |P[U]|e^{i\theta[U]}$, the expectation value becomes:

$$\langle \mathcal{O} \rangle = \frac{\int \mathcal{D}U \, \mathcal{O}[U]|P[U]|e^{i\theta[U]}}{\int \mathcal{D}U \, |P[U]|e^{i\theta[U]}} = \frac{\langle \mathcal{O}e^{i\theta} \rangle_{|P|}}{\langle e^{i\theta} \rangle_{|P|}}, \tag{2.19}$$

where $\langle \cdots \rangle_{|P|}$ denotes averaging with respect to the positive weight $|P[U]|$.

The denominator $\langle e^{i\theta} \rangle_{|P|}$ is the average sign, which typically decreases exponentially with system size:

$$\langle e^{i\theta} \rangle_{|P|} \propto e^{-\beta V \Delta f}, \tag{2.20}$$

where β is the inverse temperature, V is the volume, and Δf is the free energy density difference between the original system and the phase-quenched system used for importance sampling.

The statistical error in estimating $\langle \mathcal{O} \rangle$ grows as:

$$\delta \mathcal{O} \propto \frac{1}{\sqrt{N} |\langle e^{i\theta} \rangle_{|P|}|}, \tag{2.21}$$

requiring the number of samples N to grow exponentially to maintain constant precision [3].

2.3.5 Physical Scenarios Exhibiting the Sign Problem

The sign problem appears in several crucial physical regimes:

Finite Baryon Density: At finite quark chemical potential μ, the fermion determinant becomes complex:

$$\det(M[U,\mu]) \in \mathbb{C}, \tag{2.22}$$

preventing studies of dense matter relevant for neutron star interiors and heavy-ion collisions [3].

Real-Time Dynamics: Studying real-time evolution requires working with Minkowski space-time, where the weight is oscillatory:

$$e^{iS_M} \quad \text{instead of} \quad e^{-S_E}. \tag{2.23}$$

Topological θ-Terms: Including a CP-violating term in the QCD action introduces a complex phase:

$$S_\theta = i\theta Q, \quad Q = \frac{g^2}{32\pi^2}\int d^4x\, G^a_{\mu\nu}\tilde{G}^{a\mu\nu}, \tag{2.24}$$

where Q is the topological charge [28].

Finite Magnetic Fields: Strong magnetic fields, relevant for heavy-ion collisions and magnetars, can also induce complex phases in the fermion determinant [33].

2.3.6 Attempted Solutions and Workarounds

Despite decades of research, no general solution to the sign problem exists. Various approaches have been developed with limited success [3]:

- **Complex Langevin:** Extending the Langevin equation to complex actions, though convergence issues often arise
- **Lefschetz Thimble:** Deforming the integration contour into complex space along steepest descent paths [36, 29]
- **Density of States:** Rewriting the partition function as an integral over the density of states
- **Reweighting:** Using the phase-quenched ensemble and reweighting by the complex phase, though this suffers from the exponential degradation described above

The absence of a general solution to the sign problem represents one of the major outstanding challenges in computational quantum field theory and motivates the exploration of

alternative approaches like quantum computing for studying real-time dynamics and finite-density systems [6, 7, 8].

2.4 Hamiltonian Method and Quantum Computers

The limitations of classical Monte Carlo methods, particularly the sign problem that prevents studies of real-time dynamics and finite-density systems, have motivated the exploration of alternative approaches. While quantum computers are often heralded as a solution, it is crucial to understand that the fundamental breakthrough comes from the **Hamiltonian formulation** of lattice gauge theories, with quantum computers serving as a natural platform for implementing this approach. This section explores the Hamiltonian method as an alternative to the path integral formalism, its challenges on classical computers, and why quantum computers provide a promising pathway for Hamiltonian-based simulations [6, 7, 8].

2.4.1 Hamiltonian Formulation of Lattice Gauge Theories

While the path integral formulation has been tremendously successful for Euclidean lattice calculations, an alternative approach exists through the **Hamiltonian formulation**. This method provides a complementary perspective that is particularly well-suited for real-time evolution and quantum simulations [26].

In the Hamiltonian approach, we discretize space while keeping time continuous. The fundamental variables are the gauge fields and their conjugate momenta. For a general SU(N) lattice gauge theory, the Hamiltonian is given by [57]:

$$H = \frac{g^2}{2a}\Big[\sum_{r,\mu}\sum_{\alpha}\big(E^{\alpha}(r,\mu)\big)^2 + x\sum_{p\in\{\text{plaquettes}\}}\big(2N - (U_P + U_P^{\dagger})\big)\Big] \tag{2.25}$$

where g is the coupling constant, a is the lattice spacing, $x = 2/g^4$, and the plaquette operator is $U_P = \mathrm{Tr}\left[U(r,\mu)U(r+\mu,\nu)U^{\dagger}(r+\nu,\mu)U^{\dagger}(r,\nu)\right]$. The operators E^{α} and U satisfy the commutation relations:

$$[E^{\alpha}, U_{ij}] = \frac{1}{2}\sum_{k=1}^{N}\tau^{\alpha}_{ik}U_{kj}, \quad \left[E^{\alpha}, U^{\dagger}_{ij}\right] = -\frac{1}{2}\sum_{k=1}^{N}U^{\dagger}_{ik}\tau^{\alpha}_{kj}, \quad \left[E^{\alpha}, E^{\beta}\right] = if^{\alpha\beta\gamma}E^{\gamma}, \tag{2.26}$$

where τ^{α} are the generators of SU(N).

For SU(2) gauge theory, which serves as an important stepping stone toward full QCD, the Hamiltonian takes a more specific form. Omitting the overall constant $g^2/2a$ and the

constant energy shift $2N$ for clarity, the Kogut-Susskind Hamiltonian for SU(2) is [26]:

$$H_{\mathrm{SU}(2)} = \sum_{r,\mu} \sum_{\alpha} \left(E^{\alpha}(r,\mu)\right)^2 - 2x \sum_{p \in \{\text{plaquettes}\}} U_P, \tag{2.27}$$

where a simplification occurs since $U_P^{\dagger} = U_P$ for SU(2). In this case, the electric field operators E^a (with $a = 1, 2, 3$) are the generators of SU(2) and satisfy the commutation relations:

$$[E_i^a, E_j^b] = i\epsilon^{abc}\delta_{ij}E_i^c, \tag{2.28}$$

$$[E^a, U] = \frac{1}{2}\tau^a U, \quad [E^a, U^{\dagger}] = -\frac{1}{2}U^{\dagger}\tau^a, \tag{2.29}$$

where τ^a are the Pauli matrices. The scalar electric energy term is $E^2 = \sum_a (E^a)^2$, and U_P is the product of link variables around a plaquette.

The Hamiltonian formulation naturally avoids the sign problem because it works directly with Hermitian operators in Hilbert space rather than dealing with complex weights in a path integral. This makes it particularly advantageous for studying real-time dynamics, finite density systems, and topological terms where the sign problem appears in the Lagrangian approach [6].

2.4.2 Challenges of Hamiltonian Methods on Classical Computers

Despite its conceptual advantages, the Hamiltonian approach faces significant challenges when implemented on classical computers. The primary difficulty stems from the **exponential growth** of the Hilbert space with system size. For a lattice with N links, each carrying d degrees of freedom, the total Hilbert space dimension grows as d^N.

Furthermore, implementing **gauge invariance** as a constraint on the Hilbert space requires careful construction of physical states that satisfy Gauss's law:

$$G^a(\mathbf{x})|\psi\rangle = \left[\sum_{\text{links at } \mathbf{x}} E^a_{\text{link}} - \rho^a(\mathbf{x})\right]|\psi\rangle = 0, \tag{2.30}$$

where $\rho^a(\mathbf{x})$ represents the matter charge density. Enforcing this constraint throughout the computation adds considerable complexity to classical algorithms [40, 34, 35].

These limitations make classical simulation of Hamiltonian lattice gauge theories prohibitively expensive for all but the smallest systems, particularly when studying real-time evolution or complex vacuum structures [41].

2.4.3 Quantum Computers as Natural Simulators

Quantum computers offer a natural platform for implementing Hamiltonian lattice gauge theories. The fundamental principles of quantum computation align perfectly with the requirements of Hamiltonian simulations [7, 8]:

- **Exponential State Representation:** A quantum computer's state space grows as 2^n for n qubits, providing an efficient representation of the exponentially large Hilbert space of lattice gauge theories.
- **Natural Time Evolution:** Quantum computers natively implement time evolution through unitary operators e^{-iHt}, exactly as required by the Hamiltonian formulation.
- **Gauge Invariance as Quantum Circuits:** The constraints of Gauss's law can be implemented directly in the quantum circuit design, ensuring that all operations remain within the physical Hilbert space [57, 63, 34, 35, 40].

The mapping from the gauge theory Hilbert space to qubits can be achieved through various encodings, such as the quantum link model or group element basis. For SU(2) gauge theory, each link can be represented using multiple qubits, with operations designed to preserve the gauge symmetry [13, 14].

2.4.4 Current Challenges and Error Mitigation

Current quantum computing hardware operates in the Noisy Intermediate-Scale Quantum era, facing significant challenges from environmental noise and imperfect control. The primary noise sources include decoherence, gate infidelities, readout errors, crosstalk, and calibration drift [42].

To address these challenges, researchers have developed powerful error mitigation strategies [42, 43]:

- **Zero-Noise Extrapolation:** Intentionally amplifying noise in a controlled manner, then extrapolating back to the zero-noise limit
- **Probabilistic Error Cancellation:** Using detailed noise characterization to apply correction operations in post-processing
- **Readout Error Mitigation:** Constructing response matrices to correct measurement inaccuracies

- **Self-Mitigation:** Leveraging physical constraints, particularly time reversal invariance, to identify and correct symmetry-violating errors. [15]

These techniques enable meaningful quantum simulations of lattice gauge theories even with current hardware limitations, providing a pathway toward increasingly accurate simulations as quantum technology advances [16].

The combination of Hamiltonian methods and quantum computing represents a promising frontier for studying non-perturbative aspects of gauge theories, particularly for real-time dynamics and regimes inaccessible to classical Monte Carlo methods.

Chapter 3

From square plaquettes to triamond lattices for SU(2) gauge theory

The content in this chapter is a direct reproduction of [9].

3.1 Introduction

Quantum field theory combines quantum mechanics with special relativity and is of widespread importance in high-energy physics, nuclear physics, and condensed matter physics. Enforcing a spatially local symmetry leads to the special case of a gauge theory. The standard model of particle physics is a collection of three gauge theories describing the strong, weak and electromagnetic forces. Because perturbation theory cannot be applied to a large coupling constant, many aspects of the strong force are best described by a numerical approach called lattice gauge theory.

Lattice gauge theory has been of central importance to quantum chromodynamics for several decades and has become a precision tool for practitioners [1, 2]. It provides rigorous calculations of static properties, such as the masses and form factors of hadrons, directly from the gauge theory of quarks and gluons. Such calculations are crucial in the ongoing quest to understand hadron physics, such as the tetraquarks and pentaquarks that have been discovered experimentally in recent years [39, 44]. Lattice gauge theory calculations also provide necessary input for experiments seeking new physics beyond the standard model, where a famous recent example is the anomalous magnetic moment of the muon [45].

Quantum computers offer a prospective way to calculate more than just static properties. Traditional lattice gauge theory uses Monte Carlo methods that would have sign problems if applied straightforwardly to situations involving dynamics, nonzero density, or some topological interactions [3, 6]. These sign problems can be avoided by using a Hamiltonian approach,

where the exponentially large Hilbert space can fit naturally onto a quantum computer. Now that quantum computing hardware is becoming a reality, this powerful new approach to lattice gauge theory is being developed by a broad community of researchers [6, 7, 8].

With quantum chromodynamics as a motivating long-range goal, the present work is focused on the simplest non-Abelian gauge theory. Being non-Abelian means that gauge fields carry the relevant charge directly and can therefore interact among themselves, like the gluons of quantum chromodynamics and in contrast to the photons of quantum electrodynamics. Specifically our work will consider SU(2) gauge theory in the absence of fermions, and we will truncate the gauge field to fit on a small number of qubits. Several research groups have already carried out exploratory studies of non-Abelian gauge theories on quantum computing hardware [46, 13, 47, 48, 14, 49, 50, 15, 51, 52, 53, 54]. There have also been many theoretical studies laying the groundwork for anticipated implementations on larger quantum computers [26, 55, 56, 57, 58, 59, 60, 61, 62, 63, 64, 65, 66, 67, 68, 69, 40, 70, 71, 72, 73, 74, 75, 76, 28, 77, 78, 79, 41, 80, 81, 82, 83, 84, 85, 86, 87, 88, 89, 16, 90, 91, 92, 93, 95, 94, 96, 97]. In the present work, we address two important issues: an effective way to mitigate errors and a practical way to extend lattices into three spatial dimensions.

Future quantum computers are expected to have smaller error rates and robust methods for correcting those errors, but calculations in the present era face substantial error rates and typically have insufficient resources to implement true error correction. Instead, error mitigation methods have been devised [42], and these can provide significant improvements for computations performed on today's hardware. Our study demonstrates the use of an existing method called self-mitigation [15] but in a new context: evolution of a quantum state through imaginary time. As is well known, after sufficiently many steps of imaginary time the excited state contributions to a generic initial state will become exponentially suppressed relative to the ground state, thus providing a way to create the ground state and to determine its eigenvalue. Our results will demonstrate that self-mitigation correctly finds and sustains the true ground state of a two-plaquette lattice even though the unmitigated data points are moving ever farther from the true result with each additional time step.

With successful mitigation in hand, we then turn our attention to lattice gauge theory in three spatial dimensions. While this can be done with a standard cubic lattice, where six gauge links touch each lattice site, there is an important issue to address. Specifically, for any lattice where more than three gauge links meet at a lattice site, the quantum numbers of the gauge links themselves are insufficient to fully define the state of the gauge field across the lattice [68, 71, 86, 90]. To understand why, consider a two-dimensional square lattice where four SU(2) gauge links meet at every site. At one particular site, suppose each of the four gauge links happen to have quantum number $j = \frac{1}{2}$, where j is notation familiar from

quantized angular momentum though here it refers to the gauge degrees of freedom. One pair of these links could sum to $j_{\text{pair}} = 0$ or 1. The other pair must have the same sum because Gauss's law requires the total of all four to be $j_{\text{site}} = 0$. Therefore a full description of the state requires not just the j values of individual links, but also the value of j_{pair} for some pair selected by the user to define that site.

One way to handle this issue is to assign a sufficient number of additional qubits at each lattice site, being careful to define a convention at each site, thereby completing the state's definition [68, 71, 86, 90]. The number of additional qubits needed to define j_{pair} grows logarithmically with the user's choice for j_{max}. Moreover, a three-dimensional lattice needs more than a single j_{pair} at each site. In the present work we propose an alternative based on a structure from crystallography [105, 106, 107, 108, 109, 110]. Having only three links at each site, our choice will avoid the need for any quantum numbers beyond the individual link values.

Consider a lattice where each site is touched by exactly three gauge links that have equal lengths, lie in a single plane, and are placed at equal angles around the site, i.e. $2\pi/3$. This forms a three-dimensional lattice that has a high degree of symmetry and needs no additional qubits beyond the links themselves. Because of its similarity to a diamond crystal of carbon atoms but with three links per site instead of more, it has been called the triamond lattice [108, 109]. It is also known as the Laves lattice [106] or the K_4 lattice [107, 110]. In this work, we provide an introduction to lattice gauge theory on the triamond framework. We derive the SU(2) Hamiltonian for a triamond lattice and demonstrate its use on a noiseless simulator. Then we employ our method for error-mitigated imaginary time evolution to create the ground state of the three-dimensional triamond unit cell on an IBM quantum computer [156].

3.2 Results

3.2.1 Imaginary Time Evolution on Square Plaquettes

Finding the ground state for a given Hamiltonian is an important ingredient of many scientific studies. Two common approaches are variational methods and imaginary time evolution. Variational methods rely on an ansatz chosen by the user, and can only get as close to the true ground state as the ansatz will allow. In contrast, imaginary time evolution always converges to the true ground state unless the initial state is perfectly orthogonal to it.

Imaginary time evolution is used routinely in traditional lattice gauge theory on classical computers. Our motivation to study it now on a quantum computer is not to compete

with successful classical methods, but rather to imagine that ground-state preparation will become the first step in a larger computation that truly does require quantum computing [160, 148, 161]. Imaginary time evolution has recently been applied to Z_2 gauge theory as well [162].

Our first computation uses a lattice comprising two side-by-side square plaquettes that share a single gauge link, thus forming a left path, a center path, and a right path as shown in Fig. 3.1. Each of the seven gauge links on this lattice is a superposition of SU(2) representations, and Gauss's law requires the three on the left path to equal one another and similarly the three on the right path must equal one another. For our calculation we truncate the basis and retain only the two lowest states for each gauge link, $j = 0$ and $j = \frac{1}{2}$.

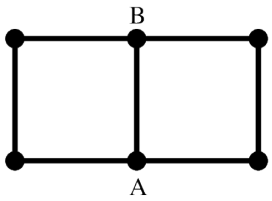

Figure 3.1: **A minimal lattice.** This is the first lattice used to demonstrate self-mitigation for quantum imaginary time evolution. The text refers to the 3 paths between sites A and B as the left path (three links), the center path (one link), and the right path (three links).

Any state of this system can be described by two qubits, one for the left path and one for the right path, because Gauss's law then determines the center path uniquely. Such a tiny system is a valuable place to study error mitigation because a single time step requires only a simple circuit while more and more time steps will require more and more entangling gates. The real-time evolution of this system was studied previously as the first example of self-mitigation [15]. The Hamiltonian, in units of $g^2/2$, is

$$\begin{aligned} \hat{H} &= \frac{3}{8}\left(7 - 3\hat{Z}_0 - \hat{Z}_0\hat{Z}_1 - 3\hat{Z}_1\right) - \frac{x}{2}\left(3 + \hat{Z}_1\right)\hat{X}_0 \\ &\quad -\frac{x}{2}\left(3 + \hat{Z}_0\right)\hat{X}_1 \,, \end{aligned} \tag{3.1}$$

where $x = 2/g^4$ and g is the coupling constant, i.e. the strength of the strong interaction for this physics theory. The Pauli gates acting on qubit i are $\hat{X}_i$, $\hat{Y}_i$ and $\hat{Z}_i$.

Imaginary time evolution is not a unitary operation, so how can it be implemented on a quantum computer? We use an algorithm developed by Motta et al., called quantum imaginary time evolution (QITE) [98], which can be described as follows. The evolution we seek is

$$|\Psi(\tau)\rangle = e^{-\tau\hat{H}}\,|\Psi(0)\rangle \,, \tag{3.2}$$

where τ is the real-valued Euclidean time parameter. We can define a normalized state $|\psi\rangle$ such that $|\Psi(0)\rangle = r\,|\psi\rangle$ for positive r. The evolution can always be expressed as

$$|\Psi(\tau)\rangle = r' e^{-i\tau\hat{A}}\,|\psi\rangle\ , \tag{3.3}$$

for some unitary operator $e^{-i\tau\hat{A}}$ and positive r'. An immediate consequence is

$$r' = r\left(1 - \tau\,\langle\psi|\,\hat{H}\,|\psi\rangle\right) + O(\tau^2)\,. \tag{3.4}$$

The operator $\hat{A}$ can be determined from a state tomography of $|\psi\rangle$ that reflects the specific qubit connectivities of $\hat{H}$.

For our physics example, Eq. (3.1) confirms that the Hamiltonian is purely real, meaning that we can restrict ourselves to real-valued basis states as well. Together with Eqs. (3.2) and (3.3), this realness means $\hat{A}$ must be purely imaginary, leading to a general expression with odd powers of $\hat{Y}_i$ gates,

$$\begin{aligned}\hat{A} \;=\;& a_{iy}\hat{Y}_0 + a_{xy}\hat{X}_1\hat{Y}_0 + a_{zy}\hat{Z}_1\hat{Y}_0 \\ & + a_{yi}\hat{Y}_1 + a_{yx}\hat{Y}_1\hat{X}_0 + a_{yz}\hat{Y}_1\hat{Z}_0\,.\end{aligned} \tag{3.5}$$

The state tomography that determines the values of the coefficients a_{jk} will be discussed in the methodology section. With those values in hand, and with r' obtained from the calculation of Eq. (3.4), the state at a small value of τ can be computed from Eq. (3.3). In particular, we use

$$e^{-i\theta\hat{Y}_j} \;=\; RY_j(2\theta)\,, \tag{3.6}$$

$$e^{-i\theta\hat{X}_j\hat{Y}_k} \;=\; CX_{kj}RY_k(2\theta)CX_{kj}\,, \tag{3.7}$$

$$e^{-i\theta\hat{Z}_j\hat{Y}_k} \;=\; CX_{jk}RY_k(2\theta)CX_{jk}\,, \tag{3.8}$$

where CX_{jk} is a controlled not (CNOT) gate with qubit j as control and qubit k as target.

For sufficiently small τ, the operator $e^{-i\theta\hat{A}}$ can be approximated by a product of six factors, one for each term in $\hat{A}$. For a better approximation, that first-order Trotter expression can be replaced by the second-order Trotter expression represented by the circuit shown in Fig. 3.2. To reach a larger value of τ, we can perform a sequence of small steps where the circuit is several end-to-end copies of Fig. 3.2. Notice that the tomography needs to be computed separately for each step, using the state at the previous step as input.

Because the two-qubit CNOT gate is noisier than a single-qubit gate on quantum hardware, the gates in Fig. 3.2 have been ordered in a way that minimizes the number of CNOT

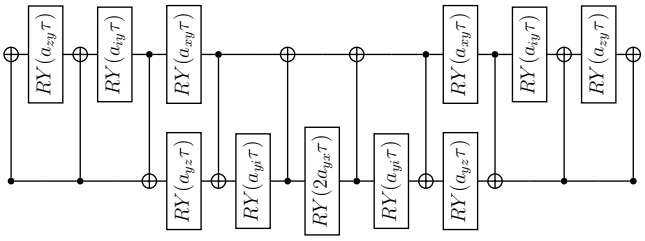

Figure 3.2: **One Trotter step.** This circuit is used for one second-order Trotter step of imaginary time evolution for SU(2) gauge theory on a lattice comprising two square plaquettes. τ is the real-valued Euclidean time parameter. The coefficients a_{jk} define time evolution as shown in Eq. (3.5).

gates. Also, the CNOT gate at the end of one Trotter step will cancel the CNOT gate at the beginning of the next step. As well, the very first CNOT gate in the circuit can be omitted because the initial control qubit is always off. Nevertheless, the error bars without symbols in Fig. 3.3 show that only the first two or three time steps approach the true ground state energy and then subsequent time steps move further and further away. The quantum computation is overwhelmed by hardware noise without ever reaching the correct result.

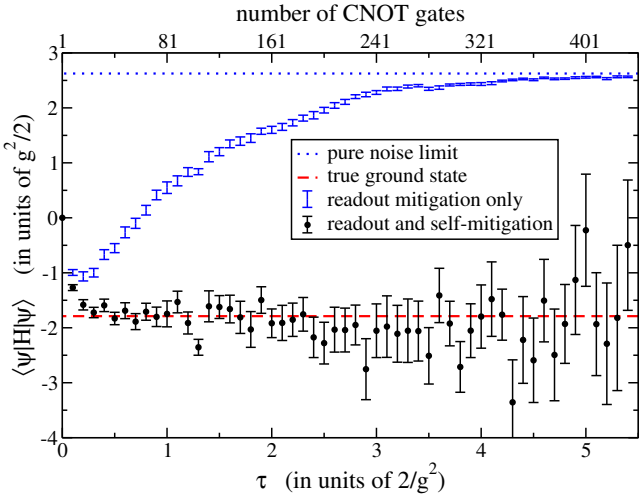

Figure 3.3: **Quantum imaginary time evolution with and without self-mitigation.** These results are for SU(2) gauge theory with $j_{\max} = \frac{1}{2}$ on a lattice comprising two square plaquettes. The gauge coupling is $x = 1$ and the time step is $\Delta\tau = 0.1$ in units of $2/g^2$. Each quantum circuit uses 50 randomized compilings with 10^4 shots per compiling. All quantum computations were performed on `ibm_lagos`. Black data points use self-mitigation and blue data points do not. Error bars are 95% confidence intervals. The true ground state is shown as a red dashed line. The pure noise limit is shown as a blue dotted line.

Self-mitigation is able to extract the true result from the computed data. The original implementation [15], which was inspired by the work of Ref. [43], has subsequently been used

and extended in various ways [51, 52, 54, 89, 99, 100, 101, 102, 148, 103]. The basic idea is to run a mitigation circuit that is identical to the physics circuit except that $\tau \to -\tau$ in the second half of the circuit. If your circuit has an odd number of second-order Trotter steps, use $2\tau \to 0$ in the center gate (see, for example, Fig. 4.4) and insert a barrier to prevent CNOT cancellation.

The true outcome of the mitigation circuit should be identical to the initial state, i.e. all qubits should be in the off position. Comparison of the computed results with this known true result provides a measurement of hardware errors. The physics circuit will have similar hardware errors because the two circuits are identical up to the sign of τ in the latter half.

More precisely, randomized compiling (see methodology section) is used to convert CNOT errors into incoherent noise that is well described by the depolarizing noise model [43]. For our example of imaginary time evolution, this leads to a pair of ratios,

$$\left.\frac{\left\langle \hat{P}_j \right\rangle_{\text{true}}}{\left\langle \hat{P}_j \right\rangle_{\text{comp}}}\right|_{\text{physics run}} = \left.\frac{1}{\left\langle \hat{Z}_j \right\rangle_{\text{comp}}}\right|_{\text{mitigation run}}, \tag{3.9}$$

$$\left.\frac{\left\langle \hat{P}_j \hat{P}_j \right\rangle_{\text{true}}}{\left\langle \hat{P}_j \hat{P}_k \right\rangle_{\text{comp}}}\right|_{\text{physics run}} = \left.\frac{1}{\left\langle \hat{Z}_j \hat{Z}_k \right\rangle_{\text{comp}}}\right|_{\text{mitigation run}}, \tag{3.10}$$

where $\hat{P}_j \in \{\hat{X}_j, \hat{Y}_j, \hat{Z}_j\}$. These equations give the true expectation value of a Pauli string as the ratio of results computed by a physics run and a mitigation run. They are the counterparts of Eq. (8) in the original paper [15] but look slightly different because the previous work studied probabilities that equalled $\frac{1}{2}$ in the pure noise limit whereas the present work employs expectation values of Pauli strings that are zero for pure noise.

The filled data points of Fig. 3.3 were obtained by computing each term of Eq. (3.1) from the ratios in Eqs. (3.9) and (3.10). The physics runs and mitigation runs (with 50 randomized compilings for each) and the readout error mitigation runs were all completed within a single `qiskit` job [104] to ensure they were experiencing the same hardware conditions. Whereas the unmitigated data in Fig. 3.3 approach the pure noise limit of $\frac{21}{8}$, where only the first term in Eq. (3.1) makes a nonzero contribution, the self-mitigated data points in Fig. 3.3 remain consistent with the true ground state as τ increases. Error bars grow as the circuit gets longer, but meaningful results are still obtained with more than 400 CNOT gates. This success provides an incentive to move toward larger lattices, including novel three-dimensional approaches like the triamond lattice.

3.2.2 The SU(2) Hamiltonian for a Triamond Lattice

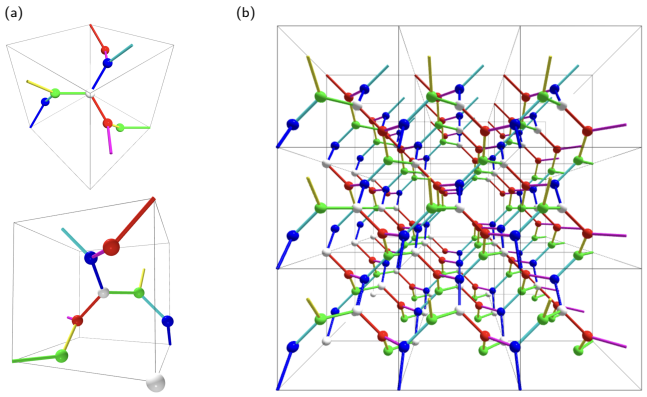

Figure 3.4: **The triamond lattice.** Panel (a) shows two views of the unit cell, which always contains 8 sites and 12 gauge links. Panel (b) shows a lattice having 3 unit cells along each direction. In both panels, the colour of each link defines its direction according to Eqs. (3.11) and (3.12).

Fig. 3.4 shows the locations of lattice sites and gauge links on a triamond lattice. See also our two-minute video presentation (`https://vimeo.com/904585432`), which provides views of the triamond lattice from a camera moving around it.

To introduce the triamond lattice quantitatively, we will first define six unit vectors labeled as colors (red, green, blue, cyan, magenta, yellow) to aid the discussion,

$$\hat{r} = \frac{\hat{j} - \hat{k}}{\sqrt{2}}, \qquad \hat{g} = \frac{\hat{i} - \hat{j}}{\sqrt{2}}, \qquad \hat{b} = \frac{\hat{k} - \hat{i}}{\sqrt{2}}, \tag{3.11}$$

$$\hat{c} = \frac{\hat{j} + \hat{k}}{\sqrt{2}}, \qquad \hat{m} = \frac{\hat{i} + \hat{j}}{\sqrt{2}}, \qquad \hat{y} = \frac{\hat{k} + \hat{i}}{\sqrt{2}}, \tag{3.12}$$

where $\hat{i}$, $\hat{j}$ and $\hat{k}$ are the standard orthonormal vectors. Every gauge link in the triamond lattice is along one of these color directions. As an aside, we note that the colors defined here have nothing to do with the colors of quantum chromodynamics.

Each lattice site is touched by three gauge links that lie in a plane. The complete lattice has just four sets of parallel planes, so we color each site white, red, green or blue to represent which plane is at that site. The links and sites form a color scheme that is motivated by the well-known RGB model of colors: each white site is touched by red, green and blue links, each red site is touched by red, magenta and yellow links, each green site is touched by green, cyan and yellow links, and each blue site is touched by blue, cyan and magenta links.

The angle between any two planes is $\arccos(\frac{1}{3})$, which is familiar because this same angle lies between any pair of lines joining the center of a cube to its corners. Because the unit vector orthogonal to a plane is only unique up to its sign, the triamond lattice is chiral. Specifically, the mirror image of Fig. 3.4 is a distinct but equally valid triamond lattice.

Notice that the white sites of a triamond lattice form a body-centered cubic (bcc) structure. It is useful to compare the options of defining a lattice gauge theory on a triamond lattice, on a bcc lattice, or on a simple cubic lattice. Relative to a simple cubic lattice of the same volume, a bcc lattice has twice as many lattice sites, gauge links that are shorter by a factor of $\sqrt{2}$, and each bcc site has 8 nearest neighbors compared to 6 for the simple cubic lattice. This suggests that a bcc lattice could be valuable for efficient discussions of the continuum limit, perhaps alongside simple cubic studies. Importantly, the bcc and simple cubic lattices both have more than three gauge links touching each lattice site, meaning that extra qubits would be needed within each lattice site (and a convention must be chosen) to fully define the quantum state of the lattice [68, 71, 86]. In a sense, the triamond lattice can be viewed as a bcc lattice where those implicit qubits have been made explicit and unambiguous by creating the red, green and blue sites.

Although the white sites do form a bcc lattice, the triamond lattice is more economical than merely being a clarified bcc lattice. Imagine, for example, shrinking the red, green and blue links into their white sites. The remaining lattice would not be bcc because it would have only 6 links per unit cell (2 cyan, 2 magenta, and 2 yellow) whereas a bcc lattice would require 8 links per unit cell.

The comparison to bcc is encouraging, but our primary motivation for proposing the triamond lattice is the fact that it has exactly three links touching each site, so the j values of each gauge link are sufficient to define basis states for the lattice. For planar physics, a hexagonal lattice succeeds in having three links touching each site, and SU(2) gauge theory has recently been implemented on a hexagonal lattice [90, 93]. Notice that the shortest closed paths on a hexagonal lattice have six gauge links.

The shortest closed paths on a triamond lattice have 10 gauge links. We refer to these as elementary plaquettes. Among the 10 gauge links comprising any elementary plaquette, one of the 6 colors is absent and the other 5 colors always occur twice. The lattice has only 6 orientations of plaquettes (the non-red plaquette, the non-green plaquette, etc.), with copies of them translated spatially throughout the lattice.

To perform any quantum computation on a triamond lattice, we need a Hamiltonian. For SU(2) gauge theory, the Hamiltonian is the non-Abelian generalization of quantum electrodynamics and is written as a sum of electric terms and magnetic terms [26]. In the continuum

limit, the Hamiltonian is

$$H^{\rm cont} = H_E^{\rm cont} + H_B^{\rm cont}\,, \tag{3.13}$$

$$H_E^{\rm cont} = g^2 \int {\rm Tr}\left(E_x^2 + E_y^2 + E_z^2\right) d^3x\,, \tag{3.14}$$

$$H_B^{\rm cont} = \frac{1}{g^2} \int {\rm Tr}\left(F_{xy}^2 + F_{yz}^2 + F_{zx}^2\right) d^3x\,, \tag{3.15}$$

where each trace is over the SU(2) indices of the electric field $\vec{E}$ or field strength tensor $F_{\mu\nu}$. (Other normalization conventions are sometimes used for $\vec{E}$ and $F_{\mu\nu}$ [90].)

On a lattice, each gauge link is an element of SU(2),

$$U(\vec{n}, \hat{s}) = e^{ia\hat{s}\cdot\vec{A}(\vec{n})}\,, \tag{3.16}$$

where a is the lattice spacing. The component of the gauge field at site $\vec{n}$ that points in direction $\hat{s}$ is an element of the SU(2) algebra,

$$A_s(\vec{n}) = \sum_{k=1}^{3} \sigma^k A_s^k(\vec{n})\,. \tag{3.17}$$

Our computations will be performed in the electric basis, where the magnetic terms are best expressed as a sum of all elementary plaquettes in this lattice and each plaquette is the trace of the ordered product of the 10 gauge links comprising that plaquette. The somewhat tedious derivation of this lattice Hamiltonian is outlined in A. The result is

$$H = H_E + H_B\,, \tag{3.18}$$

$$H_E = \frac{8\sqrt{2}a^3g^2}{3} \sum_{n={\rm links}} {\rm Tr}\left(E_x^2(n) + E_y^2(n) + E_z^2(n)\right), \tag{3.19}$$

$$H_B = -\frac{2\sqrt{2}}{g^2 a} \sum_{\vec{w}={\rm white}} \sum_{s=1}^{6} \mathcal{P}_s(\vec{w})\,, \tag{3.20}$$

where the lattice spacing a is defined to be the distance between nearest-neighbor sites, i.e. the length of each gauge link on the lattice. The sum in H_B over 6 plaquettes, $\mathcal{P}_s(\vec{w})$, for each white lattice site includes all plaquettes on the lattice. Specifically, there is one of each type of plaquette (non-red, non-green, etc.) associated with each white site, and we use the subscript s to identify the color that is absent from the plaquette.

Any eigenstate of H_E is fully defined by providing the quantum numbers for every gauge link on the triamond lattice, j_1, j_2, j_3, …, j_N. Our shorthand for an eigenstate is $|\{j\}\rangle$. The

diagonal matrix elements of the Hamiltonian are

$$\langle\{j\}|\, H_E \,|\{j\}\rangle = \frac{8\sqrt{2}g^2}{3a} \sum_{n=1}^{N} j_n(j_n+1)\,, \tag{3.21}$$

and the off-diagonal matrix elements from initial state $|\{j\}\rangle$ to final state $|\{J\}\rangle$ come from Eq. (3.20) with

$$\begin{aligned} \langle\{J\}|\, \mathcal{P}_s(n) \,|\{j\}\rangle \;\; &= \;\; \prod_{\text{sites}} (-1)^{j_e+j_f+\frac{1}{2}+J_b} \sqrt{2J_f+1} \\ &\qquad \sqrt{2j_b+1} \begin{Bmatrix} j_e & j_f & j_b \\ \frac{1}{2} & J_b & J_f \end{Bmatrix}, \end{aligned} \tag{3.22}$$

where the right-hand side has a standard $6j$ symbol and the product includes the 10 sites in order around the plaquette. For SU(2), either direction around the plaquette gives the same result. There are three links at each site, one external to the plaquette (subscript e), one in the forward direction around the plaquette (subscript f), and one in the backward direction around the plaquette (subscript b). Eq. (3.22) is not specific to the triamond lattice and has been obtained previously by other authors [86, 87].

3.2.3 Computations on the Triamond Unit Cell

As shown in Fig. 3.4, a unit cell contains 12 gauge links. By using periodic boundary conditions, a single unit cell becomes a viable three-dimensional lattice having exactly three gauge links touching each site. If each SU(2) gauge link is truncated to just two basis states, $j = 0$ and $j = \frac{1}{2}$, the unit cell accommodates $2^{12} = 4096$ basis states.

A simple way to begin exploring this theory is to use the variational method, which will find the lowest energy state among all states that couple to a selected ansatz. Fig. 3.5 shows three energy eigenstates obtained from three different ansatze, each having just one variational parameter. (We name the parameter θ in every case, but they are three different parameters.) Each of these examples is successful in finding a true eigenstate of the Hamiltonian. The 12-qubit quantum circuits that produced these results can be found in the methodology section.

To gain more intuition, notice that there is no 10-sided path inside a unit cell. This means any plaquette operator will wrap around the lattice and touch one of the gauge links twice, thus changing that value of j twice. With our truncation to $j \in \{0, \frac{1}{2}\}$, this means only 8 gauge links are changed when a plaquette operator is applied to the single-cell lattice.

For example, begin with $j = 0$ on all 12 links (called the bare vacuum) and then apply a

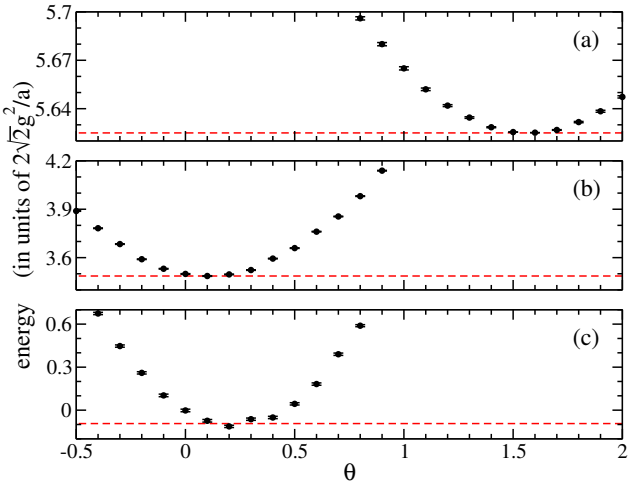

Figure 3.5: **Three energy eigenvalues for one unit cell of the triamond lattice.** Panels (a), (b) and (c) correspond to the third excited state, the first excited state, and the ground state respectively. The gauge coupling is $g = 1$ and periodic boundary conditions are used in all directions. Each data point was obtained by running qiskit code with 10^4 shots on the `ibm_qasm` noiseless simulator. Error bars are standard deviations. For comparison, red dashed lines show the true eigenvalues.

non-red plaquette. The non-red plaquette touches one of the cyan links twice while avoiding the other cyan link, thus producing a state with $j = 0$ for all red and cyan links but $j = \frac{1}{2}$ for the 8 other links. If we had applied a non-cyan plaquette instead, the result would have been exactly the same because it touches one of the red links twice. Similarly, the non-green and non-magenta plaquettes are identical to each other ($j = 0$ for green and magenta but $j = \frac{1}{2}$ for the 8 other links), and the non-blue and non-yellow plaquettes are identical to each other ($j = 0$ for blue and yellow but $j = \frac{1}{2}$ for the 8 other links).

In fact, any number of plaquette operators can be applied to the bare vacuum one after the other in any order, and the final state will always be one of these four basis states: the bare vacuum, the non-red non-cyan plaquette, the non-green non-magenta plaquette and the non-blue non-yellow plaquette. The part of the Hamiltonian matrix that governs these four states is

$$H_{\text{vac}} = \frac{2\sqrt{2}g^2}{a} \begin{pmatrix} 0 & \frac{-1}{2g^4} & \frac{-1}{2g^4} & \frac{-1}{2g^4} \\ \frac{-1}{2g^4} & 8 & \frac{-1}{32g^4} & \frac{-1}{32g^4} \\ \frac{-1}{2g^4} & \frac{-1}{32g^4} & 8 & \frac{-1}{32g^4} \\ \frac{-1}{2g^4} & \frac{-1}{32g^4} & \frac{-1}{32g^4} & 8 \end{pmatrix}. \tag{3.23}$$

Of the 4096 basis states for the periodic unit cell, only 32 obey Gauss's law. The requirement of Gauss's law is that each site has either all three gauge links with $j = 0$ or exactly one gauge link with $j = 0$. Because the triamond lattice is symmetric under color interchanges,

the 32×32 Hamiltonian for Gauss-compliant states can be block diagonalized into eight 4×4 blocks, including the one shown explicitly in Eq. (3.23). Each of the 32 states has exactly 0, 4, 6 or 8 of the gauge links with $j = \frac{1}{2}$. From top to bottom, the three examples in Fig. 3.5 are dominated by a state where the number of gauge links with $j = \frac{1}{2}$ is 6, 4 and 0 respectively. In particular, the bottom panel of Fig. 3.5 is showing the true ground state of the theory, which is built from four basis states.

Block diagonalizing the Hamiltonian is simple enough for such a small lattice, but phenomenological applications will require lattices with more than a single unit cell, and this is where the Hilbert space grows rapidly. A lattice with N unit cells will have $12N$ gauge links. Truncating each link to $j \in \{0, \frac{1}{2}\}$ leads to 2^{12N} basis states, and the ground state is built from 2^{4N-2} of them. Larger lattices are where the variational method, imaginary time evolution, and other algorithms implemented with error mitigation on quantum computers have the potential to be of great value.

3.2.4 Triamond Imaginary Time Evolution

When future computations are performed on triamond lattices, a typical first step will be to prepare the interacting vacuum. Imaginary time evolution is a reliable method for doing so, but it is only practical if error mitigation methods are able to account for the hardware errors. As a first confirmation of self-mitigation for triamond lattices, consider a single unit cell with periodic boundary conditions. The Hamiltonian matrix is Eq. (3.23), which can be written as

$$\begin{aligned}\hat{H}_{\text{vac}} &= \frac{2\sqrt{2}g^2}{a}\Big(6 - 2(\hat{Z}_0 + \hat{Z}_1) - 2\hat{Z}_1\hat{Z}_0 \\ &\quad -\frac{17}{64g^4}(\hat{X}_0 + \hat{X}_1 + \hat{X}_1\hat{X}_0) \\ &\quad -\frac{15}{64g^4}(\hat{Z}_1\hat{X}_0 + \hat{X}_1\hat{Z}_0 - \hat{Y}_1\hat{Y}_0)\Big)\,. \end{aligned} \tag{3.24}$$

This is similar to the Hamiltonian for square plaquettes given in Eq. (3.1), but with different coefficients and additional terms. We adapted our code from the square plaquette study to handle the triamond case, obtaining the results displayed in Fig. 3.6. Perhaps surprisingly, the unmitigated results are moving away from the true value already at the very first step of imaginary time. Notice, however, that we are performing a particularly difficult computation: the pure noise limit is at a height of 6 (far beyond the top of the graph) while the true result is only slightly below zero. This means the true result contains a delicate cancellation between the large first term in Eq. (3.24) and the sum of all other terms.

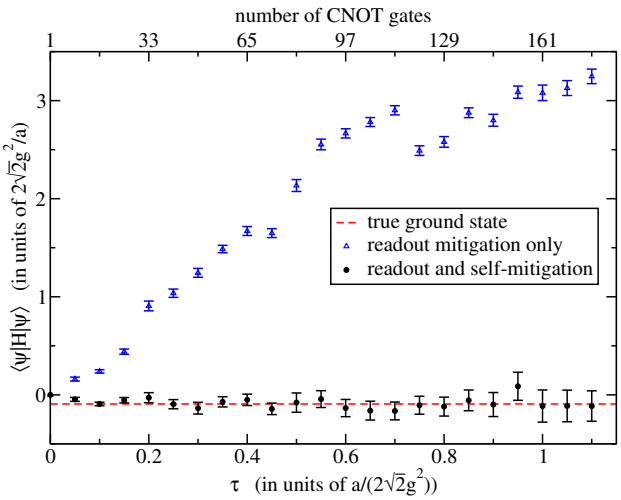

Figure 3.6: **Quantum imaginary time evolution on a triamond lattice.** These results are for SU(2) gauge theory with $j_{\max} = \frac{1}{2}$ on a triamond unit cell with periodic boundaries in all three spatial directions. The gauge coupling is $g = 1$ and the time step is $\Delta\tau = 0.05$ in units of $a/(2\sqrt{2}g^2)$. Each quantum circuit uses between 32 and 50 randomized compilings with 2000 shots per compiling. All quantum computations were performed on `ibm_brisbane`. Black data points use self-mitigation and blue data points do not. Error bars are 95% confidence intervals. The true ground state is shown as a red dashed line.

As expected, the unmitigated data points in Fig. 3.6 are approaching the pure noise limit as imaginary time increases. Fluctuations in that approach are observed and were expected because the computation at each time step was usually performed hours or days after the previous time step, and was run on whichever qubits were performing best at that time. In contrast, the self-mitigated results arrive at the correct value after two steps of imaginary time and remain in agreement for the duration of our computations. Even the fluctuations evident in the unmitigated results are handled nicely by self-mitigation, with no visible effect remaining in the self-mitigated data.

For $\tau < 0.7$ in the units of Fig. 3.6, we used 50 randomized compilings. As τ increased beyond 0.7, the number of randomized compilings was reduced linearly to just 32 randomized compilings at $\tau = 1.1$. No sensitivity to this choice is observed in the results.

It is also worth noticing a significant difference between the two quantum computers we have used in this work. The square plaquette results in Fig. 3.3 ran on `ibm_lagos` where the CNOT gate is a native gate, but our triamond results in Fig. 3.6 ran on `ibm_brisbane` where CNOT gates are not native and are constructed from the echoed cross-resonance (ECR) gate. Self-mitigation has been tailored specifically to an ECR device by other authors [101] but our code is written in terms of CNOT gates (see Table 3.1), and it is encouraging to observe that a CNOT-based self-mitigation code performs well on the ECR device also.

Table 3.1: **The 16 options for randomized compiling.** Each of the 16 rows in this table is equivalent to a single CNOT gate on error-free hardware. On noisy hardware, randomly selecting from these rows is valuable for error mitigation. See the discussion in the methodology section.

Applied before the CNOT		Applied after the CNOT	
control	target	control	target
I	I	I	I
I	X	I	X
I	Y	Z	Y
I	Z	Z	Z
X	I	X	X
X	X	X	I
X	Y	Y	Z
X	Z	Y	Y
Y	I	Y	X
Y	X	Y	I
Y	Y	X	Z
Y	Z	X	Y
Z	I	Z	I
Z	X	Z	X
Z	Y	I	Y
Z	Z	I	Z

3.3 Discussion

In this work, SU(2) gauge theory has been truncated to $j \in \{0, \frac{1}{2}\}$ and studied on small lattices.

Self-mitigation has allowed the QITE algorithm [98] to find the ground state of a lattice with two square plaquettes on an IBM quantum computer. As shown in Fig. 3.3, the computation without self-mitigation did not attain the correct ground state. The basic effect of self-mitigation is a rescaling of expectation values, where raw results from the physics circuit are divided by results from a mitigation circuit according to Eqs. (3.9) and (3.10). The Hamiltonian's expectation value is a linear combination of the individual rescaled expectation values, leading to the large improvement observed in Fig. 3.3 where, from an initial value of zero, the self-mitigated and unmitigated results ultimately move in opposite directions. The unmitigated result is approaching the pure noise limit while the self-mitigated result finds the true value quickly and remains consistent with it.

The error bars in Fig. 3.3 are statistical only, and self-mitigation has clearly handled the dominant systematic error. The mitigated result at $\tau = 1.3$ happens to be furthest from

the true ground state, being several standard deviations away, but subsequent time steps agree nicely with the true ground state. This demonstrates a valuable feature of the QITE algorithm. Output from one time step is needed as input for the following step, and yet the algorithm recovers quickly from an outlier.

The application of QITE to a larger lattice will require more terms in the expression for $\hat{A}$ in Eq. (3.5), leading to more expectation values that need to be computed. However, the expression for $\hat{A}$ will generally not require all possible Pauli strings but is instead governed by the correlation length of the physics under consideration [98]. It will be interesting to see future studies that use self-mitigated QITE to examine non-Abelian gauge theories on larger lattices.

The triamond crystal offers a systematic way to define three-dimensional lattices. Because there are only three gauge links touching each lattice site, the quantum numbers of the links themselves are sufficient to fully define any basis state of the lattice. This is not true for a simple cubic lattice [90]. In fact, the triamond lattice is the only highly symmetric lattice that achieves this goal in three dimensions. To be more precise, the triamond lattice is the only three-dimensional lattice that is strongly isotropic and has three gauge links per site [107]. Strong isotropy refers to the fact that rotation (or reflection) of the lattice around any site can interchange any pair of links at that site while leaving the physical structure of the entire lattice invariant [107]. In particular, a simple cubic lattice is not strongly isotropic [107, 110].

Another interesting glimpse into the symmetries of the triamond lattice comes from noticing that the six vectors comprising a triamond lattice form a regular tetrahedron. Begin with one gauge link of each color (recall Eqs. (3.11) and (3.12)) and translate each one spatially without any rotations. The red, green and blue links will form the equilateral triangular base of the tetrahedron. The cyan, magenta and yellow links rise from the corners of that base to meet at the top of the tetrahedron. As might be expected from the sentences preceding Eq. (3.23), the cyan link of the tetrahedron touches all links except the red one, the magenta link touches all but green, and the yellow link touches all but blue.

For eyes used to seeing cubic lattices, the triamond might seem difficult to visualize. However, our derivation shows that the SU(2) Hamiltonian has the familiar form of a sum over just a few plaquette orientations, in this case six, and our quantum circuits for obtaining ground and excited states (see Figs. 3.7 and 3.8) are quite simple due to the triamond symmetries. The triamond lattice has only the expected parameters, namely the gauge coupling and the lattice volume, but it provides extra gauge links inside a unit cell, representing a smaller lattice spacing and a new trajectory for approaching the continuum limit of a gauge theory.

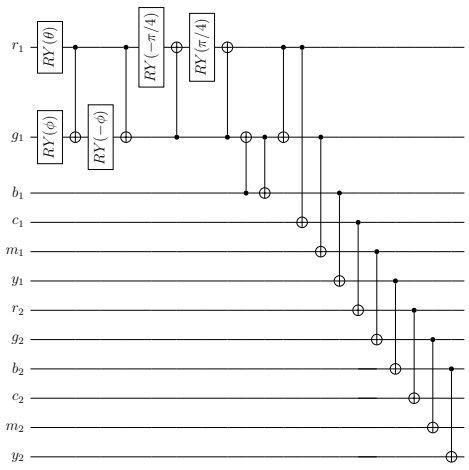

Figure 3.7: **The circuit used to obtain the ground state eigenvalue.** The 12 qubits are labeled by their colors, with two copies of each color appearing in the list. A constant angle is defined by $\phi = \arccos(1/\sqrt{3})$. The ground state eigenvalue for one unit cell of the triamond lattice is displayed in Fig. 3.5(c).

Fig. 3.6 shows the successful application of imaginary time evolution to a lattice in three spatial dimensions. The result is a robust preparation of the ground state. The triamond framework offers a systematic path toward larger lattices and relaxed truncations of the gauge theory. Future work in this direction can continue the progress toward a practical implementation of lattice gauge theories on quantum computers.

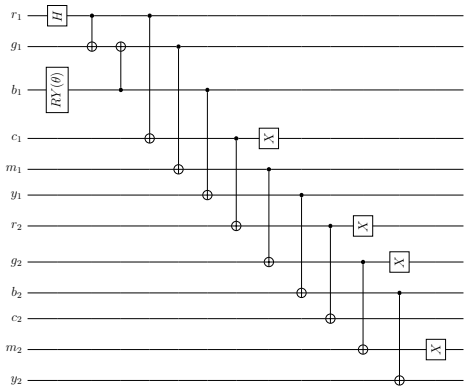

Figure 3.8: **The circuit used to obtain the first excited state eigenvalue.** The 12 qubits are labeled by their colors, with two copies of each color appearing in the list. The first excited state eigenvalue for one unit cell of the triamond lattice is displayed in Fig. 3.5(b).

Chapter 4

False Vacuum Decay in a Non-Abelian Gauge Theory on a Triamond Lattice

The content of this chapter is a direct reproduction of [10].

4.1 Introduction

The classic picture of false vacuum decay is a double-well potential energy function where the shallower well (called the false vacuum) is separated from the deeper well (called the true vacuum) by an energy barrier [4, 113]. A system that begins in the false vacuum can later be found in the true vacuum with some probability. For the corresponding scenario in a quantum field theory, the decay rate can be calculated by using a semiclassical approximation and imaginary time, but that approach does not explain the physical mechanism of the decay.

In contrast, real-time simulations would allow direct observation of the vacuum decay mechanism, perhaps showing bubbles of true vacuum appearing and nucleating to displace the false vacuum. Various approaches are being explored by several authors [5, 114, 36, 115, 29, 116], including quantum simulations of Ising models [117, 118, 119, 120, 121] and the Schwinger model [122]. In the present work, we take a first step toward using a non-Abelian lattice gauge theory for the real-time simulation of false vacuum decay. We use a pure gauge theory; no matter fields are required.

Lattice gauge theory is a direct computational method for calculations in non-Abelian theories such as quantum chromodynamics (QCD). Computations of the masses, decay constants and form factors of QCD hadrons have become precision results of the utmost importance to the particle and nuclear physics communities [27, 17]. The starting point for standard computations is a four-dimensional Euclidean spacetime lattice that provides convenient access to imaginary time calculations but no access to real-time simulations.

A promising approach to real-time physics is to rewrite the theory as a Hamiltonian problem, keeping time as a continuous variable and discretizing only the spatial components onto a three-dimensional lattice [26]. The length of the state vector grows exponentially with the lattice size but, in principle, it can be stored efficiently in the qubit register of a quantum computer [74]. Unfortunately, the non-Abelian version of Gauss's law must now be imposed as a constraint that is external to the Hamiltonian, and finding the best approach to this issue is a high-priority topic for several research groups [40, 123, 124, 125, 83, 126, 127, 128, 129, 130, 131, 132, 133, 134]. Nevertheless, non-Abelian theories have already been put successfully onto quantum computers [13, 14, 15, 47, 49, 135, 50, 136, 48, 51, 52, 53, 54, 9, 137, 96, 138, 139, 140], though the lattices are necessarily small and typically have just one or two spatial dimensions.

In three dimensions, each site on a cubic lattice is touched by six gauge links, pointed in directions $\pm\hat{i}$, $\pm\hat{j}$, $\pm\hat{k}$ along the standard Cartesian axes. There are multiple ways that six specified SU(2) representations can be combined to satisfy Gauss's law. This means additional qubits are required at each site to define the partial sums needed for a complete definition of the quantum state. The triamond lattice is an alternative that spans three-dimensional space and yet has only three gauge links touching each site [9]. This means the triamond gauge fields are fully defined by the gauge link qubits with no need for extra qubits at the sites. The triamond lattice is strongly isotropic [163, 164, 9] and provides an efficient way to build a three-dimensional lattice gauge theory. A similar approach in two dimensions leads to hexagonal lattices [90, 93, 147].

In the absence of matter fields, gauge invariance requires any flow of non-Abelian charges (such as the colors of QCD) to form closed paths on the lattice. Localized particles called glueballs are gauge-invariant objects described by a superposition of localized paths. If the lattice has periodic boundary conditions, there can also be paths that go all the way around the lattice to close on themselves from behind as shown in Fig. 4.1, and these are called torelons [11, 141, 142, 12, 143, 144, 145, 146]. A torelon is a closed path of color flux that is not homotopic to a point. Torelons become nondynamical heavy states as the lattice volume is taken to infinity, but on small lattices they are central to the physics.

In SU(2) gauge theory with periodic boundary conditions, the presence or absence of a torelon in the $\hat{i}$ direction is a good quantum number, and the same is true for the $\hat{j}$ direction and the $\hat{k}$ direction. A pair of torelons along the same direction can annihilate each other, but a single torelon cannot disappear. Torelons can move across the lattice and interact with each other through the SU(2) gauge fields. A pair of torelons along two different directions cannot annihilate each other but they can combine to form a bound state that we will call a diagonal torelon, corresponding to a single path winding around the lattice in both of the

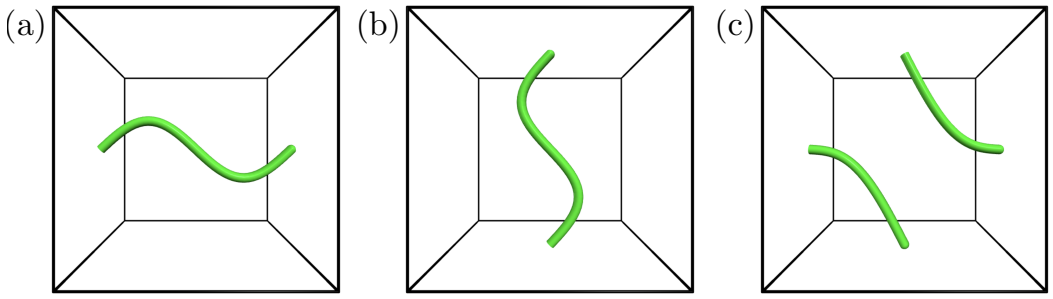

Figure 4.1: Closed path of round-the-world color flux, called a torelon, in a cubic spatial volume with periodic boundary conditions. (a) One horizontal torelon. (b) One vertical torelon. (c) One diagonal torelon.

original directions before returning to itself, as shown in Fig. 4.1(c).

For a universe containing just one torelon (suppose it is a diagonal torelon in the $\hat{i}$ and $\hat{k}$ directions) the ground state has no objects other than the stationary torelon. That diagonal torelon has the same quantum numbers as a pair of separated torelons, one in each of the $\hat{i}$ and $\hat{k}$ directions, but this two-torelon state has higher energy. If the universe is periodic in all three directions, then the ground state is stable. However, a twisted boundary condition in the $\hat{j}$ direction means $\hat{i}$ and $\hat{k}$ become interchanged for an object that travels completely around the $\hat{j}$ direction. This means the diagonal torelon state (false vacuum) can decay to a no-torelon state (true vacuum) and that these two states are separated by the two-torelon state (energy barrier). This is the false vacuum decay process that will be investigated in the present work.

Section 4.2 defines SU(2) gauge theory on a triamond lattice, explaining the specific geometry that will be used for the current study and how it can be mapped to a ladder of square paths. Section 4.3 examines the spectrum of torelon states on a triamond lattice of three unit cells, discussing the subtle relationship between energy and momentum. Section 4.4 presents our method for running quantum imaginary time evolution on an IBM quantum computer for a lattice with 12 square plaquettes, shows the results of those quantum computations, and contemplates the extension to a triamond lattice. Section 4.5 contains our use of real-time evolution to study false vacuum decay, which is built on the fact that the triamond lattice is truly three-dimensional. Section 4.6 provides an outlook toward possible next steps.

4.2 The triamond lattice

A primary motivation for choosing a triamond lattice rather than a cubic lattice is to reduce the number of gauge links touching each site from 6 to 3 [9]. Having only three gauge links

at a site means the combined SU(2) value of any pair of links is determined uniquely by the value of the third gauge link. In contrast, the combined SU(2) value of two links on a cubic lattice is not unique because the other four links can be combined in many ways, and this means extra qubits would be required at each lattice site to fully specify the quantum state.

The triamond lattice used in this work is shown in Fig. 4.2(a). To view a triamond lattice from many different vantage points, please see our two-minute video [157]. At each lattice site, the three gauge links lie in a plane and are equally spaced. The plane at a lattice site is always orthogonal to the line connecting opposite corners of a unit cell, which means there are four different planes in a triamond lattice. The lattice sites in Fig. 4.2 are shown in white, red, green and blue to label the plane at each site.

In a cubic lattice all gauge links are on the edges of a unit cell, but the triamond lattice is not so sparse and has gauge links inside each unit cell. Specifically, every gauge link lies along one of the following six directions,

$$\hat{r} = \frac{\hat{j} - \hat{k}}{\sqrt{2}}, \qquad \hat{g} = \frac{\hat{i} - \hat{j}}{\sqrt{2}}, \qquad \hat{b} = \frac{\hat{k} - \hat{i}}{\sqrt{2}},$$

$$\hat{c} = \frac{\hat{j} + \hat{k}}{\sqrt{2}}, \qquad \hat{m} = \frac{\hat{i} + \hat{j}}{\sqrt{2}}, \qquad \hat{y} = \frac{\hat{k} + \hat{i}}{\sqrt{2}}, \tag{4.1}$$

corresponding respectively to the red, green, blue, cyan, magenta and yellow gauge links in Fig. 4.2 with $\hat{i}$, $\hat{j}$ and $\hat{k}$ being the standard orthonormal unit vectors.

Because of the periodic boundaries, all connections between gauge links in Fig. 4.2(a) can be shown in a flat map as displayed in Fig. 4.2(b). The map has the form of a 12-rung ladder that is periodic only in the horizontal direction. For example, the links along one side of the ladder (numbered from 1 to 12 in Fig. 4.2) lie on a corkscrew trajectory around the periodic triamond lattice.

On a large triamond lattice the smallest closed paths are 10-sided, and several examples can be found in Fig. 4.2(a). They are called elementary plaquettes. Every elementary plaquette omits one of the gauge link directions from Eq. (4.1) but includes two links in each of the other five directions. Any triamond lattice comprising N unit cells has $12N$ gauge links and $12N$ elementary plaquettes.

On our small triamond lattice, some of the elementary plaquettes wrap around a periodic boundary and affect the same link twice. In the special case where the twice-affected link retains its original value, the result is pair creation of two torelons that we will refer to as an 8-sided plaquette. Figure 4.2(c) shows examples of 10-sided and 8-sided plaquettes.

The Hamiltonian of SU(2) gauge theory is a sum of a color-electric term and a color-

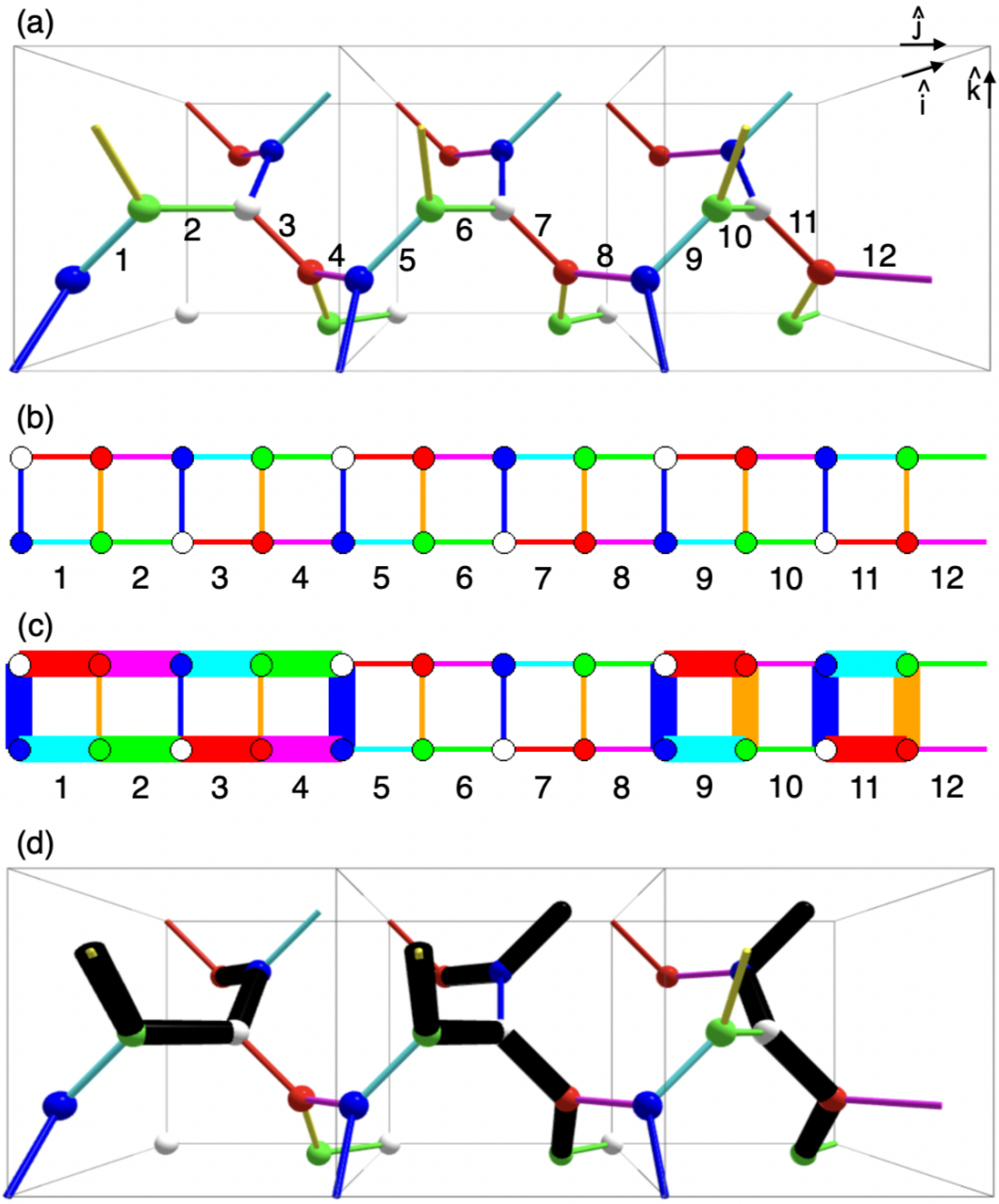

Figure 4.2: (a) Triamond lattice comprising three unit cells with periodic boundary conditions in all three directions. Twelve of the 36 gauge links are numbered so they can be referenced in the text. (b) A flattened map of the same triamond lattice with the same 12 labels. (c) The same flattened map with two plaquettes shown in thick lines, namely a 10-sided plaquette at 1,2,3,4 and an 8-sided plaquette at 9,11. (d) Thick black paths show a horizontal, diagonal and vertical torelon in the left, center and right unit cells, respectively.

magnetic term [9],

$$H_{\text{triamond}} = H_E + H_B, \tag{4.2}$$

with

$$H_E = \frac{8\sqrt{2}a^3g^2}{3} \sum_{n=\text{links}} \text{Tr}\left(E_x^2(n) + E_y^2(n) + E_z^2(n)\right), \tag{4.3}$$

$$H_B = -\frac{2\sqrt{2}}{g^2 a} \sum_{\vec{w}=\text{white}} \sum_{s=1}^{6} \mathcal{P}_s(\vec{w}), \tag{4.4}$$

where g is the SU(2) coupling and a is the lattice spacing, i.e. the length of each gauge link. The sum in the color-electric term runs over all gauge links on the lattice, with $\vec{E}$ representing the color-electric field. The double sum in the color-magnetic term runs over all plaquettes on the lattice, organized here as six plaquettes per white site as described in Ref. [9]. In particular, $\mathcal{P}_s(\vec{w})$ is the trace of the product of gauge links around the s'th plaquette at white site $\vec{w}$.

Any eigenstate of the color-electric Hamiltonian is fully defined by the SU(2) quantum numbers of the individual gauge links, j_1, j_2, j_3, ..., j_{12N}. In terms of these states, the diagonal matrix elements of the Hamiltonian are

$$\langle\{j\}|\, H_E \,|\{j\}\rangle = \frac{8\sqrt{2}g^2}{3a} \sum_{n=1}^{12N} j_n(j_n+1) \tag{4.5}$$

and the off-diagonal matrix elements are obtained from a product over all lattice sites on the perimeter of a plaquette,

$$\langle\{J\}|\, \mathcal{P}_s(\vec{w}) \,|\{j\}\rangle = \prod_{\text{perimeter}} (-1)^{j_e+j_f+J_b} \sqrt{2J_f+1} \sqrt{2j_f+1} \begin{Bmatrix} j_e & j_f & j_b \\ \frac{1}{2} & J_b & J_f \end{Bmatrix}, \tag{4.6}$$

which matches the definition in Ref. [90] and differs from Refs. [86, 87, 9] by a factor of $(-1)^{1/2}$ inside the product.

The continuous SU(2) symmetry means each gauge link has an infinite basis of options, $j \in \{0, \frac{1}{2}, 1, \frac{3}{2}, 2, \ldots\}$. Use of a finite number of qubits necessitates a truncation, and in the present work we retain only $j \in \{0, \frac{1}{2}\}$ which corresponds to one qubit per gauge link. Gauss's law restricts the options at every lattice site and allows the complete state of the lattice in Fig. 4.2 to be determined with only 13 qubits. A specific choice is the 12 numbered

gauge links plus any single link from the other side of the ladder. This Hilbert space has dimension 2^{13} and consists of two orthogonal sectors according to the presence or absence of a torelon in the long $\hat{j}$ direction. Because long torelons correspond to heavy states, we will focus on the sector without a $\hat{j}$ torelon. This leaves us with a Hilbert space of dimension 2^{12} that is spanned by just the 12 numbered gauge links of Fig. 4.2.

The mapping of a triamond lattice to a ladder of square paths is quite convenient. The three-dimensional aspects of the triamond lattice appear through the 10-sided and 8-sided plaquettes that involve more than just nearest-neighbor interactions among the squares.

4.3 The torelon spectrum

Construction of the explicit 4096×4096 Hamiltonian matrix for the triamond lattice having three unit cells allows a direct determination of all eigenvalues and eigenvectors by standard classical computing methods. The smallest eigenvalues are displayed in Fig. 4.3 for a specific choice of the gauge coupling. Important insights can be gained by examining and interpreting the corresponding eigenstates.

To begin, notice that the vacuum state is significantly lighter than all other states, as expected. In the strong-coupling limit the vacuum would have an energy of zero, but away from that limit it is pushed somewhat below zero. The vacuum state is dominated by the bare vacuum where every gauge link has $j = 0$, and the leading corrections arise from linear combinations of single-plaquette terms that are translationally invariant on the lattice.

The first excited state is degenerate and represents one zero-momentum torelon in either of the two short directions on the lattice, $\hat{i}$ or $\hat{k}$. There are six locations for a horizontal torelon, and the groupings into six momentum states are evident in Fig. 4.3. Degeneracies within the horizontal sector are due to the equal energies of forward and backward momenta.

All energies in the vertical torelon sector are identical to the horizontal case because of a lattice symmetry. To be precise, it is a screw symmetry that rotates the lattice by $\pi/2$ around $\hat{j}$ while also pushing it forward in the $\hat{j}$ direction by $\frac{1}{4}$ of a unit cell. On the ladder map in Fig. 4.2, the screw symmetry is a shift by one square.

The lowest energy state of a diagonal torelon is translationally invariant and represents a diagonal torelon with zero momentum. Relative to the vacuum, the diagonal torelon energy is less than the sum of a horizontal torelon and a vertical torelon, which is expected for sufficiently large gauge coupling because a pair of basic torelons needs eight gauge links whereas a diagonal torelon needs only six. This is a reminder that some of the excited states in the diagonal torelon sector of Fig. 4.3 can have a large overlap with a pair of spatially separated torelons.

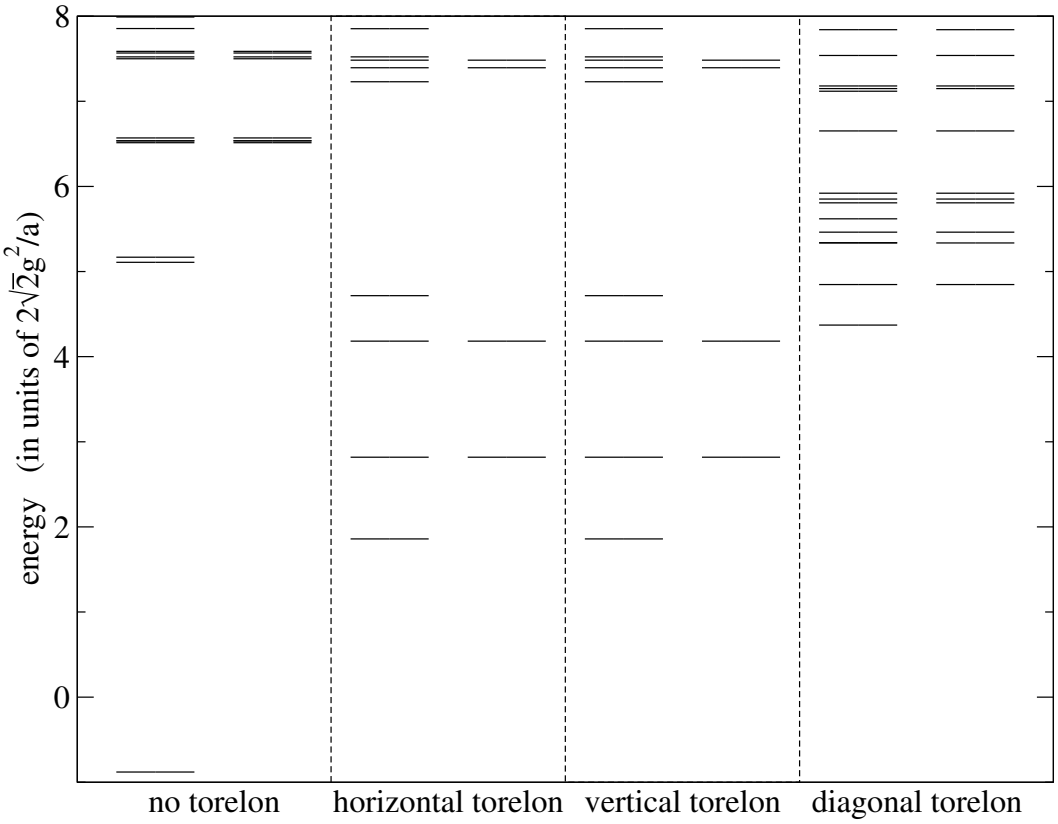

Figure 4.3: Smallest eigenvalues of SU(2) gauge theory on a triamond lattice having three unit cells in a row and periodic boundary conditions. The gauge theory is truncated such that each gauge link has $j \in \{0, \frac{1}{2}\}$ and the gauge coupling is $g = 1.3$. Numerical values from this graph are provided in Appendix B.

The 12 lowest energy states in the diagonal torelon sector tell an important story about how momentum is handled on a triamond lattice. These 12 lowest states are the energy eigenstates that correspond to placing a diagonal torelon at any of the 12 allowed positions on the lattice. In the ladder map of Fig. 4.2(b), they appear as superpositions of a single six-link rectangle at each of the 12 possible locations. Notice that half of these rectangles are doubly blue and nonyellow while the other half are nonblue and doubly yellow.

The translation along the 12-step ladder of Fig. 4.2(b) involves a $\pi/2$ rotation with each step along the $\hat{j}$ direction and is called a screw translation. The Fourier transform of this screw translation results in eigenstates of screw momentum that are also eigenstates of energy, and these are precisely the states shown in Fig. 4.3. Importantly, the 12 values of screw momentum contain six values of linear momentum for the nonyellow torelons and six values for the nonblue torelons. On the original triamond lattice, the nonblue torelon lies along a lattice diagonal that is spatially orthogonal to the nonyellow torelon. A nonblue torelon path is sketched in Fig. 4.2(d).

Excited states in the no-torelon sector include the momentum states of various operators. To see detailed numerical results for energy eigenvalues and eigenvectors from all sectors of Fig. 4.3, please consult App. B.

4.4 Imaginary time evolution

Real-time evolution is a central goal for the quantum computation of gauge theories, but it requires creation of an appropriate initial state. Imaginary time evolution is a valuable method for creating the initial state. Here we implement a successful determination of the ground state on 12 qubits of the IBM_BRISBANE quantum computer for a simplified SU(2) Hamiltonian. This success provides insight into the practical challenge of coding a triamond lattice into a quantum computer that has limited connectivity among its qubits.

Although the triamond lattice for three unit cells can be mapped onto the ladder of Fig. 4.2(b), the three-dimensional nature of the triamond structure remains evident through the large plaquettes shown in Fig. 4.2(c). A simpler system is obtained by using the ladder directly as a quasi-one-dimensional lattice having only square plaquettes and no connection to the three-dimensional triamond structure. This ladder of simple square plaquettes has been used in several quantum computations for SU(N) gauge theory [13, 14, 15, 47, 49]. Imaginary time evolution [98] for a nonperiodic ladder of only three rungs was run on a quantum computer recently [9]. Here we will study the 12-rung periodic ladder.

In units of $2/g^2$, the SU(2) Hamiltonian for square plaquettes with gauge coupling $x =$

$2/g^4$ is

$$\begin{aligned} H_\square &= \frac{27}{2} - \frac{3}{8}\sum_{j=1}^{12}(2Z_j + Z_jZ_{j+1}) \\ &\quad -\frac{x}{8}\sum_{j=1}^{12}(9 + 3Z_{j-1} + 3Z_{j+1} + Z_{j-1}Z_{j+1})X_j, \end{aligned} \tag{4.7}$$

where X_j and Z_j are Pauli gates acting on the jth qubit. Imaginary time evolution from any initial state is

$$|\Psi(\tau)\rangle = e^{-\tau H_\square}|\Psi(0)\rangle = r' e^{-i\tau A}|\psi\rangle, \tag{4.8}$$

where the normalizing factor can be obtained from

$$r' = r(1 - \tau\langle\psi|H_\square|\psi\rangle) + O(\tau^2). \tag{4.9}$$

Because the Hamiltonian is purely real, the matrix A must be purely imaginary. This means each term has an odd number of Y gates. For a two-qubit Hamiltonian, the most general expression is

$$\begin{aligned} A &= a_{iy}Y_1 + a_{xy}X_2Y_1 + a_{zy}Z_2Y_1 \\ &\quad + a_{yi}Y_2 + a_{yx}Y_2X_1 + a_{yz}Y_2Z_1. \end{aligned} \tag{4.10}$$

For the 12-qubit Hamiltonian of Eq. (4.7), the most general expression has many terms but we might expect only a subset of them to dominate the physics. In particular, since $H_\square$ has only single-qubit terms, adjacent-pair terms, and adjacent-triple terms, we anticipate that A will be predominantly local. Specifically, the single-qubit and adjacent-pair terms are expected to be most important, with adjacent-triple terms being less important. Since adjacent-triple terms would require swap gates when implemented on IBM's heavy-hex hardware architecture, we propose to neglect these subleading terms. Therefore our ansatz has only single-qubit and adjacent-pair terms,

$$\begin{aligned} A &= \sum_{j=1}^{12}\Big((a_y)_jY_j + (a_{xy})_jX_{j+1}Y_j + (a_{zy})_jZ_{j+1}Y_j \\ &\quad + (a_{yx})_jY_jX_{j-1} + (a_{yz})_jY_jZ_{j-1}\Big). \end{aligned} \tag{4.11}$$

Notice that each qubit j gets its own set of coefficients $(a_\bullet)_j$, thus allowing our error mitigation to make no assumption about individual physical qubits having similar noise profiles. The

coefficients $(a_\bullet)_j$ are determined from state tomography as explained in detail in Appendix C. The exponentiation of each term in A is accomplished by using

$$e^{-i\theta Y_j} = RY_j(2\theta), \tag{4.12}$$

$$e^{-i\theta X_j Y_k} = CX_{kj} RY_k(2\theta) CX_{kj}, \tag{4.13}$$

$$e^{-i\theta Z_j Y_k} = CX_{jk} RY_k(2\theta) CX_{jk}. \tag{4.14}$$

The complete time evolution $e^{-i\tau A}|\psi\rangle$ can be constructed as a second-order Trotter circuit with terms ordered in a way that minimizes the number of entangling gates, as shown in Fig. 4.4. Notice that CNOT gates at the end of a time step (right edge of the figure) will cancel with CNOT gates at the beginning of the next time step (left edge of the figure). The rotation angles in the circuit are

$$\alpha_j = (a_y)_j \Delta\tau, \tag{4.15}$$

$$\beta_j = (a_{yx})_j \Delta\tau, \tag{4.16}$$

$$\gamma_j = (a_{xy})_j \Delta\tau, \tag{4.17}$$

$$\delta_j = (a_{yz})_j \Delta\tau, \tag{4.18}$$

$$\epsilon_j = (a_{zy})_j \Delta\tau, \tag{4.19}$$

and their numerical values are different at each time step in the quantum circuit. Values from previous time steps are stored in a list for reuse, and values for the new time step are computed from the previous time steps according to Appendix C.

The heavy-hex layout of IBM_BRISBANE provides precisely the loop of 12 qubits that is required for this computation. Because of noisy hardware, a direct computation with mitigation of readout errors, which means mitigation for the final measurement of each qubit, was unable to obtain the true ground state, as shown in Fig. 4.5. Self-mitigation was found to overcome this problem for two-qubit computations in Ref. [9], and Fig. 4.5 shows that it is equally successful in the 12-qubit case.

The basic idea of self-mitigation [15] is to create a mitigation circuit that is very similar to the physics circuit. The true result of the mitigation circuit is known in advance, so running that circuit determines the errors being made by the hardware. The measured errors are then used to rescale the original physics circuit of interest. Specifically, if the physics circuit has N steps forward in time, then the mitigation circuit has $N/2$ steps forward followed by $N/2$ steps backward, thus arriving at the initial state modulo hardware errors. An odd number for N presents no problem because we are using second-order Trotter steps, which means each step is already symmetric as seen in Fig. 4.4 and can therefore readily be made half

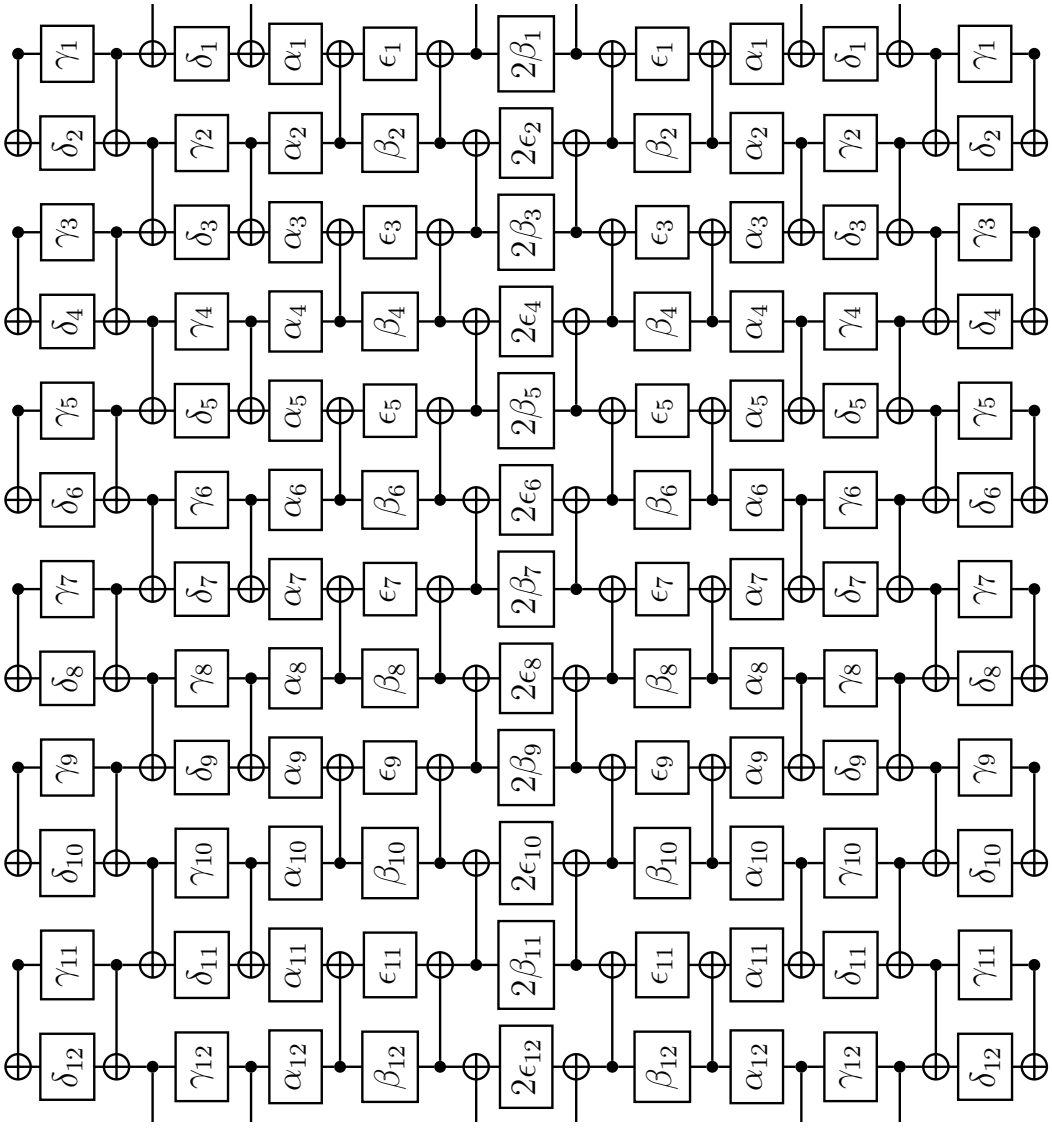

Figure 4.4: One step of imaginary time evolution for the Hamiltonian of Eq. (4.7) and the ansatz of Eq. (4.11). All boxes represent an RY(θ) gate with the angle θ given in the box. The circuit is for a closed loop of 12 qubits, so CNOT gates emerging from the top of the diagram are continued at the bottom. Multiple steps of this circuit ran on a periodic ring of 12 qubits on IBM_BRISBANE.

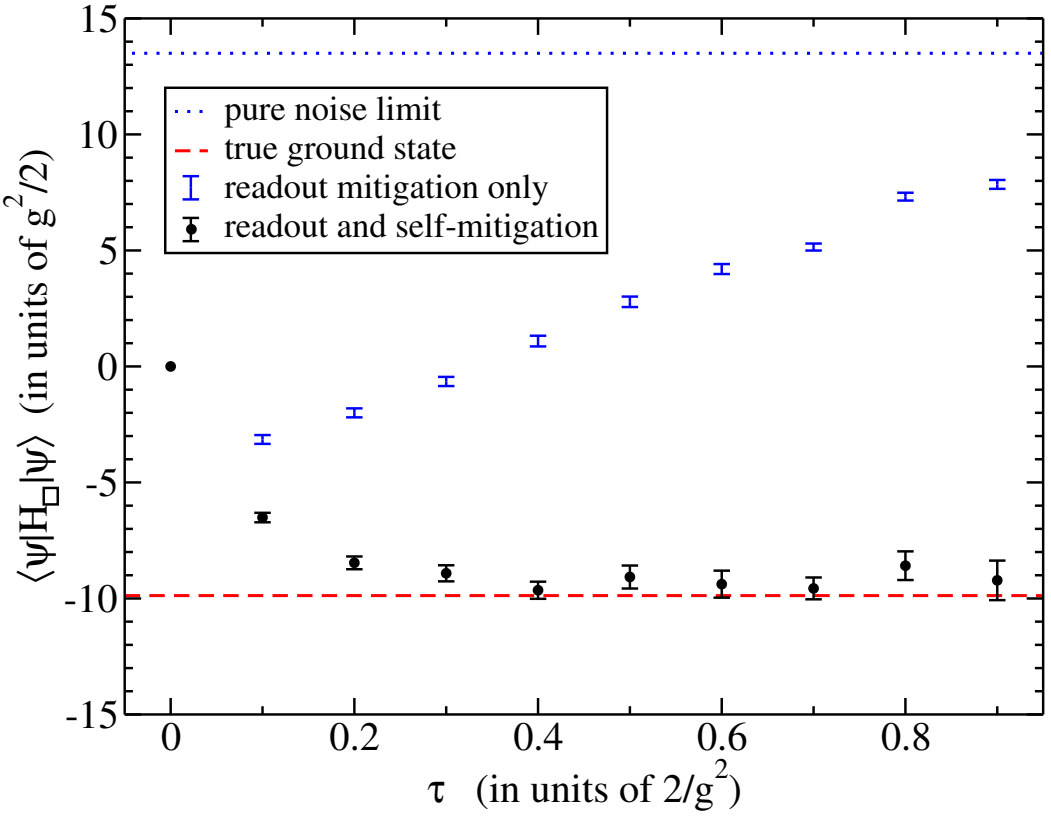

Figure 4.5: Imaginary time evolution of SU(2) gauge theory on a periodic 12-plaquette ladder. The Hamiltonian is Eq. (4.7) with gauge coupling $g = 1$. The true ground state is obtained successfully because of the use of self-mitigation. The code ran on 12 qubits of IBM_BRISBANE. Numerical values from this graph are provided in Table C.1.

forward and half backward.

Details of the self-mitigation method can be found in Refs. [15, 9]. Other uses and extensions of this approach to mitigation can be found in Refs. [51, 52, 54, 148, 99, 100, 101, 102, 103, 137, 149, 150, 151, 152, 153, 154, 155, 139].

In the quantum computation of Fig. 4.5, each quantum circuit used between 40 and 50 randomized compilings with 1000 shots per compiling, and error bars represent 95% confidence intervals. The time step is $\Delta\tau = 0.1$. Without self-mitigation, only the first step moves toward the true result and then all subsequent steps move in the wrong direction, heading toward pure noise. With self-mitigation, early time steps move toward the true result and later time steps remain there, exactly as they should when hardware errors are mitigated successfully. Code that ran on IBM_BRISBANE is publicly available [158]. Each time step used about 100 seconds of time on the quantum hardware for the combined running of the physics and self-mitigation circuits with all randomized compilings.

Given this achievement for the square-plaquette Hamiltonian, can we use a quantum computer for the triamond Hamiltonian? There is no obstacle in principle, but the larger plaquettes mean the ansatz of Eq. (4.11) is insufficient. Inclusion of terms having three or more qubits is required, and explorations of this challenge are underway [159]. On IBM's heavy-hex architecture this leads to many swap gates because of the limited connectivity, but the computation would be more manageable on other qubit architectures. Overall, the implementation of larger plaquettes serves as a reminder of the added cost arising from three-dimensional physics.

4.5 Real-time evolution

Consider the lowest energy state in the diagonal torelon sector of SU(2) gauge theory from Fig. 4.3. Because it is an energy eigenstate, its magnitude will remain unchanged during time evolution. The dominant part of that state is simply the bare six-link torelon averaged over the 12 possible lattice locations,

$$\begin{aligned} |J_0\rangle \;\; = \;\; & \frac{1}{\sqrt{12}}\Big(|110000000000\rangle + |011000000000\rangle \\ & + |001100000000\rangle + \ldots + |100000000001\rangle \Big), \end{aligned} \tag{4.20}$$

which represents a bare torelon at rest. Evolution of $|J_0\rangle$ through real time will show that it is a superposition of several eigenstates. The dominant eigenstates correspond to the separation of the original diagonal torelon (six gauge links) into one horizontal and one vertical torelon

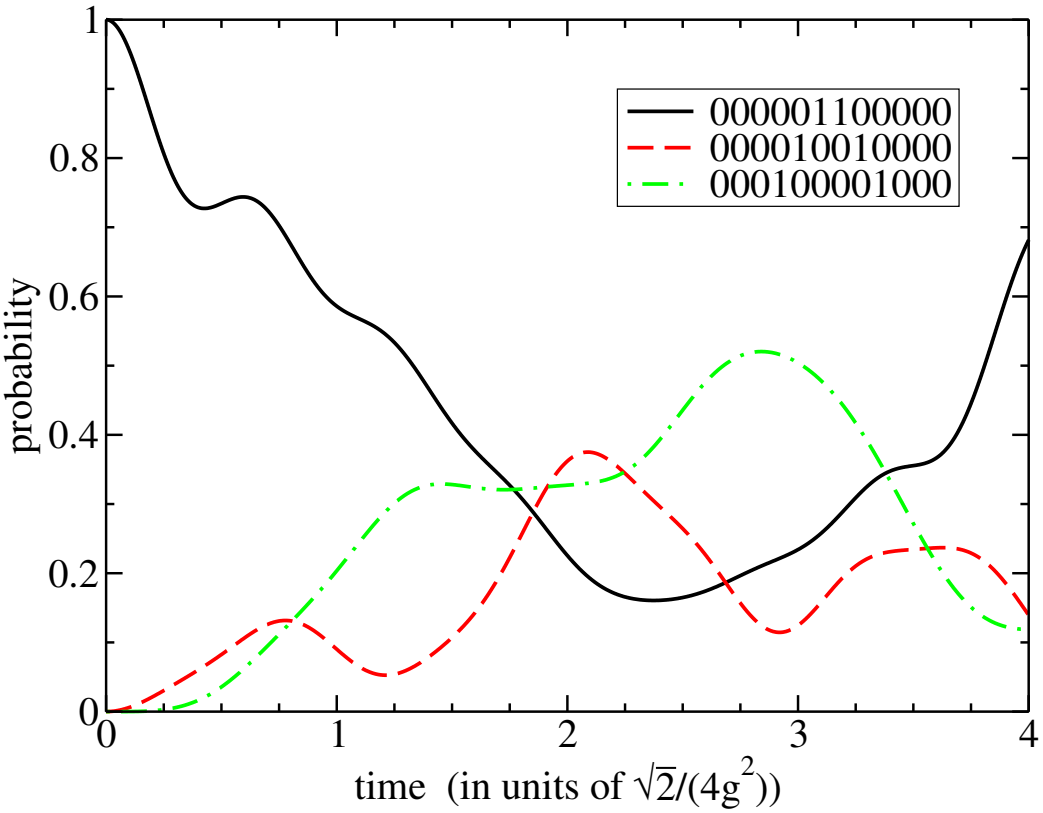

Figure 4.6: Real-time evolution of SU(2) gauge theory on a triamond lattice of three unit cells (12 qubits) and gauge coupling $g = 1.3$. The initial state is a bare diagonal torelon at rest. Time evolution shows the probabilities of separation into two separate torelons, one horizontal and one vertical. Numerical values from this graph are provided in Table B.4.

(four gauge links each). The dynamics can be visualized from Fig. 4.2(d) and numerical results are given in Fig. 4.6. The calculation was done by using the exact eigenvalues and eigenvectors determined in Sec. 4.3. Note that all data in Fig. 4.6 are translation invariant even through the legend shows only one term for brevity.

According to Fig. 4.6, whether measurement of the qubit register is more likely to reveal a diagonal torelon or a separated pair of torelons varies with time, as expected. At time zero, only the diagonal torelon is present. At a slightly later time, the closely separated pair becomes nonzero. Shortly after that, the further separated pair becomes more probable. This matches the classical intuition of two decay products emanating from the original single object.

Consider now the possibility of shrinking the lattice of Fig. 4.2 from its length of three unit cells down to a length of 2.75 unit cells. Specifically, keep the first 11 square paths of Fig. 4.2(b) and erase the 12th one. The periodic boundary condition on the flattened map now represents a twisted boundary condition for the triamond lattice. For example,

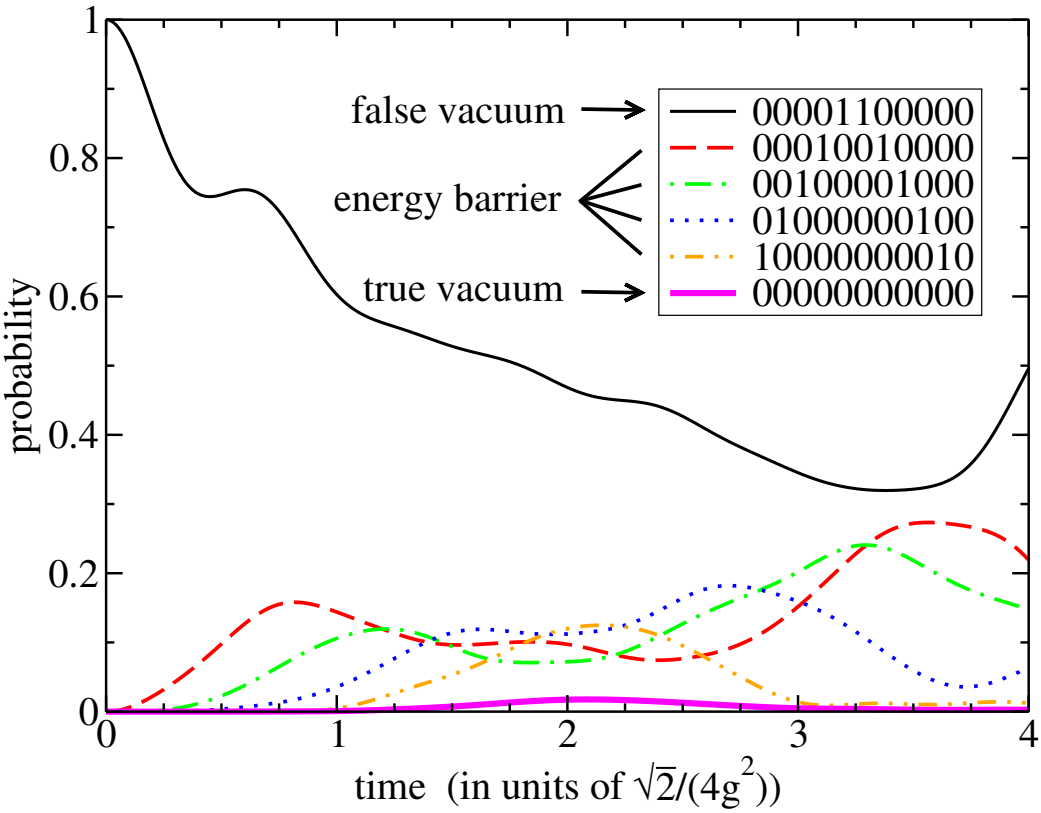

Figure 4.7: False vacuum decay on a triamond lattice. The lattice has 2.75 unit cells (11 qubits) and an SU(2) gauge coupling $g = 1.3$. The initial state is a bare diagonal torelon at rest. Real-time evolution shows the probabilities of separation into two separate torelons, and it also shows the probability of decay into the true vacuum state with no torelons remaining. Numerical values from this graph are provided in Table B.5.

a horizontal torelon that travels completely around the long $\hat{j}$ direction of the lattice will return to its original position as a vertical torelon rather than remaining horizontal.

This 11-qubit triamond lattice is an ideal setup for studying false vacuum decay. The initial state is once again $|J_0\rangle$ of Eq. (4.20) but with 11 terms instead of 12. Real-time evolution will once again produce a probability for the original diagonal torelon to separate into a pair of torelons. That pair of torelons will move further apart until they meet again after having traversed the entire $\hat{j}$ direction. The new ingredient is that they can now annihilate each other because they are both horizontal or both vertical due to the twisted boundary condition. A direct calculation from exact eigenvalues and eigenvectors confirms these expectations as seen in Fig. 4.7. Each entry in the legend of Fig. 4.7 shows only one term for brevity, but all states are fully translation invariant.

The initial state of one diagonal torelon with zero momentum is our false vacuum. It would be completely stable except for the lattice's twisted boundary condition. The true

vacuum is the state containing no torelons at all. To make the transition from the false vacuum to the true vacuum, the original torelon needs to separate into a pair (which is a higher energy state) and the two parts must traverse the entire lattice by travelling in opposite directions. The growing distance between the two parts is clear from the ordering of the curves in the lower left corner of Fig. 4.7. The significant energy barrier between the false vacuum and the true vacuum results in a transition probability of about 2% according to Fig. 4.7.

4.6 Summary and outlook

A gauge invariant string that winds all the way around a periodic lattice boundary is called a torelon. Torelons are prominent objects on small lattices. They can travel across the lattice and collide with each other due to the non-Abelian gauge interactions. Such real-time physics is not available from traditional Euclidean lattice computations but will become readily accessible on quantum computers by using Hamiltonian methods.

A lattice of three spatial dimensions with periodic boundary conditions has 2^3 orthogonal sectors, corresponding to the presence or absence of a torelon in each Cartesian direction. Each of these independent sectors has its own stable ground state. Applying a $\pi/2$ spatial twist at one lattice boundary is sufficient to transform a formerly stable ground state into a false vacuum that is separated from the true vacuum by an energy barrier.

The triamond lattice is an especially efficient lattice for three spatial dimensions. Note, for example, that the triamond lattice properly maintains the $\hat{i}$, $\hat{j}$ and $\hat{k}$ torelons even though the lattice can be mapped onto the periodic ladder of Fig. 4.2(b). In this work, we have used a small triamond lattice to calculate the spectrum of torelon states and false vacuum decay. Also, state preparation was implemented on the quantum computer IBM_BRISBANE for a simplified Hamiltonian through quantum imaginary time evolution.

The three-dimensional properties of a triamond lattice are manifest in its large plaquettes, leading to a Hamiltonian with several qubits per term that challenges the abilities of present-day quantum hardware. The successful quantum computation of one triamond unit cell in Ref. [9] and the 12-qubit quantum computation in Fig. 4.5 of the present work represent two steps toward this goal.

Additional studies can focus on relaxing the gauge field truncation and increasing the lattice size to ultimately compare direct observation of false vacuum decay on a quantum computer to theoretical predictions [5, 114, 36, 115, 29, 116]. There is also a vast range of other time-dependent observables, such as particle scattering in real time, that will become accessible through this direct quantum computing approach.

Chapter 5

Conclusion and Future Work

5.1 Conclusion

The triamond lattice provides an efficient framework for studying three-dimensional non-Abelian gauge theories on quantum computers. By reducing the number of gauge links per site from six to three while maintaining strong isotropy, it resolves the qubit overhead problem that plagues cubic lattices. This geometric efficiency enables practical simulations of genuine three-dimensional phenomena that were previously inaccessible.

Our work demonstrates several significant advances in quantum simulation of lattice gauge theories. The first paper established the triamond lattice as a viable platform, showing successful ground state preparation using quantum imaginary time evolution (QITE) with self-mitigation techniques on IBM quantum hardware. The second paper leveraged this foundation to study dynamic processes, specifically torelon collisions and false vacuum decay - phenomena that can be viewed as analogues of hadron interactions in real-world QCD.

The self-mitigation technique proved crucial for extracting meaningful physical results from noisy quantum hardware. By rescaling expectation values using carefully constructed mitigation circuits, we overcame dominant systematic errors and achieved results that classical verification confirmed as physically accurate. This error mitigation approach enabled the successful 12-qubit QITE computation on IBM Brisbane, representing one of the largest quantum simulations of non-Abelian gauge theories to date.

To elucidate the error mitigation technique, consider the Bloch sphere representation of a qubit. The ideal time evolution operator e^{-iHt} would evolve the quantum state from its initial position to a final state determined by the Hamiltonian. In practice, we implement this evolution via Trotterization, decomposing the Hamiltonian as $H = \sum_i H_i$ and applying the symmetric sequence $e^{-iH_1\Delta t/2}e^{-iH_2\Delta t/2}\dots e^{-iH_n\Delta t/2}\dots e^{-iH_2\Delta t/2}e^{-iH_1\Delta t/2}$ for each time step Δt.

The mitigation circuit performs forward evolution for half the total time followed by backward evolution: $e^{-iH_1\Delta t/2}\dots e^{-iH_n\Delta t/2}\dots e^{+iH_2\Delta t/2}e^{+iH_1\Delta t/2}$. Ideally, this sequence would return the state to its original position. However, hardware noise and imperfections cause displacement from this ideal trajectory. By measuring this displacement, we quantify the error magnitude and rescale results from the physical circuit accordingly. Circuit-specific displacement characterization enables extraction of meaningful physical results from noisy data.

The integration of this mitigation technique with the triamond lattice framework and quantum imaginary time evolution (QITE) method enabled several key achievements:

- Implementation of three-dimensional lattice gauge theory simulations on quantum hardware
- Development of efficient quantum circuits leveraging triamond symmetries
- Demonstration of real-time evolution for false vacuum decay processes
- Successful preparation of complex gauge theory configurations
- Advancement of error mitigation techniques for noisy intermediate-scale quantum devices

These accomplishments represent initial steps toward practical quantum simulation of high-energy physics phenomena in three-dimensional space. While substantial challenges remain, our work demonstrates that meaningful three-dimensional gauge theory simulations are within reach of current quantum hardware when combined with appropriate lattice formulations and error mitigation strategies.

5.2 Future Directions

Several promising directions emerge for extending this research program:

Theory Extensions

- **Inclusion of Fermions:** Adding matter fields represents a crucial step toward realistic QCD simulations. Unlike gauge links that belong to the infinite-dimensional SU(N) group and require truncation schemes (or other schemes such as subgroup methods or Fibonacci patterns), fermions can be encoded with relatively few qubits per site. Initial

implementations could begin with Wilson fermions on the triamond lattice, with subsequent advancements to staggered fermions once the technical challenges of coupling fermions to the triamond geometry are resolved [70, 71].

- **Relaxed Truncation:** In our studies, we restricted ourselves to the simplest nontrivial case in SU(2) gauge theories by truncating the gauge link representations to $j \in \{0, \frac{1}{2}\}$. However, there is no guarantee that this minimal truncation captures the full physics of the theory. Moving beyond this truncation to include higher representations (e.g., $j = 1, \frac{3}{2}, \dots$) would improve the approximation and allow access to weaker coupling regimes. However, such an extension would require additional qubits per gauge link. Alternative digitization schemes, such as subgroup approximations or Fibonacci patterns, could also be explored for more efficient encoding of the infinite-dimensional gauge link space [72, 92].

- **SU(3) Gauge Group:** While SU(2) gauge theories have historically provided valuable insights into non-perturbative QCD phenomena, SU(3) represents the true gauge group of quantum chromodynamics. Extending to SU(3) is therefore essential for realistic QCD simulations. However, this extension introduces significant complexity: the fundamental representation of SU(3) involves three colors (r, g, b) and their anti-colors, leading to more complicated color singlet combinations. For instance, the tensor product decomposition $8 \otimes 8 \otimes 8 = (27 \oplus 10 \oplus \bar{10} \oplus 8 \oplus 8 \oplus 1) \otimes 8$ reveals two pathways to color singlet states at vertices, one from each of the $8 \otimes 8$ terms. While the triamond lattice may not completely eliminate qubit overhead for SU(3), it still offers substantial advantages over cubic lattices due to its reduced connectivity, making it a fruitful approach for studying genuine QCD dynamics [47, 137, 34, 35].

Computational Advances

This section outlines the transition from current error-mitigated quantum computing to future fault-tolerant architectures, which is essential for scaling quantum simulations of lattice gauge theories.

- **Fault-Tolerant Quantum Computing:** While error mitigation techniques have enabled meaningful quantum computations on current noisy hardware, they come with significant overhead. Each circuit submitted to the quantum computer requires an additional mitigation circuit to characterize the noise profile, followed by substantial post-processing to derive rescaling factors and extract actual physical results. Although

effective, this approach is not scalable for future quantum computing. The next generation of quantum computers must be noise-aware and capable of real-time error correction during gate operations and idle periods. Fault-tolerant quantum computation represents this paradigm shift, where instead of working with physical qubits directly, we employ logical qubits - quantum information encoded across multiple physical qubits and protected through continuous parity checks. Different quantum computing platforms are pursuing various strategies for fault tolerance, with surface codes and LDPC (Low-Density Parity-Check) codes emerging as leading approaches. Both belong to the broader family of stabilizer codes, which use symplectic geometry and Pauli measurements to detect and correct errors without disturbing the encoded quantum information [165, 168].

Surface Code Implementation

The surface code represents one of the most promising approaches for practical fault-tolerant quantum computing due to its high error threshold and compatibility with $2D$ architectures. The following outlines the key characteristics that make the surface code particularly suitable for large-scale quantum simulations:

- **Logical Qubits and Stabilizer Codes:** The foundation of fault-tolerant quantum computing lies in the concept of logical qubits - quantum information encoded across multiple physical qubits and protected by quantum error correction codes. Stabilizer codes form a particularly important class of these codes, where the logical subspace is defined as the simultaneous $+1$ eigenspace of a set of commuting operators called stabilizers. These stabilizers are typically products of Pauli operators on multiple physical qubits, and their measurement (without disturbing the encoded information) allows for error detection and correction [166].

- **From Toric Codes to Rotated Surface Codes:** The toric code, one of the most studied topological quantum error correction codes, arranges physical qubits on a toroidal lattice with stabilizers defined on plaquettes and vertices. While theoretically elegant, the toric code requires a toroidal geometry that is challenging to implement physically. The rotated surface code addresses this limitation by working on a planar square lattice with non-periodic boundary conditions, making it more suitable for current quantum hardware architectures. This code achieves the same distance as the toric code but with approximately half the number of physical qubits per logical qubit, providing significant resource savings [167].

- **Rotated Surface Code Structure:** In the rotated surface code, physical qubits are arranged on the vertices of a square lattice, with two types of stabilizers: Z-type stabilizers (products of Pauli-Z operators around plaquettes) and X-type stabilizers (products of Pauli-X operators around vertices). The logical qubit as illustrated in Fig. 5.1, is defined by non-local operators that span the entire lattice - specifically, a string of Z operators along one boundary defines the logical Z operator ($\bar{Z}$), while a string of X operators along the perpendicular boundary defines the logical X operator ($\bar{X}$). These logical operators commute with all stabilizers but anti-commute with each other, exactly mimicking the behavior of physical Pauli operators on a single qubit [165].

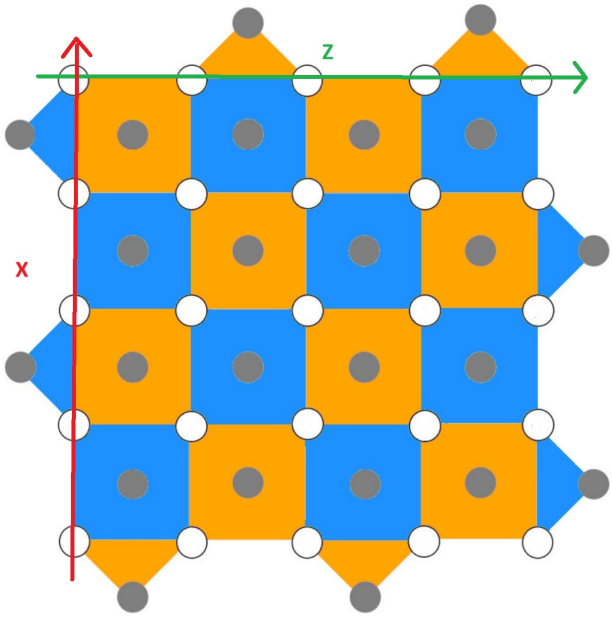

Figure 5.1: Schematic of a distance-5 rotated surface code. Physical data qubits are represented by white circles, while syndrome measurement qubits are shown as grey circles. Z-type stabilizers (blue squares) and X-type stabilizers (yellow squares) are measured periodically to detect errors. The logical $\bar{Z}$ operator consists of a horizontal chain of Z operators acting on data qubits along the top boundary, while the logical $\bar{X}$ operator comprises a vertical chain of X operators acting on data qubits along the left boundary. These logical operators define the encoded qubit and commute with all stabilizers. Repeated rounds of parity check measurements enable continuous error detection and correction while preserving the encoded quantum information.

- **Error Protection through Parity Checks:** The surface code protects quantum information through repeated rounds of parity check measurements. Each round involves measuring all stabilizers, creating a syndrome that reveals information about errors without collapsing the logical state. By performing multiple rounds and tracking

how the syndrome changes over time, we can distinguish between actual errors and measurement errors, enabling reliable error correction. The code distance d determines how many errors can be corrected, with a distance-d code capable of correcting any $\lfloor (d-1)/2 \rfloor$ errors [165].

- **Transversal Gates and Logical Operations:** A key advantage of stabilizer codes is the existence of transversal gates - operations that can be implemented by applying the same single-qubit gate to each physical qubit in the code block. For the surface code, the Clifford gates (Hadamard, Phase, and CNOT) can be implemented transversally. CNOT gates between logical qubits can be efficiently realized through lattice surgery techniques, which involve temporarily merging and splitting surface code patches to create entanglement between logical qubits. This technique is essential for building complex quantum circuits while maintaining fault tolerance, as it allows for controlled operations between encoded qubits without compromising error protection [169].

Integration with Triamond Lattice Simulations

With these fault-tolerant techniques, we can envision future simulations of the triamond lattice where logical qubits replace the physical qubits in our current implementation, while maintaining the same $j \in \{0, \frac{1}{2}\}$ truncation for the gauge links. In this fault-tolerant paradigm, error mitigation techniques become unnecessary as quantum error correction actively protects the logical information throughout the computation. The surface code's continuous parity check measurements monitor and correct errors in real-time, ensuring the logical state remains coherent and accurate. This approach would enable extended simulations of gauge theories, including real-time evolution of hadron collisions and other dynamic processes currently beyond the capabilities of noisy intermediate-scale quantum devices. For further details on lattice surgery, stabilizer codes, and the implementation of physical circuits at the logical level, see Appendix D.

The combination of fault-tolerant quantum computation with the triamond lattice framework opens exciting possibilities for future research. Once logical qubits with sufficiently low error rates become available, we could simulate hadron-hadron collisions from first principles, providing unprecedented insights into strong interaction dynamics. The triamond lattice's efficiency in three dimensions makes it particularly well-suited for such complex scattering processes, as it minimizes the qubit overhead while maintaining the essential spatial structure needed for realistic collision simulations [16].

The combination of the triamond lattice for efficient gauge theory simulation with surface codes for fault tolerance represents a powerful approach for future quantum simulations

of high-energy physics. As quantum hardware matures, this integrated framework will enable the simulation of complex phenomena like hadron-hadron collisions with unprecedented accuracy and scale.

The path toward full-scale quantum simulation of QCD remains challenging, but the triamond lattice approach provides a systematic framework for incremental progress. Each extension - whether incorporating matter fields, moving to SU(3), or relaxing truncations - brings us closer to the ultimate goal of simulating real-world strong interaction physics on quantum computers. The techniques developed here for error mitigation and efficient lattice encoding will serve as valuable tools in this ongoing effort.

As quantum hardware continues to improve in fidelity and scale, the combination of efficient lattice formulations like the triamond and fault-tolerant quantum computation positions the field to tackle increasingly complex gauge theory problems, potentially yielding new insights into non-perturbative quantum field theory that are inaccessible to classical computation [6, 7].

Appendix A

Mathematical Details and Methods

The content in this appendix is adopted from [9].

A.1 Tomography for the QITE Algorithm

The QITE procedure [98] needs optimal values for the coefficients a_{jk} in the operator $\hat{A}$. For notational convenience the subscripts can be combined into a single subscript, so $a_{jk} \equiv a_J$ with J running from 1 to 6. The a_J values can be obtained by minimizing Trotter errors, which means minimizing the difference between

$$|\Delta_0\rangle \equiv \left(\frac{e^{-i\tau\hat{A}} - 1}{\tau}\right)|\psi\rangle \tag{A.1}$$

and

$$|\Delta\rangle \equiv -i\hat{A}\,|\psi\rangle\ . \tag{A.2}$$

It is more convenient to work with a scalar function rather than states, so we actually minimize

$$\langle\Delta_0 - \Delta|\Delta_0 - \Delta\rangle \equiv \langle\Delta_0|\Delta_0\rangle + a_J b_J + a_J S_{JK} a_K\,, \tag{A.3}$$

where the 6-component vector b and the 6×6 matrix S are real-valued. Minimization results in

$$a = -(S + S^T)^{-1} b\,, \tag{A.4}$$

with

$$b_1 = -i \langle\psi| \left[\hat{H}, \hat{Y}_0\right] |\psi\rangle , \tag{A.5}$$

$$b_2 = -i \langle\psi| \left[\hat{H}, \hat{X}_1\hat{Y}_0\right] |\psi\rangle , \tag{A.6}$$

$$b_3 = -i \langle\psi| \left[\hat{H}, \hat{Z}_1\hat{Y}_0\right] |\psi\rangle , \tag{A.7}$$

$$b_4 = -i \langle\psi| \left[\hat{H}, \hat{Y}_1\right] |\psi\rangle , \tag{A.8}$$

$$b_5 = -i \langle\psi| \left[\hat{H}, \hat{Y}_1\hat{X}_0\right] |\psi\rangle , \tag{A.9}$$

$$b_6 = -i \langle\psi| \left[\hat{H}, \hat{Y}_1\hat{Z}_0\right] |\psi\rangle , \tag{A.10}$$

and the only nonzero entries in $S + S^T$ are

$$(S+S^T)_{11} = (S+S^T)_{22} = 2, \tag{A.11}$$

$$(S+S^T)_{33} = (S+S^T)_{44} = 2, \tag{A.12}$$

$$(S+S^T)_{55} = (S+S^T)_{66} = 2, \tag{A.13}$$

$$(S+S^T)_{12} = (S+S^T)_{21} = 2 \langle\psi| \hat{X}_1 |\psi\rangle , \tag{A.14}$$

$$(S+S^T)_{13} = (S+S^T)_{31} = 2 \langle\psi| \hat{Z}_1 |\psi\rangle , \tag{A.15}$$

$$(S+S^T)_{14} = (S+S^T)_{41} = 2 \langle\psi| \hat{Y}_1\hat{Y}_0 |\psi\rangle , \tag{A.16}$$

$$(S+S^T)_{25} = (S+S^T)_{52} = 2 \langle\psi| \hat{Z}_1\hat{Z}_0 |\psi\rangle , \tag{A.17}$$

$$(S+S^T)_{26} = (S+S^T)_{62} = -2 \langle\psi| \hat{Z}_1\hat{X}_0 |\psi\rangle , \tag{A.18}$$

$$(S+S^T)_{35} = (S+S^T)_{53} = -2 \langle\psi| \hat{X}_1\hat{Z}_0 |\psi\rangle , \tag{A.19}$$

$$(S+S^T)_{36} = (S+S^T)_{63} = 2 \langle\psi| \hat{X}_1\hat{X}_0 |\psi\rangle , \tag{A.20}$$

$$(S+S^T)_{45} = (S+S^T)_{54} = 2 \langle\psi| \hat{X}_0 |\psi\rangle , \tag{A.21}$$

$$(S+S^T)_{46} = (S+S^T)_{64} = 2 \langle\psi| \hat{Z}_0 |\psi\rangle . \tag{A.22}$$

The numerical computation of b, $S + S^T$ and r'/r requires nine expectation values. Three of them can be obtained by preparing the state $|\psi\rangle$ in a quantum computer and measuring each qubit, which gives

$$\langle\psi| \hat{Z}_0 |\psi\rangle = 1 - 2P_0, \tag{A.23}$$

$$\langle\psi| \hat{Z}_1 |\psi\rangle = 1 - 2P_1, \tag{A.24}$$

$$\langle\psi| \hat{Z}_1 Z_0 |\psi\rangle = 1 - 2P_{1\oplus 0}, \tag{A.25}$$

where P_j is the probability that qubit j is 1, and $P_{1\oplus 0}$ is the probability that both qubits are 1.

Three other expectation values are obtained by preparing the state $|\psi'\rangle = RY_1(-\frac{\pi}{2})RY_0(-\frac{\pi}{2})\,|\psi\rangle$ in a quantum computer and measuring each qubit, which gives

$$\langle\psi|\,\hat{X}_0\,|\psi\rangle = 1 - 2P'_0, \tag{A.26}$$

$$\langle\psi|\,\hat{X}_1\,|\psi\rangle = 1 - 2P'_1, \tag{A.27}$$

$$\langle\psi|\,\hat{X}_1X_0\,|\psi\rangle = 1 - 2P'_{1\oplus0}. \tag{A.28}$$

The remaining three expectation values are obtained similarly: Preparing $|\psi''\rangle = RX_1(\frac{\pi}{2})RX_0(\frac{\pi}{2})\,|\psi\rangle$ gives

$$\langle\psi|\,\hat{Y}_1Y_0\,|\psi\rangle = 1 - 2P''_{1\oplus0}. \tag{A.29}$$

Preparing $|\psi'''\rangle = RY_0(-\frac{\pi}{2})\,|\psi\rangle$ gives

$$\langle\psi|\,\hat{Z}_1X_0\,|\psi\rangle = 1 - 2P'''_{1\oplus0}. \tag{A.30}$$

Preparing $|\psi''''\rangle = RY_1(-\frac{\pi}{2})\,|\psi\rangle$ gives

$$\langle\psi|\,\hat{X}_1Z_0\,|\psi\rangle = 1 - 2P''''_{1\oplus0}. \tag{A.31}$$

It should be noted that the QITE procedure does not require $S + S^T$ to be an invertible matrix. For all practical purposes, $(S + S^T)^{-1}$ can be interpreted as the Moore-Penrose pseudo-inverse [111, 112] and this is what we use for our calculations.

A.2 Randomized Compiling for CNOT Gates

The conversion of CNOT errors into incoherent noise is accomplished by randomizing the input to each CNOT gate in a circuit [43, 15]. Two random Pauli gates are applied immediately before the CNOT gate, one to the control qubit and the other to the target qubit. Specifically, each gate is chosen randomly from the set $\{I, X, Y, Z\}$. Immediately after the CNOT gate, two Pauli gates are applied to ensure that the combined effect of Pauli gates would not change the circuit's output on error-free hardware.

A.3 Deriving the Triamond SU(2) Hamiltonian

This section outlines the derivation that begins with gauge links on a triamond lattice and arrives at the Hamiltonian for SU(2) gauge theory. The coefficients are defined by their need to agree with continuum SU(2) gauge theory, so our first step is to expand the sum over

plaquettes in powers of the lattice spacing.

Consider a general gauge link, $U(\vec{w}+\vec{t},\hat{s})$, where $\vec{w}$ is a white site on the lattice. The lattice spacing a enters through the vectors $\vec{t}$ and $\hat{s}$. The expansion for a typical gauge link takes the form:

$$\begin{aligned} U(\vec{w}+a\hat{g},\frac{\hat{k}+\hat{i}}{\sqrt{2}}) &= I+\frac{ia}{2}\left(A_x(\vec{w})+A_z(\vec{w})\right) \\ &\quad +\frac{ia^2}{4}(\partial_x-\partial_y)\left(A_x(\vec{w})+A_z(\vec{w})\right) \\ &\quad -\frac{a^2}{8}\left(A_x(\vec{w})+A_z(\vec{w})\right)^2 \\ &\quad +O(a^3)\,. \end{aligned} \tag{A.32}$$

Performing such expansions for all links in a plaquette provides an expression that can be summed over the lattice. The final result for the sum of all 6 plaquettes is

$$\sum_{k=1}^{6}\mathcal{P}_k = 12-8a^4\mathrm{Tr}\left(F_{xy}^2+F_{yz}^2+F_{zx}^2\right)+O(a^5)\,, \tag{A.33}$$

where the field strength tensor is $F_{\mu\nu}=\partial_\mu A_\nu-\partial_\nu A_\mu+i[A_\mu,A_\nu]$.

The continuum expression for the magnetic Hamiltonian can be converted from an integral to a sum:

$$H_B=\frac{V}{g^2}\sum_{\vec{w}=\text{white}}\mathrm{Tr}\big(F_{xy}^2(\vec{w})+F_{yz}^2(\vec{w})+F_{zx}^2(\vec{w})\big)+O(a)\,, \tag{A.34}$$

where V is the volume per white site. There are two white sites in each unit cell, and the volume of a unit cell is $(2\sqrt{2}a)^3$, so $V=16\sqrt{2}a^3$. Therefore the magnetic Hamiltonian becomes

$$H_B=\frac{2\sqrt{2}}{g^2a}\sum_{\vec{w}=\text{white}}\left(12-\sum_{k=1}^{6}\mathcal{P}_k(\vec{w})\right)+O(a)\,. \tag{A.35}$$

The constant term has no effect on dynamics so it can be dropped.

Converting the electric Hamiltonian from the continuum to the triamond lattice is straightforward:

$$\begin{aligned} H_E &= \frac{Vg^2}{6}\sum_{n=\text{links}}\mathrm{Tr}\left(E_x^2(n)+E_y^2(n)+E_z^2(n)\right)+O(a) \\ &= \frac{8\sqrt{2}a^3g^2}{3}\sum_{n=\text{links}}\mathrm{Tr}\left(E_x^2(n)+E_y^2(n)+E_z^2(n)\right)+O(a) \end{aligned} \tag{A.36}$$

A.4 Hamiltonian and Circuits for Triamond Unit Cell

For the triamond unit cell with periodic boundary conditions and truncation to $j \in \{0, \frac{1}{2}\}$, the Hamiltonian can be written in terms of Pauli operators as:

The Hamiltonian is the sum of an electric part and three magnetic parts,

$$H = H_E + H_{\bar{r}\bar{c}} + H_{\bar{g}\bar{m}} + H_{\bar{b}\bar{y}} \,. \tag{A.37}$$

The electric part is a sum of contributions from all gauge links:

$$H_E = \frac{2\sqrt{2}g^2}{a} \sum_{k=1}^{12} \frac{1 - Z_k}{2} \,. \tag{A.38}$$

The magnetic terms correspond respectively to application of the non-red non-cyan plaquette,

$$\begin{aligned} H_{\bar{r}\bar{c}} \;=\; & -\frac{\sqrt{2}}{4g^2 a} \prod_{k \notin \{r,c\}} X_k \\ & -\frac{3\sqrt{2}}{4g^4 a} \left(\prod_{k \in \{r,c\}} \frac{1 + Z_k}{2} \right) \prod_{k \notin \{r,c\}} X_k \\ & +\frac{3\sqrt{2}}{16g^4 a} \left(\prod_{k \in \{r,c\}} \frac{1 - Z_k}{2} \right) \prod_{k \notin \{r,c\}} X_k \,, \end{aligned} \tag{A.39}$$

application of the non-green non-magenta plaquette,

$$\begin{aligned} H_{\bar{g}\bar{m}} \;=\; & -\frac{\sqrt{2}}{4g^2 a} \prod_{k \notin \{g,m\}} X_k \\ & -\frac{3\sqrt{2}}{4g^4 a} \left(\prod_{k \in \{g,m\}} \frac{1 + Z_k}{2} \right) \prod_{k \notin \{g,m\}} X_k \\ & +\frac{3\sqrt{2}}{16g^4 a} \left(\prod_{k \in \{g,m\}} \frac{1 - Z_k}{2} \right) \prod_{k \notin \{g,m\}} X_k \,, \end{aligned} \tag{A.40}$$

and application of the non-blue non-yellow plaquette,

$$
\begin{aligned}
H_{\bar{b}\bar{y}} \;=\; & -\frac{\sqrt{2}}{4g^2a}\prod_{k\notin\{b,y\}} X_k \\
& -\frac{3\sqrt{2}}{4g^4a}\left(\prod_{k\in\{b,y\}}\frac{1+Z_k}{2}\right)\prod_{k\notin\{b,y\}} X_k \\
& +\frac{3\sqrt{2}}{16g^4a}\left(\prod_{k\in\{b,y\}}\frac{1-Z_k}{2}\right)\prod_{k\notin\{b,y\}} X_k\,. \qquad \text{(A.41)}
\end{aligned}
$$

Appendix B

Energy Eigenvalues and Eigenvectors

The content in this appendix is adopted from [10].

The basis states of our computations can be represented by listing the SU(2) eigenvalues of the 12 numbered gauge links of Fig. 4.2(b) in order from left to right. The bare vacuum state is

$$|A\rangle = |000000000000\rangle \tag{B.1}$$

and examples of single plaquette states include

$$\begin{aligned} |B_1\rangle &= |101000000000\rangle\,, && \text{(B.2)}\\ |B_2\rangle &= |010100000000\rangle\,, && \text{(B.3)}\\ |B_3\rangle &= |001010000000\rangle\,, && \text{(B.4)}\\ &\vdots \\ |B_{12}\rangle &= |010000000001\rangle\,, && \text{(B.5)} \end{aligned}$$

and

$$\begin{aligned} |C_1\rangle &= |111100000000\rangle\,, && \text{(B.6)}\\ |C_2\rangle &= |011110000000\rangle\,, && \text{(B.7)}\\ |C_3\rangle &= |001111000000\rangle\,, && \text{(B.8)}\\ &\vdots \\ |C_{12}\rangle &= |111000000001\rangle\,. && \text{(B.9)} \end{aligned}$$

Notice that the subscript represents screw-translation and corresponds to a symmetry of the

triamond lattice. Other significant states are

$$|D_1\rangle = |100010000000\rangle\,, \tag{B.10}$$

$$|E_1\rangle = |100000100000\rangle\,, \tag{B.11}$$

together with their screw-translations. States of definite screw-momentum can be obtained from a Fourier transform,

$$|B_\theta\rangle = \frac{1}{\sqrt{12}}\sum_{j=1}^{12} e^{-ij\theta}\,|B_j\rangle\,, \tag{B.12}$$

$$|C_\theta\rangle = \frac{1}{\sqrt{12}}\sum_{j=1}^{12} e^{-ij\theta}\,|C_j\rangle\,, \tag{B.13}$$

$$|D_\theta\rangle = \frac{1}{\sqrt{12}}\sum_{j=1}^{12} e^{-ij\theta}\,|D_j\rangle \tag{B.14}$$

for $\theta \in \{0, \pm\frac{\pi}{6}, \pm\frac{\pi}{3}, \pm\frac{\pi}{2}, \pm\frac{2\pi}{3}, \pm\frac{5\pi}{6}, \pi\}$ and

$$|E_\theta\rangle = \frac{1}{\sqrt{6}}\sum_{j=1}^{6} e^{-ij\theta}\,|E_j\rangle \tag{B.15}$$

for $\theta \in \{0, \pm\frac{\pi}{3}, \pm\frac{2\pi}{3}, \pi\}$. Table B.1 shows the leading contributions to the eigenvectors having the lowest energies in the no-torelon sector.

Basis states in the horizontal torelon sector have six screw-translation locations, such as

$$|F_1\rangle = |010000000000\rangle\,, \tag{B.16}$$

$$|F_2\rangle = |000100000000\rangle\,, \tag{B.17}$$

$$|F_3\rangle = |000001000000\rangle\,, \tag{B.18}$$

$$|F_4\rangle = |000000010000\rangle\,, \tag{B.19}$$

$$|F_5\rangle = |000000000100\rangle\,, \tag{B.20}$$

$$|F_6\rangle = |000000000001\rangle\,, \tag{B.21}$$

Table B.1: The smallest energy eigenvalues in the no-torelon sector with their eigenvectors, for $g = 1.3$. Only the leading contributions to each eigenvector are listed. Entries containing $\pm$ are degenerate pairs. The eigenvalues are displayed graphically in Fig. 4.3.

Value	Vector
7.9907	$0.22\,\|A\rangle - 0.76\,\|B_0\rangle + 0.57\,\|E_0\rangle + \ldots$
7.8551	$0.23\,\|B_\pi\rangle - 0.57\,\|E_\pi\rangle + \ldots$
7.5866	$0.79\,\left\|B_{\pm 2\pi/3}\right\rangle + 0.56\,\left\|E_{\pm 2\pi/3}\right\rangle + \ldots$
7.5673	$0.15\,\left\|B_{\pm \pi/2}\right\rangle + 0.96\,\left\|D_{\pm \pi/2}\right\rangle + \ldots$
7.5224	$0.96\,\left\|B_{\pm \pi/2}\right\rangle - 0.15\,\left\|D_{\pm \pi/2}\right\rangle + \ldots$
7.4997	$0.78\,\left\|B_{\pm \pi/3}\right\rangle - 0.57\,\left\|D_{\pm \pi/3}\right\rangle + \ldots$
6.5693	$0.40\,\left\|B_{\pm 2\pi/3}\right\rangle - 0.70\,\left\|D_{\pm 2\pi/3}\right\rangle - 0.56\,\left\|E_{\pm 2\pi/3}\right\rangle + \ldots$
6.5359	$0.44\,\left\|B_{\pm \pi/3}\right\rangle - 0.69\,\left\|D_{\pm \pi/3}\right\rangle - 0.54\,\left\|E_{\pm \pi/3}\right\rangle + \ldots$
6.5357	$0.70\,\left\|B_{\pm \pi/6}\right\rangle - 0.69\,\left\|D_{\pm \pi/6}\right\rangle + \ldots$
6.5133	$0.70\,\left\|B_{\pm 5\pi/6}\right\rangle - 0.68\,\left\|D_{\pm 5\pi/6}\right\rangle + \ldots$
5.1688	$0.17\,\|A\rangle - 0.35\,\|B_0\rangle - 0.68\,\|D_0\rangle - 0.56\,\|E_0\rangle + \ldots$
5.1084	$0.42\,\|B_\pi\rangle + 0.68\,\|D_\pi\rangle + 0.55\,\|E_\pi\rangle + \ldots$
-0.8795	$0.95\,\|A\rangle + 0.29\,\|B_0\rangle - 0.12\,\|C_0\rangle + 0.05\,\|D_0\rangle + \ldots$

and

$$|G_1\rangle = |111000000000\rangle\,, \tag{B.22}$$

$$|G_2\rangle = |001110000000\rangle\,, \tag{B.23}$$

$$|G_3\rangle = |000011100000\rangle\,, \tag{B.24}$$

$$|G_4\rangle = |000000111000\rangle\,, \tag{B.25}$$

$$|G_5\rangle = |000000001110\rangle\,, \tag{B.26}$$

$$|G_6\rangle = |100000000011\rangle\,. \tag{B.27}$$

Other important basis states in the horizontal torelon sector include

$$|H_1\rangle = \frac{1}{\sqrt{2}}(|110010000000\rangle + |100110000000\rangle), \tag{B.28}$$

$$|I_1\rangle = \frac{1}{\sqrt{2}}(|110000100000\rangle + |100001100000\rangle), \tag{B.29}$$

along with their screw-translations. Table B.2 shows the leading contributions to the eigenvectors having the lowest energies in the horizontal torelon sector.

Basis states in the diagonal torelon sector have 12 screw-translation locations. The lowest

Table B.2: The smallest energy eigenvalues in the horizontal torelon sector with their eigenvectors, for $g = 1.3$. Only the leading contributions to each eigenvector are listed. Entries containing $\pm$ are degenerate pairs. The eigenvalues are displayed graphically in Fig. 4.3.

Value	Vector
7.5222	$0.96\,\lvert G_{\pi}\rangle$
7.4834	$0.94\,\lvert G_{\pm 2\pi/3}\rangle + \ldots$
7.3943	$0.88\,\lvert G_{\pm \pi/3}\rangle - 0.46\,\lvert H_{\pm \pi/3}\rangle$
7.2297	$0.11\,\lvert F_0\rangle - 0.69\,\lvert G_0\rangle + 0.41\,\lvert H_0\rangle + 0.36\,\lvert I_0\rangle + \ldots$
4.7162	$0.96\,\lvert F_{\pi}\rangle + \ldots$
4.1822	$0.97\,\lvert F_{\pm 2\pi/3}\rangle + \ldots$
2.8189	$0.97\,\lvert F_{\pm \pi/3}\rangle + \ldots$
1.8586	$0.95\,\lvert F_0\rangle + \ldots$

energy states are dominated by

$$|J_1\rangle = |110000000000\rangle\,, \tag{B.30}$$

$$|J_2\rangle = |011000000000\rangle\,, \tag{B.31}$$

$$|J_3\rangle = |001100000000\rangle\,, \tag{B.32}$$

$$\vdots$$

$$|J_{12}\rangle = |100000000001\rangle\,, \tag{B.33}$$

but we can also define

$$|K_1\rangle = |100100000000\rangle\,, \tag{B.34}$$

$$|L_1\rangle = |100001000000\rangle\,, \tag{B.35}$$

along with their screw-translations. Table B.3 shows the leading contributions to the eigenvectors having the lowest energies in the diagonal torelon sector.

Evolution through real time can be calculated from the full set of eigenvalues and eigenvectors. For 3 unit cells, results are shown numerically in Table B.4 and graphically in Fig. 4.6. For 2.75 unit cells, results are shown numerically in Table B.5 and graphically in Fig. 4.7.

Table B.3: The smallest energy eigenvalues in the diagonal torelon sector with their eigenvectors, for $g = 1.3$. Only the leading contributions to each eigenvector are listed. Entries containing $\pm$ are degenerate pairs. The eigenvalues are displayed graphically in Fig. 4.3.

Value	Vector
7.8411	$0.58 \left\lvert K_{\pm\pi/2} \right\rangle + 0.80 \left\lvert L_{\pm\pi/2} \right\rangle + \ldots$
7.5380	$0.79 \left\lvert K_{\pm\pi/2} \right\rangle - 0.57 \left\lvert L_{\pm\pi/2} \right\rangle + \ldots$
7.1800	$0.81 \left\lvert K_{\pm2\pi/3} \right\rangle - 0.51 \left\lvert L_{\pm2\pi/3} \right\rangle + \ldots$
7.1496	$0.06 \left\lvert J_{\pm\pi/6} \right\rangle + 0.79 \left\lvert K_{\pm\pi/6} \right\rangle + 0.51 \left\lvert L_{\pm\pi/6} \right\rangle + \ldots$
7.1183	$0.79 \left\lvert K_{\pi} \right\rangle + 0.50 \left\lvert L_{\pi} \right\rangle + \ldots$
6.6515	$0.48 \left\lvert K_{\pm\pi/3} \right\rangle + 0.84 \left\lvert L_{\pm\pi/3} \right\rangle + \ldots$
5.9206	$0.63 \left\lvert J_{\pm5\pi/6} \right\rangle - 0.31 \left\lvert K_{\pm5\pi/6} \right\rangle - 0.67 \left\lvert L_{\pm5\pi/6} \right\rangle + \ldots$
5.8511	$0.97 \left\lvert J_{\pm\pi/2} \right\rangle + \ldots$
5.8075	$0.96 \left\lvert J_{\pm2\pi/3} \right\rangle + \ldots$
5.6195	$0.51 \left\lvert J_0 \right\rangle + 0.37 \left\lvert K_0 \right\rangle + 0.75 \left\lvert L_0 \right\rangle + \ldots$
5.4622	$0.95 \left\lvert J_{\pm\pi/3} \right\rangle + \ldots$
5.3389	$0.92 \left\lvert J_{\pi} \right\rangle + \ldots$
5.3357	$0.72 \left\lvert J_{\pm5\pi/6} \right\rangle + 0.43 \left\lvert K_{\pm5\pi/6} \right\rangle - 0.49 \left\lvert L_{\pm5\pi/6} \right\rangle + \ldots$
4.8470	$0.93 \left\lvert J_{\pm\pi/6} \right\rangle - 0.27 \left\lvert K_{\pm\pi/6} \right\rangle + \ldots$
4.3708	$0.81 \left\lvert J_0 \right\rangle - 0.38 \left\lvert K_0 \right\rangle - 0.35 \left\lvert L_0 \right\rangle + \ldots$

Table B.4: Time evolution of a diagonal torelon at rest on 3 unit cells. Labels J, K and L correspond to Eqs. (B.30-B.35). Results from this table are displayed graphically in Fig. 4.6.

Time	Probability		
	J	K	L
0.25	0.8067	0.0304	0.0028
0.50	0.7343	0.0824	0.0356
0.75	0.7025	0.1309	0.1117
1.00	0.5860	0.0902	0.2035
1.25	0.5334	0.0540	0.3011
1.50	0.4169	0.1070	0.3281
1.75	0.3271	0.2225	0.3208
2.00	0.2256	0.3620	0.3273
2.25	0.1658	0.3443	0.3468
2.50	0.1649	0.2645	0.4356
2.75	0.1965	0.1569	0.5142
3.00	0.2341	0.1246	0.5041
3.25	0.3090	0.2103	0.4171
3.50	0.3555	0.2344	0.2720
3.75	0.4451	0.2291	0.1511
4.00	0.6814	0.1395	0.1187

Table B.5: Time evolution of a diagonal torelon at rest on 2.75 unit cells. Column headings 10, 8, 6, 4, 2, 0 correspond to the steps remaining until torelon annihilation. Results from this table are displayed graphically in Fig. 4.7.

Time	Probability					
	10	8	6	4	2	0
0.25	0.8276	0.0320	0.0024	0.0001	0.0000	0.0000
0.50	0.7470	0.0976	0.0227	0.0036	0.0005	0.0000
0.75	0.7232	0.1550	0.0650	0.0132	0.0011	0.0002
1.00	0.6028	0.1439	0.1057	0.0356	0.0048	0.0008
1.25	0.5564	0.1133	0.1190	0.0767	0.0267	0.0032
1.50	0.5280	0.0965	0.0941	0.1139	0.0533	0.0073
1.75	0.5058	0.0999	0.0717	0.1158	0.0895	0.0131
2.00	0.4685	0.0973	0.0720	0.1122	0.1198	0.0173
2.25	0.4494	0.0790	0.0867	0.1249	0.1226	0.0166
2.50	0.4268	0.0765	0.1269	0.1639	0.0953	0.0128
2.75	0.3823	0.0974	0.1642	0.1812	0.0503	0.0082
3.00	0.3453	0.1516	0.2019	0.1593	0.0140	0.0048
3.25	0.3222	0.2279	0.2396	0.1156	0.0108	0.0038
3.50	0.3215	0.2720	0.2184	0.0595	0.0106	0.0028
3.75	0.3581	0.2667	0.1751	0.0361	0.0126	0.0026
4.00	0.4960	0.2191	0.1474	0.0634	0.0122	0.0027

Appendix C

Coefficients for the QITE Algorithm

The content in this appendix is a direct reproduction of [10].

The quantum imaginary time evolution (QITE) algorithm provides best-fit values for the 60 coefficients $(a_\bullet)_j$ within A of Eq. (4.11) by minimizing the difference between two states,

$$|\Delta_0\rangle = \left(\frac{e^{-i\tau A}-1}{\tau}\right)|\psi\rangle\,, \tag{C.1}$$

$$|\Delta\rangle = -iA\,|\psi\rangle\,. \tag{C.2}$$

Writing the coefficients with the simpler notation a_1, a_2, a_3, ..., a_{60}, the quantity to be minimized is

$$\langle\Delta_0-\Delta|\Delta_0-\Delta\rangle \equiv \langle\Delta_0|\Delta_0\rangle + a_j b_j + a_j S_{jk} a_k \tag{C.3}$$

which provides an expression for the coefficients

$$a = -(S+S^T)^{-1}b \tag{C.4}$$

in terms of the 60-component vector b and the 60×60 matrix S, both of which are real-valued. The vector elements are

$$(b_y)_j = -i\,\langle\psi|\left[\hat{H},Y_j\right]|\psi\rangle + O(\Delta\tau), \tag{C.5}$$

$$(b_{yx})_j = -i\,\langle\psi|\left[\hat{H},Y_jX_{j-1}\right]|\psi\rangle + O(\Delta\tau), \tag{C.6}$$

$$(b_{xy})_j = -i\,\langle\psi|\left[\hat{H},X_{j+1}Y_j\right]|\psi\rangle + O(\Delta\tau), \tag{C.7}$$

$$(b_{yz})_j = -i\,\langle\psi|\left[\hat{H},Y_jZ_{j-1}\right]|\psi\rangle + O(\Delta\tau), \tag{C.8}$$

$$(b_{zy})_j = -i\,\langle\psi|\left[\hat{H},Z_{j+1}Y_j\right]|\psi\rangle + O(\Delta\tau), \tag{C.9}$$

and the matrix S is defined by

$$S_{jk} = \langle\psi| V_j V_k^T |\psi\rangle , \tag{C.10}$$

with

$$V_j = \begin{pmatrix} Y_j \\ Y_j X_{j-1} \\ X_{j+1} Y_j \\ Y_j Z_{j-1} \\ Z_{j+1} Y_j \end{pmatrix} . \tag{C.11}$$

Instead of computing all 3600 matrix elements of S, our ansatz retains only single-qubit terms and nearest-neighbor two-qubit terms. In this case, all entries needed for $S + S^T$, b and every term in $H_\square$ (including its three-qubit term) can be obtained from five measurements on the quantum computer.

For the first measurement, prepare $|\psi\rangle$ and then measure each qubit to obtain

$$\langle\psi| Z_j |\psi\rangle = 1 - 2P_j, \tag{C.12}$$

$$\langle\psi| Z_{j+1} Z_j |\psi\rangle = 1 - 2P_{(j+1)\oplus j}, \tag{C.13}$$

where P_j is the probability of measuring 1 rather than 0 for the jth qubit, and $P_{k\oplus j}$ is the probability that either the jth or kth qubit (not both) is 1 rather than 0.

For the second measurement, prepare $\left(\prod_{j=\text{even}} RY_j(-\frac{\pi}{2})\right) |\psi\rangle$ and then measure each qubit to obtain

$$\langle\psi| X_j |\psi\rangle = 1 - 2P_j, \tag{C.14}$$

$$\langle\psi| Z_{j+1} |\psi\rangle = 1 - 2P_{j+1}, \tag{C.15}$$

$$\langle\psi| Z_{j+1} X_j |\psi\rangle = 1 - 2P_{(j+1)\oplus j}, \tag{C.16}$$

$$\langle\psi| Z_{j+1} X_j Z_{j-1} |\psi\rangle = 1 - 2P_{(j+1)\oplus j\oplus(j-1)}, \tag{C.17}$$

where $P_{l\oplus k\oplus j}$ is the probability that an odd number of the three qubits is 1 rather than 0.

For the third measurement, prepare $\left(\prod_{j=\text{even}} RY_{j+1}(-\frac{\pi}{2})\right) |\psi\rangle$ and then measure each qubit to obtain

$$\langle\psi| Z_j |\psi\rangle = 1 - 2P_j, \tag{C.18}$$

$$\langle\psi| X_{j+1} |\psi\rangle = 1 - 2P_{j+1}, \tag{C.19}$$

$$\langle\psi| X_{j+1} Z_j |\psi\rangle = 1 - 2P_{(j+1)\oplus j}, \tag{C.20}$$

$$\langle\psi| Z_{j+2} X_{j+1} Z_j |\psi\rangle = 1 - 2P_{(j+2)\oplus j+1\oplus j}. \tag{C.21}$$

For the fourth measurement, prepare $\left(\prod_j RY_j(-\frac{\pi}{2})\right)|\psi\rangle$ and then measure each qubit to obtain

$$\langle\psi| X_j |\psi\rangle = 1 - 2P_j, \tag{C.22}$$
$$\langle\psi| X_{j+1} |\psi\rangle = 1 - 2P_{j+1}, \tag{C.23}$$
$$\langle\psi| X_{j+1}X_j |\psi\rangle = 1 - 2P_{(j+1)\oplus j}. \tag{C.24}$$

For the fifth measurement, prepare $\left(\prod_j RX_j(\frac{\pi}{2})\right)|\psi\rangle$ and then measure each qubit to obtain

$$\langle\psi| Y_j |\psi\rangle = 1 - 2P_j, \tag{C.25}$$
$$\langle\psi| Y_{j+1} |\psi\rangle = 1 - 2P_{j+1}, \tag{C.26}$$
$$\langle\psi| Y_{j+1}Y_j |\psi\rangle = 1 - 2P_{(j+1)\oplus j}. \tag{C.27}$$

The computations in this appendix have been implemented successfully on IBM_BRISBANE as discussed in Sec. 4.4. Numerical results are provided in Fig. 4.5 and Table C.1. Our quantum computer code for the QITE algorithm is publically available [158].

Table C.1: Imaginary time evolution on 12 qubits of IBM_BRISBANE. The Hamiltonian is Eq. (4.7) with gauge coupling $g = 1$ on a periodic 12-plaquette ladder. The true ground state is obtained successfully through self-mitigation. The eigenvalues are displayed graphically in Fig. 4.5.

τ	$\langle\psi\| H_\square \|\psi\rangle$	
	Without self-mitigation	With self-mitigation
0.1	-3.15±0.19	-6.51±0.20
0.2	-2.00±0.19	-8.46±0.28
0.3	-0.65±0.20	-8.92±0.35
0.4	1.09±0.23	-9.65±0.37
0.5	2.79±0.22	-9.08±0.50
0.6	4.20±0.21	-9.38±0.58
0.7	5.15±0.15	-9.57±0.47
0.8	7.32±0.17	-8.59±0.62
0.9	7.85±0.19	-9.22±0.85

Appendix D

Surface Codes and Lattice Surgery

D.1 Stabilizer Formalism and Surface Codes

Stabilizer codes form the foundation of modern quantum error correction. The mathematical framework relies on the Pauli group and its commuting subgroups [166].

D.1.1 Pauli Group and Stabilizer Formalism

The Pauli group on n qubits, $\mathcal{P}_n$, consists of all n-fold tensor products of Pauli operators $\{I, X, Y, Z\}$ with possible phase factors $\{\pm 1, \pm i\}$. A stabilizer group $\mathcal{S}$ is an abelian subgroup of $\mathcal{P}_n$ that does not contain $-I$. The code space is defined as the simultaneous $+1$ eigenspace of all elements in $\mathcal{S}$:

$$\mathcal{C} = \{|\psi\rangle \in \mathbb{C}^{2^n} : S\,|\psi\rangle = |\psi\rangle \text{ for all } S \in \mathcal{S}\} \tag{D.1}$$

For a stabilizer group with r independent generators, the code space has dimension 2^{n-r}, encoding $k = n - r$ logical qubits.

D.1.2 Rotated Surface Code Structure

The rotated surface code arranges physical qubits on a square lattice with periodic boundary conditions. For a distance-d code, the lattice contains d^2 physical qubits. The stabilizer generators are defined as:

$$S_Z(p) = \bigotimes_{e \in \partial p} Z_e \quad \text{(Z-type stabilizers)} \tag{D.2}$$

$$S_X(v) = \bigotimes_{e \in \delta v} X_e \quad \text{(X-type stabilizers)} \tag{D.3}$$

where ∂p denotes the boundary edges of plaquette p, and δv denotes the edges incident to vertex v.

The logical operators are defined using homologically non-trivial cycles:

$$\bar{Z} = \bigotimes_{e \in C_Z} Z_e \tag{D.4}$$

$$\bar{X} = \bigotimes_{e \in C_X} X_e \tag{D.5}$$

where C_Z and C_X are paths connecting opposite boundaries of the lattice [165].

D.1.3 Error Correction Procedure

The surface code protects quantum information through repeated rounds of syndrome measurements:

1. Measure all Z-type stabilizers to detect X errors
2. Measure all X-type stabilizers to detect Z errors
3. Repeat measurements over multiple rounds
4. Use matching algorithms to identify error locations
5. Apply correction operations based on error patterns

The code distance d determines the error correction capability. A distance-d code can correct any error affecting up to $\lfloor (d-1)/2 \rfloor$ physical qubits [165].

D.2 Stabilizer Measurement Circuits

The implementation of stabilizer measurements in surface codes requires careful circuit design to maintain fault tolerance. The measurement circuits for X-type and Z-type stabilizers follow specific patterns to detect errors without disturbing the encoded logical information.

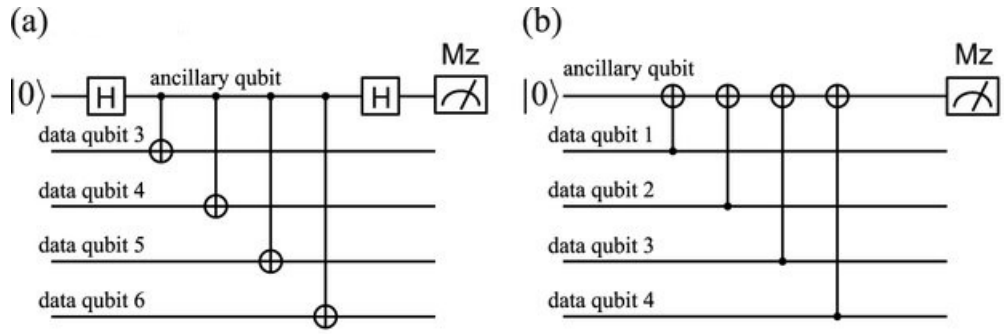

Figure D.1: Stabilizer measurement circuits for the surface code. (a) Circuit for measuring Z-type stabilizers, which detect X errors. The ancillary qubit is initialized to $|0\rangle$ and measured in the Z basis after interacting with four data qubits. (b) Circuit for measuring X-type stabilizers, which detect Z errors. The ancillary qubit is initialized to $|0\rangle$ and measured in the Z basis after interacting with a different set of four data qubits.

D.2.1 Z-Type Stabilizer Measurements

The X-type stabilizer measurement circuit, shown in Fig. D.1(a), operates as follows:

1. Initialize an ancillary qubit to $|0\rangle$
2. Apply Hadamard gates to prepare the ancillary qubit in the $|+\rangle$ state
3. Apply controlled-X (CX) gates between the ancillary qubit and the four data qubits in the stabilizer's support
4. Apply Hadamard gates to return the ancillary qubit to the computational basis
5. Measure the ancillary qubit in the Z basis

The measurement outcome provides the syndrome information for Z errors. If an Z error has occurred on any of the data qubits, it anti-commutes with the X stabilizer and flips the measurement outcome.

D.2.2 Z-Type Stabilizer Measurements

The Z-type stabilizer measurement circuit, shown in Fig. D.1(b), follows a similar pattern:

1. Initialize an ancillary qubit to $|0\rangle$
2. Apply controlled-NOT (CNOT) gates with the ancillary qubit as target and the data qubits as controls

3. Measure the ancillary qubit in the Z basis

This circuit measures the parity of Z operators on the data qubits. X errors on the data qubits will flip the measurement outcome, providing syndrome information for X errors.

D.2.3 Fault-Tolerant Design

The circuits in Fig. D.1 are designed to be fault-tolerant through several key features:

- **Transversal Operations**: The CNOT gates are applied transversally across multiple qubits
- **Error Propagation Control**: The gate sequences are designed to prevent catastrophic error propagation
- **Syndrome Extraction**: Multiple measurement rounds enable distinction between data errors and measurement errors
- **Local Operations**: All operations are local, respecting the geometric constraints of the surface code lattice

These measurement circuits are executed repeatedly in what are called "syndrome extraction rounds." By comparing syndrome measurements across multiple rounds, the decoder can identify and locate errors, enabling reliable quantum error correction even in the presence of faulty operations [165].

D.2.4 Fault Tolerance Properties

Lattice surgery maintains fault tolerance because:

- All operations are performed using local measurements and Pauli corrections
- Errors during the procedure can be detected and corrected by the surface code
- The procedure has a threshold: if physical error rates are below approximately 1%, logical error rates can be made arbitrarily small by increasing code distance
- The overhead scales polynomially with the desired logical error rate

D.2.5 Implementation with Triamond Lattice

When combining surface codes with the triamond lattice approach:

- Each logical qubit replaces a physical qubit in the triamond simulation
- The $j \in \{0, \frac{1}{2}\}$ truncation applies to logical qubits
- Error mitigation becomes unnecessary as logical information is actively protected
- Quantum circuits can run for much longer durations while maintaining coherence
- Complex simulations like hadron-hadron collisions become feasible

D.2.6 Resource Overhead Analysis

The resource requirements for fault-tolerant quantum computation using surface codes are:

- Number of physical qubits per logical qubit: $O(d^2)$
- Number of measurement rounds per logical operation: $O(d)$
- Space-time volume overhead: $O(d^3)$ for a single logical gate
- Threshold for fault tolerance: $\sim 1\%$ physical error rate

Despite this overhead, the ability to perform arbitrarily long computations with suppressed logical error rates makes this approach essential for practical quantum simulation of complex physical systems [165].

This mathematical foundation provides the theoretical basis for fault-tolerant quantum computation using surface codes and lattice surgery, enabling the long-term vision of error-corrected quantum simulations of lattice gauge theories on the triamond lattice.

D.3 Lattice Surgery for Logical Operations

Lattice surgery enables fault-tolerant implementation of multi-qubit gates, particularly the CNOT gate, between logical qubits encoded in surface codes [169, 170].

To understand how this works, consider translating a physical-level circuit, such as the one in 3.7, to the logical level. This circuit contains both CNOT gates and RY(θ) rotations. The strategy for implementing these gates differs significantly:

- **RY(θ) Gates (Non-Clifford):** These gates cannot be applied transversally. They are typically implemented via magic state injection. In this technique, a low-fidelity $R_Y(\theta)$ state is prepared on a physical qubit and placed at the corner of a logical patch. Through d rounds of syndrome measurements, this information is distilled and propagated into the logical state. This process is complex and delicate, and we will not elaborate on it further here.

- **CNOT Gates (Clifford):** These gates can be applied between logical patches using lattice surgery, where two adjacent logical patches can undergo a CNOT gate by being temporarily connected and measured [169].

D.3.1 Merging and Splitting Operations

The CNOT gate between two logical qubits can be implemented through the following lattice surgery procedure:

1. **Merging**: Temporarily merge the two surface code patches along a common boundary
2. **Joint Measurement**: Measure joint stabilizers that couple the two logical qubits
3. **Entanglement Creation**: The joint measurements create entanglement between the logical qubits
4. **Splitting**: Carefully split the merged patch back into separate code patches
5. **Byproduct Operators**: Account for possible byproduct operators that may require correction

D.3.2 Implementing a CNOT via Joint Measurements

Lattice surgery implements a logical CNOT gate by replacing the direct gate operation with a sequence of joint measurements between the two logical patches. A canonical method for this is illustrated in the circuit below (adapted from Gidney), which shows how a CNOT can be decomposed into two joint measurements involving an ancilla [170].

In this circuit, a CNOT gate between two data qubits is replaced with two joint measurements between these data qubits and a new ancillary qubit prepared in the Z basis. At the logical level, a joint measurement is performed by connecting two logical patches through a temporary resource called a "bus." The bus does not hold quantum information but serves to facilitate the transformation. Once we connect the two logical patches with a bus, we run d rounds of syndrome measurements. By measuring the Z syndromes in the bus, we project

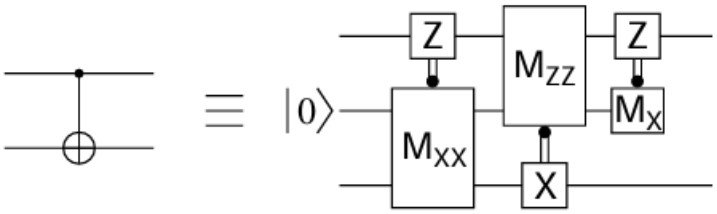

Figure D.2: CNOT implementation via joint measurements (after Gidney and Fowler [170])

the quantum state of two patches onto the $+1$ or -1 eigenstate of $Z \otimes Z$. A similar procedure applies for XX joint measurements.

D.3.3 Mathematical Implementation

To elucidate the CNOT gate implementation in Fig. D.2, we derive the operation mathematically. Consider the initial state:

$$|\psi_{\text{initial}}\rangle = (\alpha_1|0\rangle + \beta_1|1\rangle) \otimes |0\rangle \otimes (\alpha_2|0\rangle + \beta_2|1\rangle)$$

The circuit implements the CNOT gate through the operator sequence:

$$\begin{aligned}|\psi_{\text{final}}\rangle =&(I_1 \otimes H_2 \otimes I_3) \cdot \frac{1}{\sqrt{2}}(I_1 \otimes I_2 \otimes I_3 + Z_1 \otimes Z_2 \otimes I_3) \\ &\cdot \frac{1}{\sqrt{2}}(I_1 \otimes I_2 \otimes I_3 + I_1 \otimes X_2 \otimes X_3) \cdot |\psi_{\text{initial}}\rangle\end{aligned}$$

We compute this evolution step by step:

Step 1: Apply $(I_1 \otimes I_2 \otimes I_3 + I_1 \otimes X_2 \otimes X_3)$ The operator $I_1 \otimes X_2 \otimes X_3$ transforms the state as:

$$\begin{aligned}&(\alpha_1|0\rangle + \beta_1|1\rangle) \otimes |0\rangle \otimes (\alpha_2|0\rangle + \beta_2|1\rangle) \\ \rightarrow&(\alpha_1|0\rangle + \beta_1|1\rangle) \otimes |1\rangle \otimes (\alpha_2|1\rangle + \beta_2|0\rangle)\end{aligned}$$

Thus:

$$\frac{1}{\sqrt{2}}(I + I_1 \otimes X_2 \otimes X_3)|\psi_{\text{initial}}\rangle =$$
$$\frac{1}{\sqrt{2}}\left[(\alpha_1|0\rangle + \beta_1|1\rangle) \otimes |0\rangle \otimes (\alpha_2|0\rangle + \beta_2|1\rangle) + \right.$$
$$\left.(\alpha_1|0\rangle + \beta_1|1\rangle) \otimes |1\rangle \otimes (\alpha_2|1\rangle + \beta_2|0\rangle)\right]$$

Step 2: Apply $(I_1 \otimes I_2 \otimes I_3 + Z_1 \otimes Z_2 \otimes I_3)$ The operator $Z_1 \otimes Z_2 \otimes I_3$ introduces phases based on qubits 1 and 2:

$$\frac{1}{2}(I + Z_1 \otimes Z_2 \otimes I_3)(I + I_1 \otimes X_2 \otimes X_3)|\psi_{\text{initial}}\rangle$$

This yields:

$$\frac{1}{2}\left[\alpha_1\alpha_2|000\rangle + \alpha_1\beta_2|001\rangle + \beta_1\alpha_2|110\rangle + \beta_1\beta_2|111\rangle\right]$$

Step 3: Apply $(I_1 \otimes H_2 \otimes I_3)$ Applying the Hadamard gate to the second qubit:

$$|\psi_{\text{final}}\rangle = \frac{1}{2}(I_1 \otimes H_2 \otimes I_3)\left[\alpha_1\alpha_2|000\rangle + \alpha_1\beta_2|001\rangle + \beta_1\alpha_2|110\rangle + \beta_1\beta_2|111\rangle\right]$$

After simplification, we obtain the CNOT operation between qubit 1 (control) and qubit 3 (target), with the ancilla returning to $|0\rangle$. This result is equivalent to applying a CNOT gate directly to the initial two-qubit state:

$$\begin{aligned}|\psi_{\text{initial}}\rangle &= (\alpha_1|0\rangle + \beta_1|1\rangle) \otimes (\alpha_2|0\rangle + \beta_2|1\rangle) \\ &= \alpha_1\alpha_2|00\rangle + \alpha_1\beta_2|01\rangle + \alpha_2\beta_1|10\rangle + \beta_1\beta_2|11\rangle\end{aligned}$$

yielding:

$$\text{CNOT}|\psi_{\text{initial}}\rangle = \alpha_1\alpha_2|00\rangle + \alpha_1\beta_2|01\rangle + \alpha_2\beta_1|11\rangle + \beta_1\beta_2|10\rangle$$

Note on Measurement Outcomes: This derivation assumes the $(+1, +1)$ outcome for both joint measurements. In practice, the four possible measurement combinations $(+1, +1)$, $(+1, -1)$, $(-1, +1)$, and $(-1, -1)$ require appropriate Pauli corrections (X and/or Z operations on control and target qubits) to implement the exact CNOT gate.

Resource Overhead Considerations

Implementing the circuit in 3.7 at the logical level requires significant quantum resources. In addition to the 12 logical patches needed for the computational qubits, we would require 12

additional logical patches to serve as ancillas for lattice surgery operations.

Each logical patch requires d^2 physical qubits, where d is the code distance. For example, with a code distance of 10, the total physical qubit requirement would be:

$$10^2 \times 24 = 2400 \text{ physical qubits}$$

Furthermore, each CNOT gate requires 2 rounds of parity check measurements during the lattice surgery procedure. Although these resource requirements appear substantial, they represent the future of fault-tolerant quantum computation where quantum systems can continuously self-correct [165, 170].

Once Fault-Tolerant Quantum Computing (FTQC) is achieved, we can anticipate truly extensive Quantum Chromodynamics (QCD) studies becoming feasible. The combination of advanced simulation techniques like the triamond lattice for QCD with FTQC capabilities provides a promising pathway for comprehensive investigations in quantum field theory and particle physics [16].

Bibliography

[1] C. Gattringer and C. B. Lang, "Quantum chromodynamics on the lattice," Lect. Notes Phys. **788**, 1-343 (2010).

[2] F. Knechtli, M. Günther and M. Peardon, "Lattice Quantum Chromodynamics: Practical Essentials," (Springer, 2017).

[3] K. Nagata, "Finite-density lattice QCD and sign problem: Current status and open problems," Prog. Part. Nucl. Phys. **127**, 103991 (2022).

[4] S. R. Coleman, "The Fate of the False Vacuum. 1. Semiclassical Theory," Phys. Rev. D **15**, 2929 (1977) [Phys. Rev. D **16**, 1248 (1977)].

[5] J. Braden, M. C. Johnson, H. V. Peiris, A. Pontzen and S. Weinfurtner, "New Semiclassical Picture of Vacuum Decay," Phys. Rev. Lett. **123**, 031601 (2019) [erratum: Phys. Rev. Lett. **129**, 059901 (2022)].

[6] L. Funcke, T. Hartung, K. Jansen and S. Kühn, "Review on Quantum Computing for Lattice Field Theory," PoS **LATTICE2022**, 228 (2023).

[7] C. W. Bauer, Z. Davoudi, A. B. Balantekin, T. Bhattacharya, M. Carena, W. A. de Jong, P. Draper, A. El-Khadra, N. Gemelke and M. Hanada, *et al.* "Quantum Simulation for High-Energy Physics," PRX Quantum **4**, 027001 (2023).

[8] A. Di Meglio, K. Jansen, I. Tavernelli, C. Alexandrou, S. Arunachalam, C. W. Bauer, K. Borras, S. Carrazza, A. Crippa and V. Croft, *et al.* "Quantum Computing for High-Energy Physics: State of the Art and Challenges. Summary of the QC4HEP Working Group," [arXiv:2307.03236 [quant-ph]].

[9] A. H. Z. Kavaki and R. Lewis, "From square plaquettes to triamond lattices for SU(2) gauge theory," Commun. Phys. **7**, 208 (2024).

[10] A. H. Z. Kavaki and R. Lewis, "False vacuum decay in triamond lattice gauge theory," Phys. Rev. D **112**, 014502 (2025).

[11] C. Michael, "Glueball and Toron Masses From Lattice Gauge Theory," J. Phys. G **13**, 1001 (1987).

[12] K. J. Juge, J. Kuti, F. Maresca, C. Morningstar and M. J. Peardon, "Excitations of torelon," Nucl. Phys. B Proc. Suppl. **129**, 703 (2004).

[13] N. Klco, J. R. Stryker and M. J. Savage, "SU(2) non-Abelian gauge field theory in one dimension on digital quantum computers," Phys. Rev. D **101**, 074512 (2020).

[14] S. A Rahman, R. Lewis, E. Mendicelli and S. Powell, "SU(2) lattice gauge theory on a quantum annealer," Phys. Rev. D **104**, 034501 (2021).

[15] S. A Rahman, R. Lewis, E. Mendicelli and S. Powell, "Self-mitigating Trotter circuits for SU(2) lattice gauge theory on a quantum computer," Phys. Rev. D **106**, 074502 (2022).

[16] C. W. Bauer, Z. Davoudi, N. Klco and M. J. Savage, "Quantum simulation of fundamental particles and forces," Nature Rev. Phys. **5**, 420-432 (2023).

[17] R. L. Workman *et al.* [Particle Data Group], "Review of Particle Physics," PTEP **2022**, 083C01 (2022).

[18] D. J. Gross and F. Wilczek, "Ultraviolet Behavior of Non-Abelian Gauge Theories," Phys. Rev. Lett. **30**, 1343-1346 (1973).

[19] H. D. Politzer, "Reliable Perturbative Results for Strong Interactions?," Phys. Rev. Lett. **30**, 1346-1349 (1973).

[20] R. P. Feynman, "Space-time approach to non-relativistic quantum mechanics," Rev. Mod. Phys. **20**, 367-387 (1948).

[21] M. Creutz, "Quarks, Gluons and Lattices," Cambridge University Press (1983).

[22] K. G. Wilson, "Confinement of Quarks," Phys. Rev. D **10**, 2445-2458 (1974).

[23] M. E. Peskin and D. V. Schroeder, "An Introduction to Quantum Field Theory," Westview Press (1995).

[24] F. J. Wegner, "Duality in Generalized Ising Models and Phase Transitions without Local Order Parameters," J. Math. Phys. **12**, 2259-2272 (1971).

[25] M. Creutz, "Monte Carlo Study of Quantized SU(2) Gauge Theory," Phys. Rev. D **21**, 2308-2315 (1980).

[26] J. B. Kogut and L. Susskind, "Hamiltonian Formulation of Wilson's Lattice Gauge Theories," Phys. Rev. D **11**, 395-408 (1975).

[27] Y. Aoki *et al.* [Flavour Lattice Averaging Group (FLAG)], "FLAG Review 2024," arXiv:2411.04268.

[28] A. Kan, L. Funcke, S. Kühn, L. Dellantonio, J. Zhang, J. F. Haase, C. A. Muschik and K. Jansen, "Investigating a (3+1)D topological θ-term in the Hamiltonian formulation of lattice gauge theories for quantum and classical simulations," Phys. Rev. D **104**, 034504 (2021).

[29] J. Nishimura, K. Sakai and A. Yosprakob, "A new picture of quantum tunneling in the real-time path integral from Lefschetz thimble calculations," JHEP **09**, 110 (2023).

[30] S. Duane, A. D. Kennedy, B. J. Pendleton and D. Roweth, "Hybrid Monte Carlo," Phys. Lett. B **195**, 216-222 (1987).

[31] M. Troyer and U. J. Wiese, "Computational Complexity and Fundamental Limitations to Fermionic Quantum Monte Carlo Simulations," Phys. Rev. Lett. **94**, 170201 (2005).

[32] N. Metropolis, A. W. Rosenbluth, M. N. Rosenbluth, A. H. Teller and E. Teller, "Equation of State Calculations by Fast Computing Machines," J. Chem. Phys. **21**, 1087-1092 (1953).

[33] G. S. Bali, F. Bruckmann, G. Endrődi, Z. Fodor, S. D. Katz, S. Krieg, A. Schäfer and K. K. Szabó, "The QCD phase diagram for external magnetic fields," JHEP **02**, 044 (2012).

[34] P. Balaji, C. Conefrey-Shinozaki, P. Draper, J. K. Elhaderi, D. Gupta, L. Hidalgo, A. Lytle and E. Rinaldi, "Quantum Circuits for SU(3) Lattice Gauge Theory," Phys. Rev. D **112**, 054511 (2025).

[35] P. Balaji, C. Conefrey-Shinozaki, P. Draper, J. K. Elhaderi, D. Gupta, L. Hidalgo and A. Lytle, "Perturbation theory, irrep truncations, and state preparation methods for quantum simulations of SU(3) lattice gauge theory," arXiv:2509.25865 [hep-lat] (2025).

[36] Z. G. Mou, P. M. Saffin and A. Tranberg, "Quantum tunnelling, real-time dynamics and Picard-Lefschetz thimbles," JHEP **11**, 135 (2019).

[37] R. P. Feynman, "Simulating physics with computers," Int. J. Theor. Phys. **21**, 467-488 (1982).

[38] S. Lloyd, "Universal Quantum Simulators," Science **273**, 1073-1078 (1996).

[39] N. Brambilla, S. Eidelman, C. Hanhart, A. Nefediev, C. P. Shen, C. E. Thomas, A. Vairo and C. Z. Yuan, "The XYZ states: experimental and theoretical status and perspectives," Phys. Rept. **873**, 1-154 (2020).

[40] I. Raychowdhury and J. R. Stryker, "Solving Gauss's Law on Digital Quantum Computers with Loop-String-Hadron Digitization," Phys. Rev. Res. **2**, 033039 (2020).

[41] N. Klco, A. Roggero and M. J. Savage, "Standard model physics and the digital quantum revolution: thoughts about the interface," Rept. Prog. Phys. **85**, 064301 (2022).

[42] S. Endo, Z. Cai, S. C. Benjamin and X. Yuan, "Hybrid Quantum-Classical Algorithms and Quantum Error Mitigation," J. Phys. Soc. Jap. **90**, 032001 (2021).

[43] M. Urbanek, B. Nachman, V. R. Pascuzzi, A. He, C. W. Bauer and W. A. de Jong, "Mitigating depolarizing noise on quantum computers with noise-estimation circuits," Phys. Rev. Lett. **127**, 270502 (2021).

[44] P. Bicudo, "Tetraquarks and pentaquarks in lattice QCD with light and heavy quarks," Phys. Rept. **1039**, 1-49 (2023).

[45] T. Aoyama, N. Asmussen, M. Benayoun, J. Bijnens, T. Blum, M. Bruno, I. Caprini, C. M. Carloni Calame, M. Cè and G. Colangelo, *et al.* "The anomalous magnetic moment of the muon in the Standard Model," Phys. Rept. **887**, 1-166 (2020).

[46] D. Banerjee, M. Bögli, M. Dalmonte, E. Rico, P. Stebler, U. J. Wiese and P. Zoller, "Atomic Quantum Simulation of U(N) and SU(N) Non-Abelian Lattice Gauge Theories," Phys. Rev. Lett. **110**, 125303 (2013).

[47] A. Ciavarella, N. Klco and M. J. Savage, "Trailhead for quantum simulation of SU(3) Yang-Mills lattice gauge theory in the local multiplet basis," Phys. Rev. D **103**, 094501 (2021).

[48] Y. Y. Atas, J. Zhang, R. Lewis, A. Jahanpour, J. F. Haase and C. A. Muschik, "SU(2) hadrons on a quantum computer via a variational approach," Nature Commun. **12**, 6499 (2021).

[49] A. N. Ciavarella and I. A. Chernyshev, "Preparation of the SU(3) lattice Yang-Mills vacuum with variational quantum methods," Phys. Rev. D **105**, 074504 (2022).

[50] M. Illa and M. J. Savage, "Basic elements for simulations of standard-model physics with quantum annealers: Multigrid and clock states," Phys. Rev. A **106**, 052605 (2022).

[51] R. C. Farrell, I. A. Chernyshev, S. J. M. Powell, N. A. Zemlevskiy, M. Illa and M. J. Savage, "Preparations for quantum simulations of quantum chromodynamics in 1+1 dimensions. I. Axial gauge," Phys. Rev. D **107**, 054512 (2023).

[52] Y. Y. Atas, J. F. Haase, J. Zhang, V. Wei, S. M. L. Pfaendler, R. Lewis and C. A. Muschik, "Simulating one-dimensional quantum chromodynamics on a quantum computer: Real-time evolutions of tetra- and pentaquarks," Phys. Rev. Res. **5**, 033184 (2023).

[53] R. C. Farrell, I. A. Chernyshev, S. J. M. Powell, N. A. Zemlevskiy, M. Illa and M. J. Savage, "Preparations for quantum simulations of quantum chromodynamics in 1+1 dimensions. II. Single-baryon β-decay in real time," Phys. Rev. D **107**, 054513 (2023).

[54] A. N. Ciavarella, "Quantum simulation of lattice QCD with improved Hamiltonians," Phys. Rev. D **108**, 094513 (2023).

[55] S. Chandrasekharan and U. J. Wiese, "Quantum link models: A Discrete approach to gauge theories," Nucl. Phys. B **492**, 455-474 (1997).

[56] M. Mathur, "Harmonic oscillator prepotentials in SU(2) lattice gauge theory," J. Phys. A **38**, 10015-10026 (2005).

[57] T. Byrnes and Y. Yamamoto, "Simulating lattice gauge theories on a quantum computer," Phys. Rev. A **73**, 022328 (2006).

[58] L. Tagliacozzo, A. Celi, P. Orland and M. Lewenstein, "Simulations of non-Abelian gauge theories with optical lattices," Nature Commun. **4**, 2615 (2013).

[59] E. Zohar, J. I. Cirac and B. Reznik, "Cold-Atom Quantum Simulator for SU(2) Yang-Mills Lattice Gauge Theory," Phys. Rev. Lett. **110**, 125304 (2013).

[60] E. Zohar, J. I. Cirac and B. Reznik, "Quantum simulations of gauge theories with ultracold atoms: local gauge invariance from angular momentum conservation," Phys. Rev. A **88**, 023617 (2013).

[61] K. Stannigel, P. Hauke, D. Marcos, M. Hafezi, S. Diehl, M. Dalmonte and P. Zoller, "Constrained dynamics via the Zeno effect in quantum simulation: Implementing non-Abelian lattice gauge theories with cold atoms," Phys. Rev. Lett. **112**, 120406 (2014).

[62] R. Anishetty and I. Raychowdhury, "SU(2) lattice gauge theory: Local dynamics on nonintersecting electric flux loops," Phys. Rev. D **90**, 114503 (2014).

[63] E. Zohar and M. Burrello, "Formulation of lattice gauge theories for quantum simulations," Phys. Rev. D **91**, 054506 (2015).

[64] A. Mezzacapo, E. Rico, C. Sabín, I. L. Egusquiza, L. Lamata and E. Solano, "Non-Abelian $SU(2)$ Lattice Gauge Theories in Superconducting Circuits," Phys. Rev. Lett. **115**, 240502 (2015).

[65] P. Silvi, E. Rico, M. Dalmonte, F. Tschirsich and S. Montangero, "Finite-density phase diagram of a (1+1)-d non-abelian lattice gauge theory with tensor networks," Quantum **1**, 9 (2017).

[66] M. C. Bañuls, K. Cichy, J. I. Cirac, K. Jansen and S. Kühn, "Efficient basis formulation for 1+1 dimensional SU(2) lattice gauge theory: Spectral calculations with matrix product states," Phys. Rev. X **7**, 041046 (2017).

[67] D. Banerjee, F. J. Jiang, T. Z. Olesen, P. Orland and U. J. Wiese, "From the $SU(2)$ quantum link model on the honeycomb lattice to the quantum dimer model on the kagomé lattice: Phase transition and fractionalized flux strings," Phys. Rev. B **97**, 205108 (2018).

[68] I. Raychowdhury, "Low energy spectrum of SU(2) lattice gauge theory: An alternate proposal via loop formulation," Eur. Phys. J. C **79**, 235 (2019).

[69] P. Sala, T. Shi, S. Kühn, M. C. Bañuls, E. Demler and J. I. Cirac, "Variational study of U(1) and SU(2) lattice gauge theories with Gaussian states in 1+1 dimensions," Phys. Rev. D **98**, 034505 (2018).

[70] E. Zohar and J. I. Cirac, "Removing Staggered Fermionic Matter in $U(N)$ and $SU(N)$ Lattice Gauge Theories," Phys. Rev. D **99**, 114511 (2019).

[71] I. Raychowdhury and J. R. Stryker, "Loop, string, and hadron dynamics in SU(2) Hamiltonian lattice gauge theories," Phys. Rev. D **101**, 114502 (2020).

[72] Y. Ji *et al.* [NuQS], "Gluon Field Digitization via Group Space Decimation for Quantum Computers," Phys. Rev. D **102**, 114513 (2020).

[73] V. Kasper, G. Juzeliunas, M. Lewenstein, F. Jendrzejewski and E. Zohar, "From the Jaynes–Cummings model to non-abelian gauge theories: a guided tour for the quantum engineer," New J. Phys. **22**, 103027 (2020).

[74] Z. Davoudi, I. Raychowdhury and A. Shaw, "Search for efficient formulations for Hamiltonian simulation of non-Abelian lattice gauge theories," Phys. Rev. D **104**, 074505 (2021).

[75] R. Dasgupta and I. Raychowdhury, "Cold-atom quantum simulator for string and hadron dynamics in non-Abelian lattice gauge theory," Phys. Rev. A **105**, 023322 (2022).

[76] V. Kasper, T. V. Zache, F. Jendrzejewski, M. Lewenstein and E. Zohar, "Non-Abelian gauge invariance from dynamical decoupling," Phys. Rev. D **107**, 014506 (2023).

[77] E. Zohar, "Quantum simulation of lattice gauge theories in more than one space dimension—requirements, challenges and methods," Phil. Trans. A. Math. Phys. Eng. Sci. **380**, 20210069 (2021).

[78] J. C. Halimeh, H. Lang and P. Hauke, "Gauge protection in non-abelian lattice gauge theories," New J. Phys. **24**, 033015 (2022).

[79] I. Raychowdhury, "Toward quantum simulating non-Abelian gauge theories," Indian J. Phys. **95**, 1681-1690 (2021).

[80] J. Mildenberger, W. Mruczkiewicz, J. C. Halimeh, Z. Jiang and P. Hauke, "Probing confinement in a $\mathbb{Z}_2$ lattice gauge theory on a quantum computer," [arXiv:2203.08905 [quant-ph]].

[81] D. González-Cuadra, T. V. Zache, J. Carrasco, B. Kraus and P. Zoller, "Hardware Efficient Quantum Simulation of Non-Abelian Gauge Theories with Qudits on Rydberg Platforms," Phys. Rev. Lett. **129**, 160501 (2022).

[82] M. Carena, E. J. Gustafson, H. Lamm, Y. Y. Li and W. Liu, "Gauge theory couplings on anisotropic lattices," Phys. Rev. D **106**, 114504 (2022).

[83] Z. Davoudi, A. F. Shaw and J. R. Stryker, "General quantum algorithms for Hamiltonian simulation with applications to a non-Abelian lattice gauge theory," Quantum **7**, 1213 (2023).

[84] X. Yao, "SU(2) gauge theory in 2+1 dimensions on a plaquette chain obeys the eigenstate thermalization hypothesis," Phys. Rev. D **108**, L031504 (2023).

[85] T. Jakobs, M. Garofalo, T. Hartung, K. Jansen, J. Ostmeyer, D. Rolfes, S. Romiti and C. Urbach, "Canonical momenta in digitized Su(2) lattice gauge theory: definition and free theory," Eur. Phys. J. C **83**, 669 (2023).

[86] T. V. Zache, D. González-Cuadra and P. Zoller, "Quantum and Classical Spin-Network Algorithms for q-Deformed Kogut-Susskind Gauge Theories," Phys. Rev. Lett. **131**, 171902 (2023).

[87] T. Hayata and Y. Hidaka, "String-net formulation of Hamiltonian lattice Yang-Mills theories and quantum many-body scars in a nonabelian gauge theory," JHEP **09**, 126 (2023).

[88] J. C. Halimeh, L. Homeier, A. Bohrdt and F. Grusdt, "Spin exchange-enabled quantum simulator for large-scale non-Abelian gauge theories," [arXiv:2305.06373 [cond-mat.quant-gas]].

[89] A. Chan, Z. Shi, L. Dellantonio, W. Dür and C. A. Muschik, "Hybrid variational quantum eigensolvers: merging computational models," [arXiv:2305.19200 [quant-ph]].

[90] B. Müller and X. Yao, "Simple Hamiltonian for quantum simulation of strongly coupled (2+1)D SU(2) lattice gauge theory on a honeycomb lattice," Phys. Rev. D **108**, 094505 (2023).

[91] G. Cataldi, G. Magnifico, P. Silvi and S. Montangero, "(2+1)D SU(2) Yang-Mills Lattice Gauge Theory at finite density via tensor networks," [arXiv:2307.09396 [hep-lat]].

[92] C. W. Bauer, I. D'Andrea, M. Freytsis and D. M. Grabowska, "A new basis for Hamiltonian SU(2) simulations," [arXiv:2307.11829 [hep-ph]].

[93] L. Ebner, B. Müller, A. Schäfer, C. Seidl and X. Yao, "Eigenstate Thermalization in 2+1 dimensional SU(2) Lattice Gauge Theory," Phys. Rev. D **109**, 014504 (2024).

[94] E. J. Gustafson, H. Lamm and F. Lovelace, "Primitive Quantum Gates for an $SU(2)$ Discrete Subgroup: Binary Octahedral," [arXiv:2312.10285 [hep-lat]].

[95] L. Ebner, A. Schäfer, C. Seidl, B. Müller and X. Yao, "Entanglement Entropy of $(2+1)$-Dimensional SU(2) Lattice Gauge Theory," [arXiv:2401.15184 [hep-lat]].

[96] F. Turro, A. Ciavarella and X. Yao, "Classical and Quantum Computing of Shear Viscosity for $2+1D$ SU(2) Gauge Theory," Phys. Rev. D **109**, 114511 (2024).

[97] M. Illa, C. E. P. Robin and M. J. Savage, "Qu8its for Quantum Simulations of Lattice Quantum Chromodynamics," [arXiv:2403.14537 [quant-ph]].

[98] M. Motta, C. Sun, A. T. K. Tan, M. J. O. Rourke, E. Ye, A. J. Minnich, F. G. S. L. Brandão and G. K. L. Chan, "Determining eigenstates and thermal states

on a quantum computer using quantum imaginary time evolution," Nature Phys. **16**, 205-210 (2019).

[99] C. Charles, E. J. Gustafson, E. Hardt, F. Herren, N. Hogan, H. Lamm, S. Starecheski, R. S. Van de Water and M. L. Wagman, "Simulating $\mathbb{Z}_2$ lattice gauge theory on a quantum computer," [arXiv:2305.02361 [hep-lat]].

[100] R. C. Farrell, M. Illa, A. N. Ciavarella and M. J. Savage, "Scalable Circuits for Preparing Ground States on Digital Quantum Computers: The Schwinger Model Vacuum on 100 Qubits," PRX Quantum **5**, 020315 (2024).

[101] M. Asaduzzaman, R. G. Jha and B. Sambasivam, "Sachdev-Ye-Kitaev model on a noisy quantum computer," Phys. Rev. D **109**, 105002 (2024).

[102] L. Hidalgo and P. Draper, "Quantum Simulations for Strong-Field QED," Phys. Rev. D **109**, 076004 (2024).

[103] O. Kiss, M. Grossi and A. Roggero, "Quantum error mitigation for Fourier moment computation," [arXiv:2401.13048 [quant-ph]].

[104] M. S. Anis et al., Qiskit: An open-source framework for quantum computing, doi:10.5281/zenodo.2573505 (2021).

[105] F. Laves, "Zur Klassifikation der Silikate. Geometrische Untersuchungen möglicher Silicium-Sauerstoff- Verbände als Verknüpfungsmöglichkeiten regulärer Tetraeder," Zeitschrift für Kristallographie, **82**, 1 (1932).

[106] H. S. M. Coxeter, "On Laves' Graph Of Girth Ten," Canadian Journal of Mathematics, **7**, 18 (1955).

[107] T. Sunada, "Crystals That Nature Might Miss Creating," Notices of the American Mathematical Society, **55**, 208 (2008).

[108] C. H. Séquin, "Intricate Isohedral Tilings of 3D Euclidean Space," in *Bridges Leeuwarden: Mathematics, Music, Art, Architecture, Culture*, London: Tarquin Publications (2008).

[109] J. H. Conway, H. Burgiel, C. Goodman-Strauss, "The symmetries of things," A. K. Peters Ltd, Wellesley (2008).

[110] R. Suizu and K. Awaga, "Line graph theory reveals hidden spin frustration and bond frustration in molecular crystals with strong isotropy," J. Mater. Chem, C**10**, 1196 (2022).

[111] E. H. Moore, "On the reciprocal of the general algebraic matrix," Bull. Am. Math. Soc. **26** 394–395 (1920).

[112] R. Penrose, "A Generalized inverse for matrices," Proc. Cambridge Phil. Soc. **51**, 406-413 (1955).

[113] C. G. Callan, Jr. and S. R. Coleman, "The Fate of the False Vacuum. 2. First Quantum Corrections," Phys. Rev. D **16**, 1762 (1977).

[114] W. Y. Ai, B. Garbrecht and C. Tamarit, "Functional methods for false vacuum decay in real time," JHEP **12**, 095 (2019).

[115] A. Zenesini, A. Berti, R. Cominotti, C. Rogora, I. G. Moss, T. P. Billam, I. Carusotto, G. Lamporesi, A. Recati and G. Ferrari, "False vacuum decay via bubble formation in ferromagnetic superfluids," Nature Phys. **20**, 558 (2024).

[116] L. Batini, A. Chatrchyan and J. Berges, "Real-time dynamics of false vacuum decay," Phys. Rev. D **109**, 2 (2024).

[117] A. Sinha, T. Chanda and J. Dziarmaga, "Non-adiabatic dynamics across a first order quantum phase transition: Quantized bubble nucleation," Phys. Rev. B **103**, L220302 (2021).

[118] G. Lagnese, F. M. Surace, M. Kormos and P. Calabrese, "False vacuum decay in quantum spin chains," Phys. Rev. B **104**, L201106 (2021).

[119] G. Lagnese, F. M. Surace, S. Morampudi and F. Wilczek, "Detecting a Long-Lived False Vacuum with Quantum Quenches," Phys. Rev. Lett. **133**, 240402 (2024).

[120] J. Vodeb, J. Y. Desaules, A. Hallam, A. Rava, G. Humar, D. Willsch, F. Jin, M. Willsch, K. Michielsen and Z. Papić, "Stirring the false vacuum via interacting quantized bubbles on a 5,564-qubit quantum annealer," Nature Phys. **21**, 386 (2025).

[121] D. Luo, F. M. Surace, A. De, A. Lerose, E. R. Bennewitz, B. Ware, A. Schuckert, Z. Davoudi, A. V. Gorshkov and O. Katz, *et al.* "Quantum simulation of bubble nucleation across a quantum phase transition," arXiv:2505.09607.

[122] Z. H. Zhu, Y. Liu, G. Lagnese, F. M. Surace, W. Y. Zhang, M. G. He, J. C. Halimeh, M. Dalmonte, S. C. Morampudi and F. Wilczek, *et al.* "Probing false vacuum decay on a cold-atom gauge-theory quantum simulator," arXiv:2411.12565.

[123] J. R. Stryker, "Oracles for Gauss's law on digital quantum computers," Phys. Rev. A **99**, 042301 (2019).

[124] P. Emonts and E. Zohar, "Gauss law, minimal coupling and fermionic PEPS for lattice gauge theories," SciPost Phys. Lect. Notes **12**, 1 (2020).

[125] D. B. Kaplan and J. R. Stryker, "Gauss's law, duality, and the Hamiltonian formulation of U(1) lattice gauge theory," Phys. Rev. D **102**, 094515 (2020).

[126] C. Kane, D. M. Grabowska, B. Nachman and C. W. Bauer, "Efficient quantum implementation of 2+1 U(1) lattice gauge theories with Gauss law constraints," arXiv:2211.10497.

[127] I. D'Andrea, C. W. Bauer, D. M. Grabowska and M. Freytsis, "New basis for Hamiltonian SU(2) simulations," Phys. Rev. D **109**, 074501 (2024).

[128] M. Carena, H. Lamm, Y. Y. Li and W. Liu, "Quantum error thresholds for gauge-redundant digitizations of lattice field theories," Phys. Rev. D **110**, 054516 (2024).

[129] C. Ball and T. D. Cohen, "Zeno effect suppression of gauge drift in quantum simulations," Phys. Rev. A **110**, 022417 (2024).

[130] S. V. Kadam, A. Naskar, I. Raychowdhury and J. R. Stryker, "Loop-string-hadron approach to SU(3) lattice Yang-Mills theory: Gauge invariant Hilbert space of a trivalent vertex," arXiv:2407.19181.

[131] P. Fontana, M. M. Riaza and A. Celi, "An efficient finite-resource formulation of non-Abelian lattice gauge theories beyond one dimension," arXiv:2409.04441.

[132] D. M. Grabowska, C. F. Kane and C. W. Bauer, "A Fully Gauge-Fixed SU(2) Hamiltonian for Quantum Simulations," arXiv:2409.10610.

[133] I. M. Burbano and C. W. Bauer, "Gauge Loop-String-Hadron Formulation on General Graphs and Applications to Fully Gauge Fixed Hamiltonian Lattice Gauge Theory," arXiv:2409.13812.

[134] E. Ballini, J. Mildenberger, M. M. Wauters and P. Hauke, "Symmetry verification for noisy quantum simulations of non-Abelian lattice gauge theories," arXiv:2412.07844.

[135] M. S. Alam, S. Hadfield, H. Lamm and A. C. Y. Li, "Primitive quantum gates for dihedral gauge theories," Phys. Rev. D **105**, 114501 (2022).

[136] E. J. Gustafson, H. Lamm, F. Lovelace and D. Musk, "Primitive quantum gates for an SU(2) discrete subgroup: Binary tetrahedral," Phys. Rev. D **106**, 114501 (2022).

[137] A. N. Ciavarella and C. W. Bauer, "Quantum Simulation of SU(3) Lattice Yang-Mills Theory at Leading Order in Large-Nc Expansion," Phys. Rev. Lett. **133**, 111901 (2024).

[138] T. Hayata and Y. Hidaka, "Floquet evolution of the q-deformed SU(3)1 Yang-Mills theory on a two-leg ladder," arXiv:2409.20263.

[139] A. N. Ciavarella, "String Breaking in the Heavy Quark Limit with Scalable Circuits," arXiv:2411.05915.

[140] A. T. Than, Y. Y. Atas, A. Chakraborty, J. Zhang, M. T. Diaz, K. Wen, X. Liu, R. Lewis, A. M. Green, C. A. Muschik and N. M. Linke, "The phase diagram of quantum chromodynamics in one dimension on a quantum computer," arXiv:2501.00579.

[141] C. Michael, "Particle Decay in Lattice Gauge Theory," Nucl. Phys. B **327**, 515 (1989).

[142] C. Michael, "Torelons and Unusual Ground States," Phys. Lett. B **232**, 247 (1989).

[143] H. B. Meyer, "The spectrum of SU(N) gauge theories in finite volume," JHEP **03**, 064 (2005).

[144] M. García Pérez, A. González-Arroyo and M. Okawa, "Spatial volume dependence for 2+1 dimensional SU(N) Yang-Mills theory," JHEP **09**, 003 (2013).

[145] M. García Pérez, A. González-Arroyo, M. Koren and M. Okawa, "The spectrum of 2+1 dimensional Yang-Mills theory on a twisted spatial torus," JHEP **07**, 169 (2018).

[146] A. Athenodorou and M. Teper, "The torelon spectrum and the world-sheet axion," PoS **LATTICE2021**, 103 (2022).

[147] L. Ebner, B. Müller, A. Schäfer, L. Schmotzer, C. Seidl and X. Yao, "Entanglement Properties of SU(2) Gauge Theory," arXiv:2411.04550.

[148] R. C. Farrell, M. Illa, A. N. Ciavarella and M. J. Savage, "Quantum simulations of hadron dynamics in the Schwinger model using 112 qubits," Phys. Rev. D **109**, 11 (2024).

[149] K. F. Koenig, F. Reinecke, W. Hahn and T. Wellens, "Inverted-circuit zero-noise extrapolation for quantum-gate error mitigation," Phys. Rev. A **110**, 042625 (2024).

[150] E. J. Gustafson, J. Tiihonen, D. Chamaki, F. Sorourifar, J. W. Mullinax, A. C. Y. Li, F. B. Maciejewski, N. P. Sawaya, J. T. Krogel and D. E. B. Neira, *et al.* "Surrogate Optimization of Variational Quantum Circuits," arXiv:2404.02951.

[151] F. Turro, K. A. Wendt, S. Quaglioni, F. Pederiva and A. Roggero, "Evaluation of phase shifts for nonrelativistic elastic scattering using quantum computers," Phys. Rev. C **110**, 054604 (2024).

[152] F. Turro, I. A. Chernyshev, R. Bhaskar and M. Illa, "Qutrit and Qubit Circuits for Three-Flavor Collective Neutrino Oscillations," arXiv:2407.13914.

[153] Z. Li, D. M. Grabowska and M. J. Savage, "Sequency Hierarchy Truncation (SeqHT) for Adiabatic State Preparation and Time Evolution in Quantum Simulations," arXiv:2407.13835.

[154] D. Teplitskiy, O. Kiss, M. Grossi and A. Mandarino, "Statistics of topological defects across a phase transition in a superconducting quantum processor," arXiv:2410.06250.

[155] N. A. Zemlevskiy, "Scalable Quantum Simulations of Scattering in Scalar Field Theory on 120 Qubits," arXiv:2411.02486.

[156] IBM Quantum, `https://quantum-computing.ibm.com`.

[157] A. H. Z. Kavaki and R. Lewis, "Triamond lattice video," https://vimeo.com/904585432.

[158] https://github.com/randylewis/SelfMitigatedQITE.

[159] https://github.com/alikavaki.

[160] Y. Chai, A. Crippa, K. Jansen, S. Kühn, V. R. Pascuzzi, F. Tacchino and I. Tavernelli, "Entanglement production from scattering of fermionic wave packets: a quantum computing approach," [arXiv:2312.02272 [quant-ph]].

[161] Z. Davoudi, C. C. Hsieh and S. V. Kadam, "Scattering wave packets of hadrons in gauge theories: Preparation on a quantum computer," [arXiv:2402.00840 [quant-ph]].

[162] Z. Davoudi, N. Mueller and C. Powers, "Towards Quantum Computing Phase Diagrams of Gauge Theories with Thermal Pure Quantum States," Phys. Rev. Lett. **131**, 081901 (2023).

[163] T. Sunada, "Crystals that nature might miss creating," Not. Am. Math. Soc. **55**, 208 (2008).

[164] R. Suizu and K. Awaga, "Line graph theory reveals hidden spin frustration and bond frustration in molecular crystals with strong isotropy," J. Mater. Chem, C**10**, 1196 (2022).

[165] A. G. Fowler, M. Mariantoni, J. M. Martinis and A. N. Cleland, "Surface codes: Towards practical large-scale quantum computation," Phys. Rev. A **86**, 032324 (2012).

[166] D. Gottesman, "Stabilizer codes and quantum error correction," Caltech PhD Thesis (1997).

[167] S. B. Bravyi and A. Y. Kitaev, "Quantum codes on a lattice with boundary," [arXiv:quant-ph/9811052].

[168] E. T. Campbell, B. M. Terhal and C. Vuillot, "Roads towards fault-tolerant universal quantum computation," Nature **549**, 172-179 (2017).

[169] D. Horsman, A. G. Fowler, S. Devitt and R. Van Meter, "Surface code quantum computing by lattice surgery," New J. Phys. **14**, 123011 (2012).

[170] C. Gidney, "Low overhead quantum computation with lattice surgery," arXiv:1808.06709 [quant-ph] (2018).